Duskside Relativistic Electron Precipitation

by

Kirsten Ruth Lorentzen

A dissertation submitted in partial fulfillment
of the requirements for the degree of

Doctor of Philosophy

University of Washington

1999

Approved by Michael McCarthy
(Chairperson of Supervisory ~~Committee~~)

Program Authorized
to Offer Degree Geophysics Program

Date March 16, 1999

In presenting this dissertation in partial fulfillment of the requirements for the Doctoral degree at the University of Washington, I agree that the Library shall make its copies freely available for inspection. I further agree that extensive copying of the dissertation is allowable only for scholarly purposes, consistent with "fair use" as prescribed in the U.S. Copyright Law. Requests for copying or reproduction of this dissertation may be referred to UMI Dissertation Services, 300 North Zeeb Road, Ann Arbor, MI 48106-1346, to whom the author has granted "the right to reproduce and sell (a) copies of the manuscript in microform and/or (b) printed copies of the manuscript made from microform."

Signature Kristen Loentjes

Date March 16, 1999

University of Washington

Abstract

Duskside Relativistic Electron Precipitation

by Kirsten Ruth Lorentzen

Chairperson of Supervisory Committee:
Professor Michael P. McCarthy
Geophysics Program

On August 20, 1996, a balloon-borne X-ray pinhole camera and a high resolution germanium X-ray spectrometer observed an intense X-ray event near Kiruna, Sweden, at 1835 MLT, on an L-shell of 5.8. This X-ray event consisted of seven bursts spaced 100-200 seconds apart, with smaller 10-20 second variations observed within individual bursts. The energy spectra of these bursts show the presence of X-rays with energies greater than 1 MeV, which are best accounted for by atmospheric bremsstrahlung from mono-energetic 1.7 MeV precipitating electrons. The X-ray imager observed no significant motion or small-scale spatial structure in the event, implying that the bursts were temporal in nature. Ultra-violet images from the Polar satellite and energetic particle data from the Los Alamos geosynchronous satellites show a small magnetospheric substorm onset about 24 minutes before the start of the relativistic precipitation event. Since the balloon was south of the auroral oval and there was no associated increase in relativistic electron flux at geosynchronous altitude, the event must be the result of some mechanism selectively precipitating ambient relativistic electrons from the radiation belts.

The balloon X-ray observations are analyzed in a magnetospheric context, in order to determine which of several mechanisms for selective precipitation of relativistic electrons can account for the event. Resonance with electromagnetic ion cyclotron mode waves on the equator is the most likely candidate. The drift of substorm-injected warm protons is

calculated using input from the geosynchronous satellites. Wave growth in the model is driven by temperature anisotropies in the warm proton population. A numerical solution of the wave dispersion relation shows that electromagnetic ion cyclotron waves can be excited in high-density duskside regions such as the plasmasphere or detached plasma regions. These waves can selectively precipitate relativistic electrons of energy 1.7 MeV in regions of density greater than 10 cm^{-3}, given the appropriate warm proton temperature, density, and anisotropy. The model is used to investigate the effects of variations in these free parameters, and shows that only a narrow range of values can produce waves that interact with 1.7 MeV electrons.

TABLE OF CONTENTS

LIST OF FIGURES

LIST OF TABLES

ACKNOWLEDGMENTS

I would like to thank my advisor, Michael McCarthy, for his guidance in all aspects of this project, from buiding the instruments, to analyzing the data, to writing this dissertation. I would also like to thank the other members of my supervisory committee, George Parks, Robert Holzworth, Robert Winglee, and Ron Merrill for their useful suggestions.

The X-ray imagers were made possible through the electronic design efforts of engineers John Chin, Tim Chinowsky, and Irwan Budihardjo. Other computer and mechanical help was provided by Jeff Ross and Steve Domonkos.

The CESR team of Jean-Paul Treilhou, Jacques Coutelier, Jean-Jacques Thocaven and Christian Jacquey deserve credit for organizing the INTERBOA campaign. The efforts of CNES and Esrange during three perfect balloon launches are also appreciated. Thanks also to the PGI team of Leonid Borovkov, Leonid Schur and Leonid Lazutin. Particular thanks are due to the Berkeley team of Robert Lin, Jason Foat, Robyn Millan, David Smith, and Frances Fenrich for the germanium detector data and many useful discussions about the nature of the event.

Some of the data presented in this dissertation were obtained from scientists at other institutions who very kindly made their data available through the internet for this global study, although they were not involved in the original balloon experiment. The scientists and institutions are Geoff Reeves, Michelle Thomsen, and David McComas of Los Alamos National Laboratory, John Hargreaves and Steve Marple at Lancaster University, UK, and Johan Stadsnes at the University of Bergen, Norway.

I would also like to express my appreciation to all of my officemates and fellow Space Physics group members, Ruth Skoug, Ben Barnum, Andrew Meadows, Kerry Deutsch, John Williams, Matt Fillingim, Ted Freeman, Suvro Datta, Frank Lind, Li-Jen Chen, Qing Li, Damien Chua, Ron Elsen, Mark Wilber and Mitch Brittnacher, for their friendship and assistance over the years.

I want to thank my parents for always encouraging me in my goals. And most of all, I want to thank my husband, Michael Loverude, for his love and support, and also for feeding the cat and putting up with me through everything.

This work was supported by NSF grants ATM9223612 and ATM9806400, and by a NASA Graduate Student Researchers Program fellowship NGT5-50095.

Chapter 1

INTRODUCTION

1.1 Auroral Electron Precipitation

Auroras are created when precipitating electrons collide with atmospheric particles. These collisions excite the atmospheric particles and produce the visible lights sometimes seen at night. Auroras can also occur during the daytime, but then the visible lights are obscured by sunlight. The electrons that create the aurora are usually of low enough energy (<100 keV) that relativistic effects are unimportant [*Swift*, 1981], but sometimes very high energy (>100 keV) relativistic electrons are observed as well. Non-relativistic electrons in the Earth's magnetosphere have been much more extensively studied than relativistic electrons. It is not fully understood how relativistic electrons are accelerated to such high energies or what causes them to be precipitated into the atmosphere. The purpose of this dissertation is to present coordinated ground, balloon, and satellite-based observations of a duskside relativistic electron precipitation (REP) event, and to identify and evaluate the theoretical mechanisms most likely to account for the precipitation.

For a variety of reasons, we want to understand how and why relativistic electrons precipitate into the atmosphere. Relativistic electron precipitation presents a very interesting energy transport problem in space physics, one that has not yet been adequately explained. Although a general study of the physical processes involved in relativistic electron precipitation is the primary motivation for this dissertation, there are also certain practical considerations for wanting to understand this process. Relativistic electrons can be extremely damaging to satellites and humans in space, so an ability to predict the behavior of these particles is desirable, given the increasing number of spacecraft now orbiting the Earth.

Also, relativistic electron precipitation has been shown to produce odd nitrogen molecules, which can cause ozone destruction in the lower atmosphere [*Callis et al.*, 1991].

By studying a single case of REP using coordinated observations from different points in space, we can gain insight into how magnetospheric factors affect the process. New types of balloon-borne instruments such as X-ray imagers and germanium spectrometers can characterize spatial, temporal and energy features with more resolution that previous observations. During the particular REP event presented in this dissertation, several scientific satellites were in position to provide coordinated data about the magnetosphere. By using data from multiple locations, we can evaluate theories for REP events, and gain insight that can be used to plan future research on this type of event.

1.1.1 Particle Motion in the Magnetosphere

In order to understand how electrons precipitate into the Earth's atmosphere, it is necessary to first understand how they behave in the magnetosphere. Charged particles in a magnetic field exhibit three basic types of motion, which are illustrated in Figure 1.1 for a dipole field. All three types of motion occur because of the magnetic part of the Lorentz force, $q_e((\vec{v}/c) \times \vec{B})$, where q_e is the signed electric charge, $\vec{v}$ is the velocity, c is the speed of light, and $\vec{B}$ is the magnetic field. Charged particles gyrate around magnetic field lines, travel along field lines bouncing between north and south poles, and drift around the Earth in longitude. The first type of motion, gyration around the field lines, is easiest to understand in terms of the Lorentz force. The second type of motion occurs because electrons and ions feel an increase in the magnetic field strength as they travel in helical paths along the field lines toward one of the Earth's poles. This change in magnetic field creates a mirror force that can turn the particles around and cause them to bounce between the poles. The third type of motion occurs because of the gradient and curvature in the Earth's magnetic field. This gradient and curvature creates a centrifugal force, $\vec{F}$, directed away from the center of the Earth, which causes a longitudinal drift in the $(\vec{F} \times \vec{B})/q_e$ direction.

These three types of motion can be completely described by a particle's energy and pitch-angle. The pitch-angle is the angle between the particle's velocity and the magnetic field. A particle will continue to exhibit drift, bounce, and gyration motion without precipitating, unless its pitch-angle is such that the particle collides with the ionosphere before the mirror force is great enough to turn it around. If something happens to change the velocity and pitch-angle of drifting particles, then they can precipitate and create aurora.

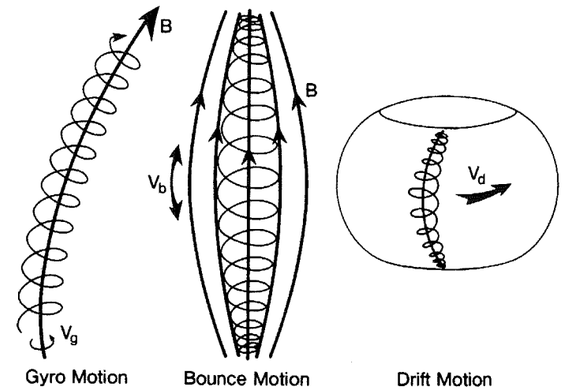

Figure 1.1: Three kinds of particle motion in a dipole magnetic field, from *Kivelson and Russell* [1995].

Particles that drift all the way around the Earth are considered to be trapped. The position of a particle as it drifts around the earth can be described by the L-shell or L-parameter, which gives the distance to a dipole field line at the equator, measured in Earth radii, R_E. Particles are only trapped in the region where the magnetic field is close to dipolar. Figure 1.2 shows the magnetosphere, which is stretched into a tail on the nightside because of the interaction of the solar wind with the Earth's magnetic field. Because of the shape of the magnetosphere, particles are only trapped in closed drift orbits out to about 8 R_E [*Schulz and Lanzerotti*, 1974]. The region where energetic particles are trapped is known as the Van Allen radiation belts.

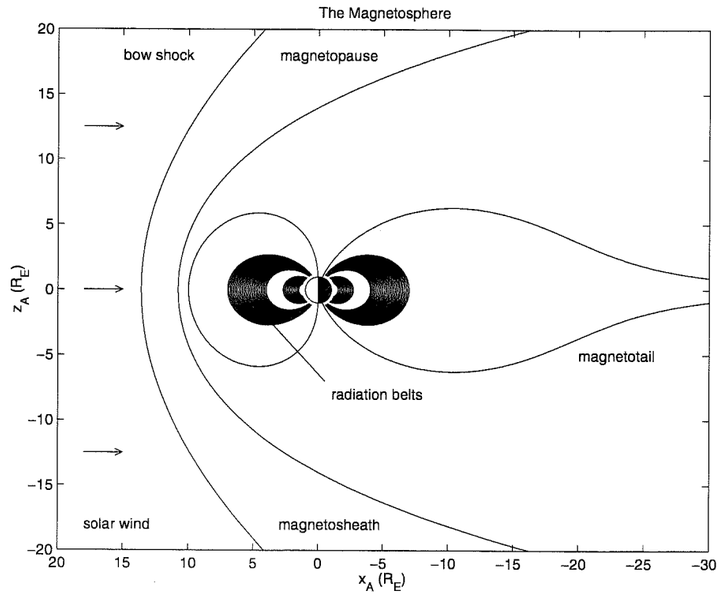

Figure 1.2: The Earth's magnetosphere and the Van Allen radiation belts.

1.1.2 Magnetospheric Substorms

Although some auroral electrons originate from the radiation belts near the earth, more electron precipitation originates from the more distant magnetotail through a process known as a magnetospheric substorm. In the magnetotail, where the magnetic field is no longer dipolar, particles and fields behave differently than in the radiation belts. Sometimes the stretched tail will relax back into a more dipole-like configuration, which results in the transport of energetic particles from the tail to the near-Earth region. This relaxation is part of the process known as a magnetospheric substorm. It can be seen at geosynchronous satellite altitudes of 6.6 R_E in the form of a sudden injection of charged particles with energies of up to hundreds of keV. It can also be seen in the ionosphere in the form of aurora on the field lines mapping to the injection region. The visible aurora are created by the precipitation of electrons with energies $\sim$1-10 keV. The substorm dipolarization of the

magnetotail and the associated auroral oval signatures are shown in Figure 1.3. The substorm phenomenology provides a well-studied framework in which to interpret dynamic magnetospheric phenomena.

1.2 Observed Characteristics of Relativistic Electrons

In this section, previous observations of relativistic electrons are briefly summarized and discussed in order to provide background for the new observations presented in Chapter 3. The rest mass of an electron is 511 keV and the rest mass of a proton is 938 MeV, so particles with kinetic energies near or above these value are considered relativistic. The relativistic formula for kinetic energy is $mc^2(\gamma - 1)$, where m is is the mass of the particle, γ is the relativistic mass factor, $(1 - v^2/c^2)^{-1/2}$, v is the velocity of the particle, and c is the speed of light. Table 1.1 gives velocities and relativistic mass factors for particles of various energies. Since 100 keV electrons travel faster than half the speed of light, it is reasonable to consider electron energies above this energy as relativistic, although some researchers restrict the definition to electrons in the MeV range. Typical magnetospheric proton energies are not relativistic.

Relativistic electron precipitation was first inferred from the absorption of high frequency (HF) forward scatter radio signals transmitted during the day [*Bailey and Pomerantz*, 1965]. Because so many observations of relativistic electron precipitation are related to observations of electromagnetic waves, a summary of the standard nomenclature for

Table 1.1: Velocities and relativistic mass factors for particles of various energies.

type of particle	kinetic energy in keV	v/c	γ
electron	1	0.063	1.002
electron	100	0.55	1.2
electron	1000	0.95	3
proton	1000	0.023	1.0003

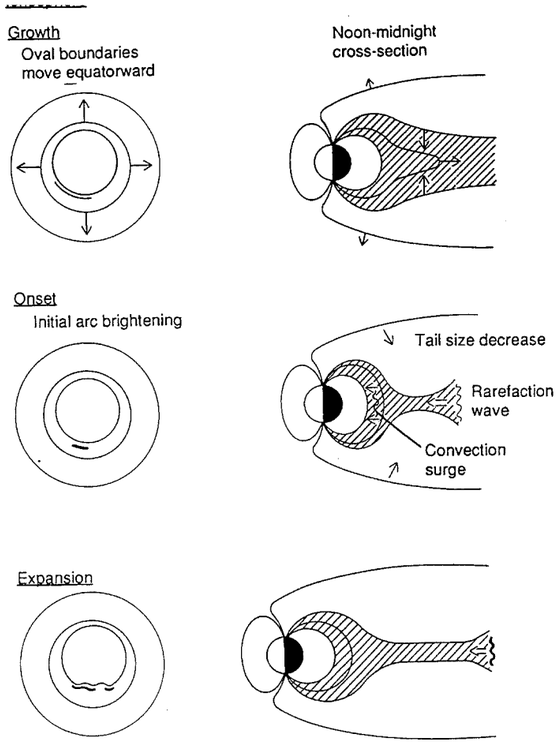

Figure 1.3: Typical characteristics of a substorm in the ionosphere and in the magnetosphere, from *Lui* [1991]. In the growth phase, the magnetotail is stretched, and the auroral oval is small. At the substorm onset, the tail suddenly relaxes into a more dipole-like configuration, particle injections can be seen at the equator at $L = 6.6$, and the auroral oval brightens as some of these injected particles are precipitated. In the expansion phase, the auroral oval becomes larger on the nightside as the injected particles spread out in the near-Earth magnetosphere.

Table 1.2: Classification of magnetic frequencies, where Pc stands for pulsations continuous, ULF stands for ultra low frequency, ELF for extremely low frequency, VLF for very low frequency, and HF for high frequency.

Nomenclature		Period range	Frequency Range
ULF	Pc 5	150 - 600 s	1.7 - 6.7 mHz
	Pc 4	45 - 150 s	6.7 - 22 mHz
	Pc 3	10 - 45 s	22 - 100 mHz
	Pc 2	5 - 10 s	0.1 - 0.2 Hz
	Pc 1	0.2 - 5 s	0.2 - 5 Hz
ELF		0.001 - 0.2 s	5 Hz - 1 kHz
VLF		0.033 - 1 ms	1 kHz - 30 kHz
HF		0.033 - 0.33 μs	3 MHz - 30 MHz

various wave frequencies is given in Table 1.2. Since HF radio waves propagate beyond line-of-sight by scattering off the conducting ionosphere, changes in the intensity of forward scatter signals from a known source indicate changes in the height of the ionosphere. Occasionally, an extremely low ionospheric height was observed, and was believed to be the result of a phenomenon *Bailey and Pomerantz* [1965] named relativistic electron precipitation (REP). Typical precipitating electrons have energies below 100 keV, and create ionization at altitudes around 100 km. Higher energy electrons can penetrate much deeper into the atmosphere, since the scattering and absorption cross-sections are much larger for higher energy electrons. The very low conducting layers seen in HF forward scatter data were believed to be caused by REP events creating ionization at low altitudes.

Because recombination of ions changes the ionosphere density profile from day to night, a different radio wave method is used to identify REP events occurring at night. This nighttime method involves monitoring phase changes in very low frequency (VLF) radio waves [*Thorne and Larsen*, 1976]. Both types of radio wave observations have been used to establish that REP events tend to occur following magnetospheric substorms, but

that not all substorms are accompanied by REP events [*Thorne and Larsen*, 1976].

1.2.1 X-Ray Observations

Observations of REP events using radio waves are limited, since the day and night techniques are not the same, making it difficult to compare observations from different local times. In addition, the radio wave methods do not provide a simple way to obtain quantitative measurements of the precipitation flux. X-ray observations provide a more direct method of measuring REP events, and can be carried out during both day and night. Precipitating electrons produce X-rays at altitudes around 100 km through the bremsstrahlung process. Bremsstrahlung theory is well understood, so it is possible to determine the energy spectrum of precipitating electrons by measuring the X-rays produced. The main limitation in measuring X-rays is that the observations must be carried out from stratospheric balloons at altitudes above 30 km, because the X-rays cannot penetrate through the lowest layers of the atmosphere. Since it is not possible to predict when and where REP events will occur and the typical stratospheric balloon can only remain aloft for a few days, REP observations from balloons are somewhat rare.

The first balloon observations of REP events were by *Rosenberg et al.* [1972]. They observed very high energy X-rays at the same time as forward scatter radio wave observations established the presence of an REP event. The X-rays were observed in three channels (>25 keV, >50 keV, and >100 keV) and electron spectra deduced from these measurements had approximately the same spectral shape as electrons observed simultaneously from geosynchronous satellites in five channels (50-1900 keV). By assuming an exponential form for the energy spectrum, $dJ/dE \propto \exp(-E/E_0)$, where J is the X-ray flux, E is the energy, and E_0 is a constant, they determined a value for E_0 of 100-150 keV.

Some years later, *Parks et al.* [1979] and *West and Parks* [1984] observed a very hard X-ray spectrum from 20 to >120 keV in 6 channels from another balloon experiment. Figure 1.4 shows the X-ray count rate from this event. The X-ray flux was enhanced for 20 minutes near local noon by bursts of X-rays lasting 1-2 minutes. These bursts in X-ray flux were correlated in time with ELF emissions centered around 1.5 kHz, which led to the conclusion that wave-particle interactions were responsible for the REP event. By

assuming an exponential form for the energy spectrum, they determined a value for E_0 of 200 keV.

1.2.2 Primary Electron Observations

Balloons are good for observations of REP events because balloons are essentially stationary, and can view a moderately large region at once. However, it is not possible to measure the primary electron precipitation from a balloon. With satellites and rockets, it is possible to directly measure the primary electrons but difficult to distinguish spatial and temporal characteristics. Rocket observations of REP events are somewhat rare, but *Matthews and Simons* [1973] observed electron precipitation between 50-1000 keV with periodicities of 0.8, 1.3 and 6 seconds, and more recently *Herrero et al.* [1991] observed electron precipitation between 0.1 and 3.8 MeV with time scales of 10-20 seconds and > 100 seconds. Both rockets observed exponentially falling energy spectra, but these measurements were limited since rocket flights only last for a few minutes.

Satellite observations of relativistic electrons are more numerous, but are also limited since the spacecraft fly quickly through the regions of interest. Satellite measurements can be separated into two categories: trapped electrons and precipitating electrons. Geosynchronous satellites sometimes observe increases in the fluxes of relativistic electron population trapped in the radiation belts, but these particles do not necessarily precipitate into the ionosphere. Only satellites that can measure electron pitch-angles, or satellites that are located at low altitudes can determine if relativistic electrons are precipitating or not. Although relativistic electrons trapped in the radiation belts are not the subject of this dissertation, precipitating relativistic electrons are likely to originate from the trapped populations, so these observations are discussed as well.

Trapped Relativistic Electrons

Paulikas and Blake [1979] were the first to present a long-term study of variations in the trapped relativistic electron flux. They found very good correlation between increases in the solar wind speed and increases in the geosynchronous relativistic flux, delayed by a

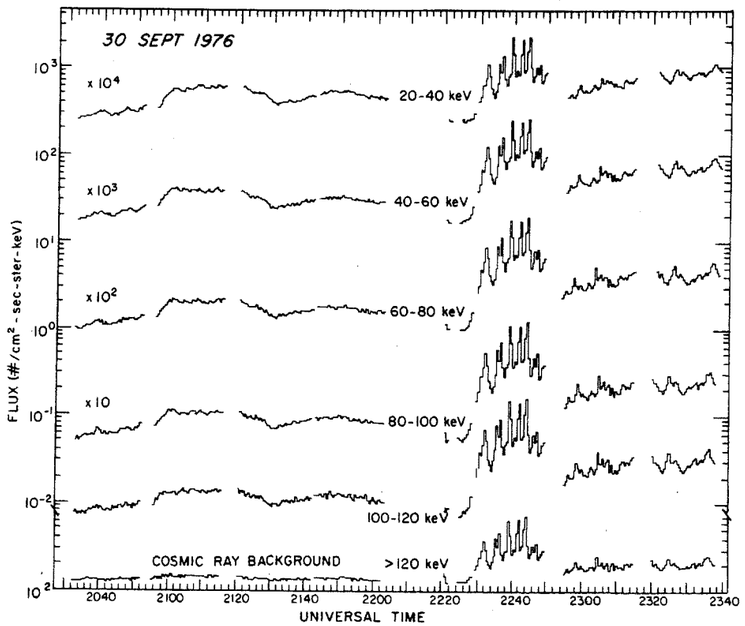

Figure 1.4: Previous balloon X-ray observations of a dayside REP event from *West and Parks* [1984].

day or two. The 140-600 keV electron flux increase appeared to follow solar wind velocity increases by about a day, and the $>$ 3.9 MeV electron flux increases appeared to follow solar wind velocity increases by about two days.

Baker et al. [1986] also used data from geosynchronous satellites to study the temporal history of trapped relativistic electrons between 3 and 10 MeV. They found enhancements of flux lasting for several days. These enhancements were found to be correlated with the 11-year solar cycle and with the 27-day solar rotation.

Nagai [1988] studied trapped electron flux at geosynchronous orbit for energies greater than 2 MeV. He found that the relativistic electron flux decreases at the beginning of geomagnetic storms, then recovers and increases to higher than pre-storm levels on a time scale of several days.

Reeves [1998] carried out a statistical study of trapped relativistic flux at geosynchronous altitudes in comparison to magnetic storms measured by the D_{ST} index. He found that relativistic electron events were correlated with decreases in D_{ST}, but that the reverse was not necessarily true.

Precipitating Relativistic Electrons

Thorne and Andreoli [1980] used fourteen months of measurements from the low-altitude polar-orbiting S3-3 satellite to carry out a statistical study of relativistic electron precipitation occurrence. This satellite observed electrons from 35 keV to 1.1 MeV in five energy channels. During the 20-second spin period, all pitch-angles were sampled, making it possible to determine whether or not the electrons were precipitating. Using the limited pitch-angle and energy data from the events, they roughly classified the events according to which wave-particle mechanism was most likely to have caused the precipitation. Whistler mode waves were associated with electron scattering that is most intense at low energies (33 keV) in the absence of ion precipitation. Electromagnetic ion cyclotron mode waves were associated with electron scattering that is most intense at high energies (850 keV). Electrostatic ion cyclotron waves were associated with electron scattering in a broad energy range accompanied by ion precipitation. Out of 313 observed relativistic precipitation events, they found 7 events that could be linked to whistler mode scattering, all located on

the morningside, and 4 events that could be linked to electromagnetic ion cyclotron mode scattering, all located on the duskside. The remainder of the events occurred primarily on the nightside and were attributed to scattering by electrostatic ion cyclotron waves. No mechanisms other than wave-particle interactions were considered in this study.

Imhof et al. [1991] observed both trapped and precipitating relativistic electrons from 6 keV to 1 MeV from the S81-1 satellite. They also found that precipitation was more likely to occur on the nightside, and near the radiation belt boundary. These events were attributed to scattering in the magnetotail, not wave-particle interactions. They set a scale size for the events of less than 100 km, but this scale size may also be the result of a temporal effect.

Blake et al. [1996] and *Nakamura et al.* [1995] observed bands of precipitating relativistic electrons in the pre-midnight sector with energies $>$ 1 MeV from the low-altitude polar-orbiting SAMPEX satellite. These precipitating events were also observed near the outer edges of the radiation belts, for periods of 10-30 seconds, persisting over several 90-minute satellite orbits. This time scale is comparable to the spatial scale observed by *Imhof et al.* [1991]. They also observed microbursts lasting less than one second in the relativistic electron precipitation.

Imhof et al. [1997] measured pitch-angle distributions of REP events in more detail using the UARS satellite. They found that pitch-angle distributions were nearly isotropic for precipitation of electrons between 30 keV and 5 MeV near the outer edge of the radiation belts. The observed events were all near local midnight.

In summary, satellite observations of trapped relativistic electrons are quite different from observations of precipitating relativistic electrons. Trapped relativistic electron flux enhancements are linked to solar wind phenomena. These enhancements are observed throughout the radiation belts, and can last for several days. In contrast, satellite observations of precipitating relativistic electrons tend to be seen for much shorter time periods, and occur primarily near midnight. Unfortunately, the inherent space-time ambiguity of direct measurements of primary electron spectra limits the usefulness of these measurements for testing theories for precipitation of relativistic electrons. There is a need for long period observations of REP events that can resolve space-time ambiguities, such as X-ray measurements from balloons in combination with satellite observations of the magnetosphere.

1.3 Mechanisms for Energization of Trapped Relativistic Electrons

Although the focus of this dissertation is on mechanisms for precipitation and not energization of relativistic electrons, the existing models for energization are briefly summarized here for completeness. Electrons in the outer radiation belts originate in the solar wind and the ionosphere, where energies are typically non-relativistic. Acceleration by the well-established magnetospheric processes of radial diffusion or convective electric fields cannot account for MeV electron energies observed in the radiation belts [*Liu and Rostoker*, 1995]. *Fujimoto and Nishida* [1990] have presented a recirculation model, in which electrons with energies on the order of 100 keV are accelerated to MeV energies through a repeated three-step process involving 1) inward radial diffusion, 2) pitch-angle diffusion through wave-particle interactions, and 3) low-altitude cross-L diffusion. *Rostoker et al.* [1998] have presented a magnetic pumping model involving compressional waves that create ULF pulsations in the Pc 5 range and pitch-angle scattering by whistler mode waves. *Hudson et al.* [1999a, b] have developed a model in which electrons are energized to relativistic energies over the course of several hours through a drift resonance with the electric field component of Pc 5 ULF waves. Effects of electron acceleration by whistler mode waves have been considered by *Li et al.* [1997] and *Horne and Thorne* [1998]. *Summers et al.* [1998] used these whistler mode results in a stochastic energization model in which cyclotron resonant interaction with whistler mode chorus outside the plasmasphere can accelerate electrons to MeV energies. There is not currently enough data to fully evaluate these mechanisms for energization of relativistic electrons, since the models all invoke multiple processes occurring over long periods of time in different regions of space.

1.4 Mechanisms for Precipitation of Trapped Relativistic Electrons

The precipitation of relativistic electrons is a very different process from the energization process described in the previous section. In this dissertation, we focus only on mechanisms for precipitation. There are three common mechanisms that can change a trapped particle's pitch-angle and cause it to precipitate. One method for changing a particle's velocity is acceleration by an electric field parallel to the magnetic field [*Lyons and Williams*,

1984]. Another mechanism involves nightside scattering off the magnetotail current sheet where the magnetic field is more curved than on the dayside [*Sergeev et al.*, 1983]. A third mechanism is exchange of energy with electromagnetic waves [*Thorne and Andreoli*, 1980]. Waves and particles can exchange energy through the cyclotron resonance, which occurs when a particle's gyrofrequency matches the wave frequency in the particle's frame of reference. The velocity and pitch-angle of a relativistic electron can be changed by any of these mechanisms, allowing the electron to precipitate. These three mechanisms will be discussed in more detail in Chapter 4.

1.5 Scope of Research

Although REP events have been observed for over thirty years, very few studies have correlated measurements from various regions of the magnetosphere. In addition, no studies have investigated both spatial and spectral characteristics of REP events. Satellite studies attempting to limit REP size are limited by the inherent uncertainties in spatial and temporal variations. In this dissertation, we describe new measurements that overcome some of these difficulties, and discuss these measurements in the context of precipitation theories mentioned above.

In Chapter 2, we describe a set of complementary balloon-borne X-ray instruments that allow multi-day measurements of auroral precipitation. The University of Washington X-ray imager was designed to make images of the auroral region with time resolution on the order of tens of seconds, in order to eliminate the space-time ambiguity present in other types of measurements. The X-ray imager also measures energy spectra from 20-120 keV with resolution of about 10 keV. The University of California germanium detector complements the X-ray imager by providing energy spectra from 20-1400 keV with resolution of about 2 keV. These instruments can observe a region of sky about 100 km in diameter at 100 km altitude for several days, recording the spatial, temporal and energy characteristics of an REP event from beginning to end.

Chapter 3 presents balloon observations of a half-hour REP event, along with related ground and satellite measurements. The observed duskside REP event had somewhat different characteristics than previously observed REP events described in this introduction, which were primarily observed at night. The observed event had an X-ray spectrum that is best accounted for by mono-energetic 1.7 MeV electrons. Previous X-ray observations had been accounted for by exponentially falling electron spectra, possibly due to the fact that those instruments did not have the energy range or resolution to differentiate between spectral shapes. The new event had a distinct temporal structure, consisting of seven pulsations with periodicity of 100-200 seconds, similar to that observed on the dayside by [*West and Parks*, 1984]. In addition, the X-ray imager observations were able to definitively show that these pulsations were temporal rather than spatial in nature. Other observations at this time show the presence of a small substorm on the nightside and a localized field line resonance at the balloon location.

In Chapter 4, we discuss mechanisms that may account for the selective precipitation of the 1.7 MeV electrons, identifying wave-particle interactions with the electromagnetic ion cyclotron mode as the most probable candidate. In addition, we evaluate the possible influence of the field line resonance and the substorm on the REP event.

In Chapter 5, the wave-particle interaction model is investigated further, using numerical solution of the ion cyclotron dispersion relation, in order to determine whether wave-growth is sufficient to account for the observed precipitation. This calculation takes into account the drift of substorm injected protons. Input to the calculation are measurements of the nightside equatorial particle population from geosynchronous satellites.

We conclude that a model of relativistic electron interaction with electromagnetic ion cyclotron waves driven by drifting substorm-injected protons can satisfactorily account for the observed mono-energetic spectral shape, duskside occurrence, and localized spatial extent. This case study shows that the model is feasible and that balloon observations, which are a simple and low-cost method of observing electron precipitation, have the potential to provide needed information about REP events. Further balloon observations of such duskside REP events, preferably correlated with satellite observations on the same magnetic field lines, will be able to expand our knowledge of the REP phenomenon.

Chapter 2

BALLOON INSTRUMENTATION

The INTERBOA balloon instruments were carefully chosen in order to best characterize both wave and particle aspects of auroral phenomena. For the campaign, the University of Washington (UW) provided two instruments, an X-ray imaging camera and a VLF magnetic search coil antenna. The University of California at Berkeley (UCB) provided a germanium X-ray spectrometer. The Polar Geophysical Institute (PGI) in Apatity, Russia, provided an X-ray spectrometer and a Geiger-Muller counter. The Centre d'Etude Spatiale des Rayonnements (CESR), in Toulouse, France, provided three-axis electric field probes and a three-axis magnetometer.

The three types of X-ray instruments were chosen to complement one another. The X-ray imager was chosen to provide spatial information about X-rays with energies between 20 and 120 keV. The germanium detector (GED) was chosen because its energy range extended up to 1.4 MeV and because it had excellent energy resolution. However, the GED was somewhat fragile, and no spare instruments were provided, so the PGI spectrometer overlapped the energy range of the GED up to 200 keV. The X-ray imagers and PGI spectrometers were less expensive and more robust designs than the GED so X-ray imagers and PGI spectrometers were available for multiple flights. Table 2.1 compares the properties of the three X-ray instruments. In this chapter, only the X-ray imaging camera and the germanium X-ray spectrometer are discussed in detail, because these two instruments provided the observations most relevant to the study of the relativistic electron precipitation event. The electromagnetic field instruments are briefly described in the last section of this chapter.

Table 2.1: Comparison of X-ray detector properties.

	UW X-Ray Imager	UCB Germanium X-Ray Detector	PGI X-Ray Detector
Energy Range	20-120 keV	20-1400 keV	20-200 keV
Energy Resolution	10 keV at 60 keV	2 keV at 300 keV	10 keV at 60 keV
Time needed for one spectrum	~5 s	$\leq$ 0.5 s	similar to GED
Geometric Factor	~5 cm^2 ster	~25 cm^2 ster	similar to GED
Field of View	90°	90°	90°
Advantages	imaging capability, and sturdiness	energy range, energy resolution, time resolution	energy range time resolution, low cost, and sturdiness

2.1 The X-Ray Imager

The X-ray imager is an Anger type pinhole camera [*Anger*, 1958], similar to those used in medical imaging of gamma rays. Figure 2.1 illustrates the basic principles of this type of instrument. X-rays are focused onto a scintillation crystal by a pinhole in a lead shield. A pinhole is used because X-rays cannot be effectively reflected or refracted by conventional optical lenses. This pinhole is actually almost 2 cm in diameter, but in comparison to the area of sky being imaged, it acts like the tiny pinhole in an optical camera. When X-rays hit the scintillator, the X-ray energy is converted into visible light. Four photomultiplier tubes (PMTs) then detect this light and produce voltage pulses whose amplitude gives the amount of light detected by each individual tube. The distribution of light between the four tubes tells where the X-ray interaction occurred. The sum of the four tube responses gives the total amount of light collected, which is proportional to the energy of the X-ray.

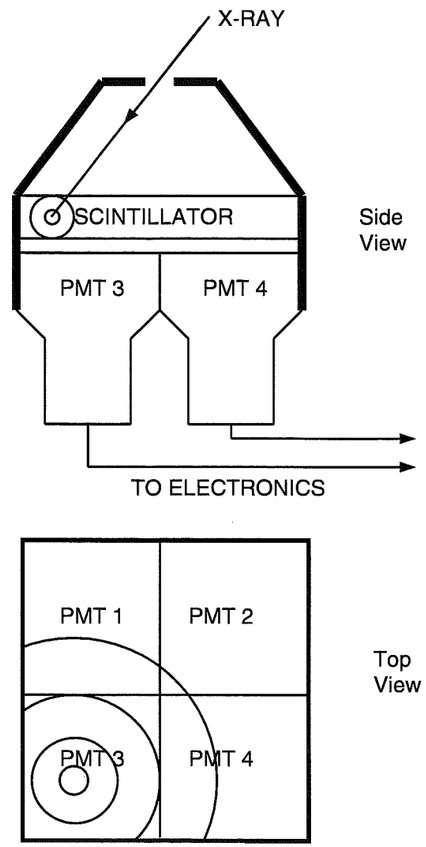

Figure 2.1: The basic principles of the X-ray imager. First the lead pinhole collimator focuses X-rays like a camera. Then the scintillator emits visible photons when hit by an X-ray. The PMTs detect these photons and send signals to the electronics. The distribution of photons among the PMTs gives the location of the X-ray. The total of the four PMT responses is proportional to the energy of the X-ray.

The current version of the X-ray imager is based on several auroral X-ray cameras previously designed and built at the University of Washington [*Mauk et al.*, 1981; *Werden*, 1988; *Parks et al.*, 1993], although significant changes and improvements were made for the newest instruments. For example, the present X-ray imager version uses four square photomultiplier tubes rather than seven hexagonal ones, substantially altering the image-forming algorithm. In addition, the analog electronics were modified to include a new system for rejecting cosmic rays, and the logic and data processing systems were designed to take advantage of recent advances in digital electronics technology.

For the INTERBOA campaign, four identical imagers were constructed for the four planned balloon flights, although only three of them actually flew. All three imagers were recovered after the flights in working condition, which facilitated post-flight calibrations. Each imager was physically contained in two boxes, one containing the scintillator and photomultipliers (the camera unit) and the other containing most of the necessary electronics. In this chapter, each unit is described in its own subsection, and the final two subsections describe the calibration procedure and the image-forming algorithm.

2.1.1 Camera Unit

The design of the camera unit carefully considered a number of factors in order to optimize the instrument performance. Because imaging is a statistical process, it was necessary to balance instrument spatial resolution with the exposure time in order to obtain enough counts to form a meaningful image. This optimization process involved finding the ideal combination of pinhole size and crystal thickness for the chosen energy range. The energy range was set to be 20-120 keV because most auroral X-rays observed at balloon altitudes (about 35 km) lie between these energies. Although X-rays with lower energies are produced in auroras, almost all are absorbed by the atmosphere before reaching balloon altitudes. Figure 2.2 shows how the main parts fit together in the camera unit. In this illustration, details specific to the auroral X-ray measuring capabilities of the instrument, such as the pinhole, scintillators, and PMTs, are emphasized, while more strictly engineering details are omitted.

The pinhole size was chosen so that a reasonable number of auroral X-rays with ener-

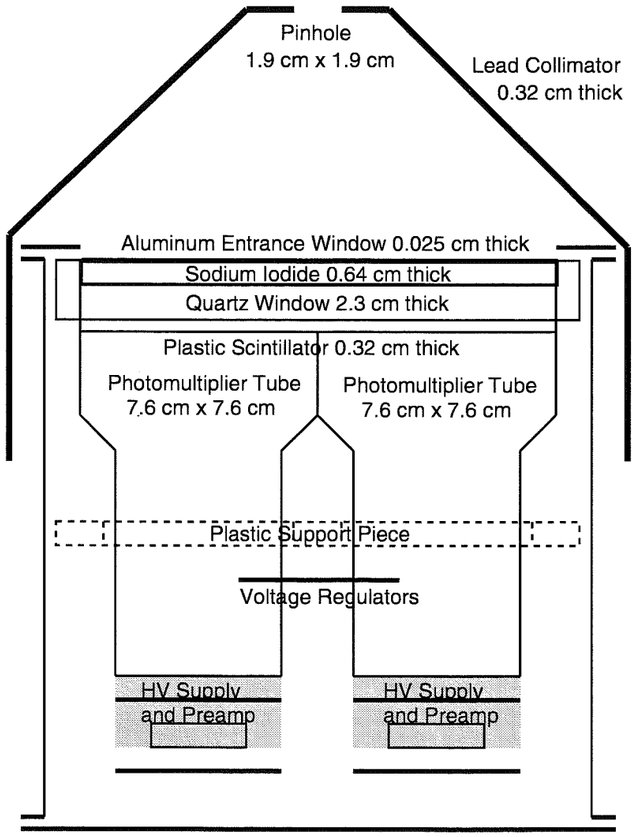

Figure 2.2: A cross-section of the X-ray imager camera unit.

gies between 20 and 120 keV would be collected each second. The count rate was limited on the upper end by the capabilities of the electronics, and on the lower end by statistical requirements for good images. In addition, the size of the pinhole limited the spatial resolution of the camera. We chose a square pinhole of size 1.9×1.9 cm^2. The height of the pinhole above the crystal was chosen to give a 90 degree field of view. For a crystal of size 15.24×15.24 cm^2, these parameters give a geometry factor of about 4.2 cm^2 ster. Balloon observations of X-ray fluxes from active auroral events can vary from 100 to 1000 cm^{-2} sec^{-1} ster^{-1} [*Werden*, 1988], which would give a range of observed count rates of 420 to 4200 counts/second for this geometry factor. Telemetry rates limited the information sent down to only 420 X-ray events/second. For a pinhole of size 1.9×1.9 cm^2 the spatial resolution was limited to 64 pixels on a crystal of size 15.24×15.24 cm^2.

In order for the images to be statistically reasonable, each pixel needed to see enough counts for its $\sqrt{n}/n$ error to be less than 10%. Using this criteria, the minimum time needed to form a reasonable 64-pixel image is about 20 seconds. At typical auroral altitudes of 100 km (65 km above the balloon altitude), the field of view has a diameter of about 100 km and resolution of about 10 km, which is a reasonable spatial scale for observing typical auroral phenomena such as arcs and patches. If electron precipitation is of higher energy than that observed in typical aurora, the X-ray production region will be at a lower altitude, and the field of view will be correspondingly smaller.

The pinhole was made by placing a 0.32 cm thick lead collimator over the surface of the scintillator crystal. The thickness of the lead was chosen because only about 5 in 10^7 X-rays of 120 keV can pass through without being absorbed. Of course, higher energy X-rays and very high energy cosmic ray particles can still pass through the lead, but the high-level energy threshold and anti-coincidence systems described later in this chapter rejected these undesirable events.

The thickness of the sodium iodide scintillator crystal was chosen to optimize light collection for X-rays in the energy range 20-120 keV. Sodium iodide converts X-rays into visible light via the processes of photoelectric absorption and Compton scattering. In a very thin crystal, X-rays would escape before being photoelectrically absorbed and depositing all their energy in the crystal. In a very thick crystal it is impossible to predict at exactly

what depth the X-ray interaction would occur. Most interactions would occur near the upper surface of the crystal, and the light produced would be very diffuse by the time it reached the lower surface and the four PMTs. Interactions occurring near the lower surface of the crystal, however, would produce light that was much less diffuse. In addition, a thicker crystal would be very expensive and fragile.

A quartz glass light pipe whose thickness was chosen to optimize light distribution among all four tubes was located between the scintillator and the photomultiplier tubes. A very thin light pipe would concentrate light over only one tube, and position determination would be impossible, since at least three PMT measurements are needed to determine a position in a plane. A very thick light pipe would spread out the light too evenly between all four tubes, so that position determination would also be impossible. Computer simulations of light transport aided in determining the ideal thickness for the light pipe.

The scintillator crystal was made of thallium activated sodium iodide (NaI(Tl)), which is a hygroscopic material and would begin to react if exposed to the moisture in air. Therefore the scintillator crystal and light pipe were manufactured as one unit, encased in an aluminum housing. X-rays reached the scintillator through a 0.025 cm thick aluminum entrance window. A diffuse, reflective, white powder coating between the crystal and aluminum ensured that the maximum amount of light would reach the tubes.

In order to screen out high energy cosmic ray charged particles, a two-scintillator anti-coincidence system was used. An organic, plastic scintillator of type NE-102 was placed below the sodium iodide scintillator and light pipe, and the anti-coincidence system operated on the principle that photons such as X-rays would interact in only one location in a scintillator of sufficient thickness (photoelectric absorption or Compton scattering followed by photoelectric absorption), while high-energy charged particles such as cosmic ray muons would interact continuously along a path as they traveled through the scintillators (Coulomb collisions). Therefore an X-ray would make a signal in only one scintillator, while a cosmic ray would make a signal in both scintillators. Any event causing a coincident signal in both scintillators was rejected. The anti-coincidence scintillator was chosen to be plastic, not sodium iodide, because the response times of these two scintillator materials differ significantly, and therefore the rise times of the output voltage pulses differ.

The electronics were designed to distinguish between the shapes of pulses from the two scintillator materials. This type of anti-coincidence system is called a phoswich system [*Knoll*, 1989]. The plastic scintillator was 0.32 cm thick and was located between the light pipe and the tubes. Since sodium iodide is denser than plastic, and was located above the plastic, most of the X-ray interactions of interest occurred in the sodium iodide.

The photomultiplier tubes were 7.62×7.62 cm^2 square tubes packed closely together under the scintillator assembly. Mechanical and optical coupling between the quartz light pipe, the plastic anti-coincidence scintillator, and the tubes was by means of an optical gel. Light loss at the interfaces between the four tubes was negligible. Light loss at the outer edge of the scintillator was more significant and will be discussed later in this chapter.

Each tube was attached to its own charge-sensitive preamplifier and adjustable high-voltage supply. The tubes produced charge pulses that were very sensitive to electronic noise, so it was important to have the preamplifiers as close to the tubes as possible. Because the gain of the tubes varied with voltage, the adjustable high-voltage supply was used to ensure that all the tubes had identical gain, a necessary prerequisite for imaging.

2.1.2 Electronics Design

Figure 2.3 shows a block diagram for the different parts of the X-ray imager electronics. Except for the high-voltage supplies and charge-sensitive preamplifiers, which were located in the camera unit, all other flight electronics were located in the Electronics/Data Processing Unit (DPU) box. This box contained six printed circuit boards for the imager: four peak detect boards, a logic board, and a DPU board, all connected via a backplane. This section briefly describes the function of each of these boards, in as much detail as relates to the features needed to form the X-ray images.

There was one peak detect board for each photomultiplier tube. These boards fulfilled a number of functions, the most important being shaping and amplifying the signals from the tubes, and converting the pulse height into an 8-bit number using an analog-to-digital converter (ADC). In addition, the peak detect boards also made sure that the PMT pulses satisfied a number of different criteria. Only pulses with energies above a certain low-level threshold and below a certain high-level threshold were accepted, in order to restrict

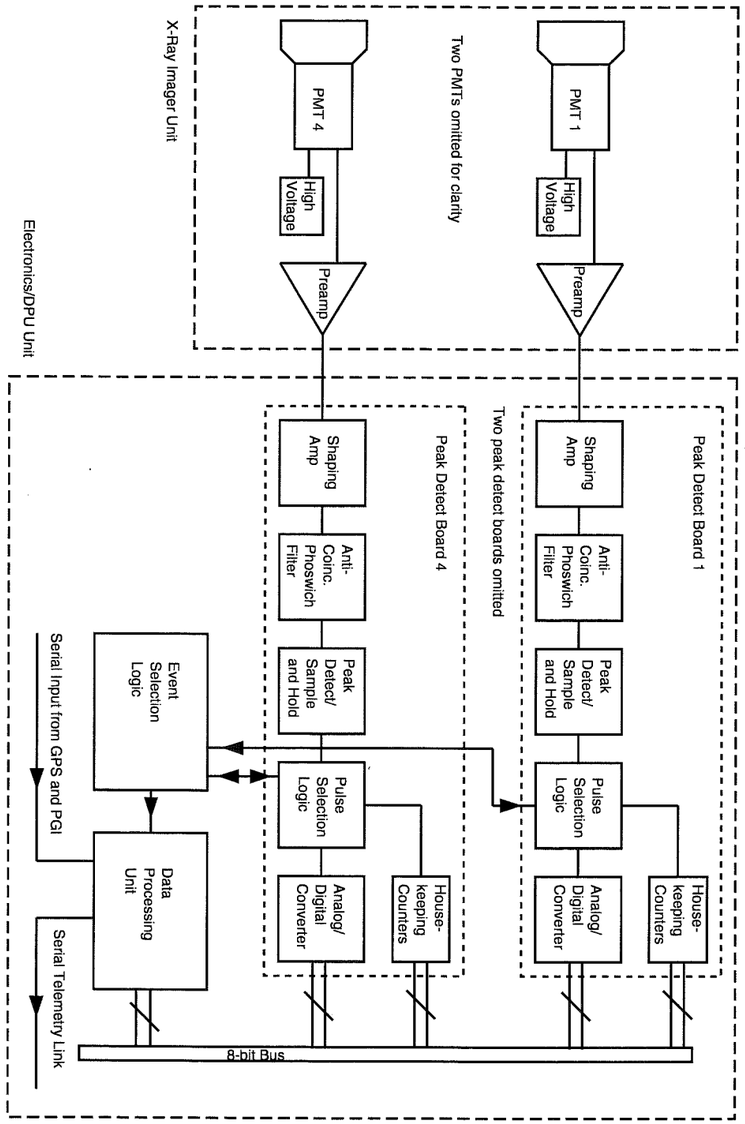

Figure 2.3: A block diagram of the X-ray imager electronics

the energy range analyzed. The high-level threshold also ensured that no high-energy X-ray pulses passing through the walls of the lead collimator would be analyzed. The peak detect boards also looked for cosmic-ray anti-coincidence signals, as mentioned previously. Since pulses from the plastic scintillator have a much faster rise time than pulses from the sodium iodide scintillator, the peak detect boards could trigger on the fast rise time signal, and cancel any coincident signals. In addition, the peak detect boards looked for pile-up events, when two pulses arrive too closely together for their individual energies to be measured accurately. The peak detect boards cancelled these events as well. Programmable logic Actel chips on the peak detect boards determined if a given PMT pulse satisfied the necessary criteria. The Actel chips also kept statistics on how many pulses did and did not satisfy the criteria, and for what reasons.

All four peak detect boards were connected to a single logic board, which determined if an X-ray event was satisfactory. After the Actel logic chips on the four individual peak detect boards had determined that each individual PMT pulse was satisfactory, a fifth Actel chip on the logic board determined whether an X-ray event was satisfactory. That is, a satisfactory X-ray event must have been observed in the correct energy range by a minimum of three tubes, and no anti-coincidence or pile-up signal could have occurred on any peak detect board. The three-tube criteria was used because only three independent measurements were needed for position determination. If an event was determined to be satisfactory, the logic board signaled the DPU board.

The DPU board used an Analog Devices ADSP 2101 microcontroller to control the instrument, process data, and produce a telemetry signal (clock and data or pulse-code-modulated (PCM) signal). A Motorola MC6811 microprocessor took care of serial communication with programming devices and with the Global Positioning System (GPS) and Polar Geophysical Institute (PGI) instrument. Two DPU Actel chips controlled communication with the four peak detect boards, the logic board, and the telemetry interface.

Flight software was written in the ADSP 2101 assembly language. The software operated asynchronously, since the X-ray events occurred randomly in time, and the DPU needed to process each event as it came in. The DPU software waited until the logic board had generated an interrupt, before reading an 8-bit number from each of the peak detect

boards. X-rays were processed, stored and sent down as four 8-bit numbers. No image processing was done on board the balloon, limiting the count rate to 416 X-rays per second, because telemetry was sent at about 16 kbits/second. Any X-ray events beyond 416 per second were thrown away, although a total count rate was recorded. The DPU software also read the housekeeping statistics from each of the four peak detect boards and recorded them once per frame.

Data frames were generated approximately four times per second, limiting the time resolution of the instrument to 0.25 seconds. The flight software packaged the data into 512-byte frames, and sent out clock and data signals to the telemetry system. Once per frame the flight software also checked the GPS system and recorded the time, attitude and restitution. Once per second, the flight software read in data from the PGI instruments.

In addition to the flight electronics, a ground station was needed in order to decode the telemetry signals from the imager and store them, for calibration purposes as well as in-flight monitoring of the imager. This function was supplied by reprogramming a spare DPU board into a PCM decoder. The PCM decoder then output data serially in RS232 format into a PC for further processing.

2.1.3 Calibration Procedure

The calibration procedure for the X-ray imagers involved a number of different steps, and was carried out both before and after the balloon flights. The first step was to measure the gain of all the PMTs without their associated electronics, and determine what high voltage setting was optimal for each. We chose to set each PMT to produce 1.5 $\times 10^5$ electrons per visible photon, which gave a preamplifier output of 20 mV per keV. The individual high-voltage supplies were adjusted accordingly, before the tubes were coupled to the scintillator.

After coupling to the scintillator, the four PMT gain settings were checked again, using X-ray sources of known energy such as Cadmium-109 (22 keV), Americium-241 (60 keV), and Cobalt-57 (122 keV). The X-ray source was placed in a lead collimator, limiting the X-ray source to a spot 0.64 cm in diameter. The collimated X-ray source was held over the same relative position above each tube, and a commercial multi-channel analyzer was used

to measure the gain of each tube. Even though the gains of the PMT and scintillator system should in principle have all been uniform, in practice they differed by up to 20%. The unequal gains were believed to be due to irregularities in the scintillator and the coupling to the PMTs. The high-voltage supplies were again adjusted to equalize the four PMT gains. The peak detect boards were also adjusted and calibrated independently from the PMTs, primarily due to a shortage of time.

After the last hardware gain adjustment was believed to have been made to the PMTs and peak detect boards, final calibration data was collected over a grid of 64-pixels for input to the image-forming algorithm. A grid of 64 square pixels of size 2.9 $\times$ 2.9 cm^2 was chosen, because the spatial resolution of the imager was limited to the size of the pinhole, 2.9 $\times$ 2.9 cm^2. An automated X-Y positioning system built from a converted X-Y plotting table was used to facilitate the collection of grid data for all four imagers. Cadmium and cobalt sources were placed one at a time in the test collimator, and the automated positioning system held the sources over the center of each pixel while data was recorded.

The 64-pixel calibration was completely redone following the balloon campaign, because the peak detect boards had been changed after the preflight calibration. Americium was used for this calibration since it was found that a single calibration with a 60 keV peak gave more consistent results in the image formation algorithm than two calibrations with higher and lower energy X-rays.

2.1.4 Image Formation Algorithm

Statistical considerations

Forming images from the four PMT responses was a fairly complicated task, because of the statistical nature of PMT-scintillator measurements. Statistical uncertainties in PMT energy measurements translated into statistical uncertainties in the position of each X-ray interaction. The following example illustrates the limitations of the instrument. Typical efficiencies for sodium iodide scintillators are about 11% [*Knoll*, 1989], so only 6.6 keV of the energy of a 60 keV X-ray will be converted into light. Since the scintillator produces

primarily blue photons, which have energies of about 3 eV, about 2200 visible photons will be produced. Assuming the coupling between the scintillator and PMT is 100% efficient, then 2200 photons will reach the PMT photocathode, which has a quantum efficiency of about 25%. So the photocathode will convert only about 550 visible photons into electrons to be multiplied. Since the process is governed by Poisson statistics, one standard deviation will be $\sqrt{550}/550$ or 4%, which gives a resolution of 10%. (The resolution is the full width at half maximum over peak energy and the FWHM is 2.35 times the standard deviation.) Because the X-ray imager uses a square crystal and four PMTs, the coupling is not 100% efficient, and the actual resolution for a 60 keV X-ray is somewhat worse. Near the center of the imager, the resolution is about 15% and near the corners of the imager, the resolution is about 17%.

This limited energy resolution means that any single measurement of the energy or position of an X-ray event will have a fairly large error associated with it. In order to be more confident of energy and position measurements, a large number of X-ray events are needed. Figure 2.4 shows how the tube response to a collimated 60 keV X-ray source varied with the position of the source. When the X-ray source is directly over the tube, the energy of the peak is highest, and the resolution is best. When the source is not over the tube, the energy of the peak is lower, and the resolution is worse.

Position determination

The calibration data for the 64 pixels gives the conditional probabilities of various PMT responses (measured X-ray energies) given the known source locations. In order to form images, we need the conditional probabilities of the various X-ray positions for any given set of of 3 or 4 PMT responses. To convert the calibration data into a table that can be used to look up the conditional probabilities needed for imaging, Baye's Rule [*Rice*, 1995] was used.

$$P(X_j|\vec{Q}_k) = \frac{P(\vec{Q}_k|X_j)P(X_j)}{\sum_i P(\vec{Q}_k|X_i)P(X_i)} \tag{2.1}$$

Here, $\vec{Q}_k$ is the discrete outcome vector, or PMT response. It is a four-component vector, where any component can have an integer value between 0 and 255 (the output of the

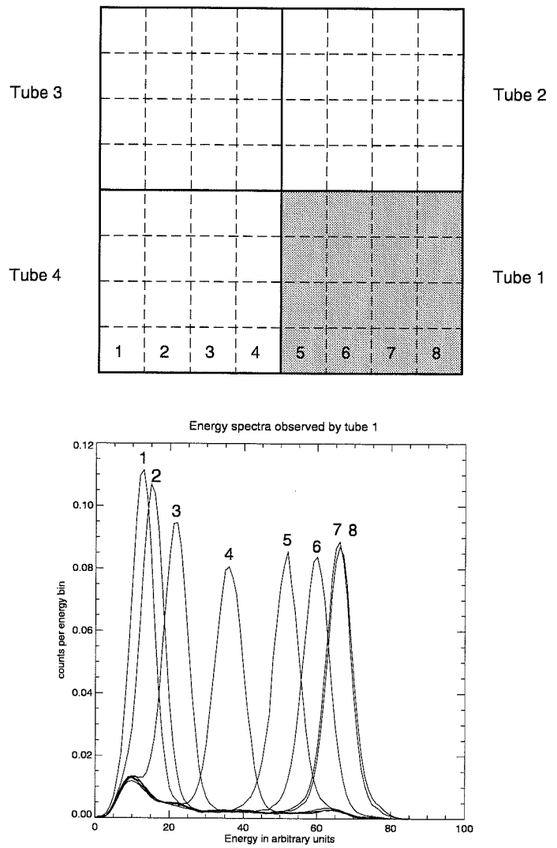

Figure 2.4: Variation in X-ray imager response with position. In the upper panel, the numbered pixels show the eight positions where a collimated 60 keV X-ray source was placed for this test, and the shaded region shows the location of tube whose response is plotted in the lower panel. The peaks with the highest energies were obtained when the X-ray source was directly over the tube. The small peak at low energies is from the 25 keV Am-241 line.

analog-to-digital converter). X_j is an integer between 1 and 64, which gives the discrete position, or pixel, over which the calibration source was located. $P(\vec{Q}_k|X_j)$ is the conditional probability of some PMT response, $\vec{Q}_k$, given an initial position X_j. This conditional probability was measured in the calibration for each pixel. Since we do not have any information about the probability distribution $P(X)$, we assume it is uniform and equal to 1/64, or that the X-rays are equally likely to interact in any pixel. $P(X_j|\vec{Q}_k)$ is the conditional probability that an event occurred over some position, X_j, given a PMT response, $\vec{Q}_k$. This conditional probability is used to create the images.

Using equation 2.1, and approximating the calibration data by fitting Gaussian functions to the actual tube responses, it was possible to write a computer program to read in the calibration data for each pixel, $P(\vec{Q}_k|X_j)$, and generate a look-up table, $P(X_j|\vec{Q}_k)$, where the the observed PMT responses could be easily plugged in to find the probabilities of where any X-ray event was likely to have occurred.

Using this look-up table, images can be formed from a group of X-ray events by one of two methods. In the first method, a single X-ray event can be assigned to the single pixel where it was most likely to have occurred. A second method allows a single X-ray event to be distributed over the entire image based on the probability of its occurrence in each pixel. That is, if there is a 0.50 probability of a given event occurring over a certain pixel, then 0.50 X-rays will be added to that pixel. Images are made by summing up the number of whole or fractional X-rays that land in each of the 64 pixels. Both methods were investigated by making images out of the calibration data, but the second method, the distribution by probability, gave better images. Because of the limited resolution of the instrument, particularly near the edges of the imager, some X-ray events will be equally likely to have occurred in more than one pixel. Therefore, the distribution by probability gives smoother images.

Several features of the instrument were used to simplify the look-up table. As described above, the calibration data $P(\vec{Q}_k|X_j)$, would be an array of size $64 \times 256 \times 4$, and the look-up table, $P(X_j|\vec{Q}_k)$, would be an array of size $256^4 \times 64$. These arrays were too large to work with practically. Since a minimum of three non-zero PMT responses were needed to describe a position, the algorithm was designed to work with exactly three responses. In the

case where four non-zero PMT responses were observed, only the three largest responses were used. For position finding, the sum of all the PMT responses was not needed, only the relative sizes of each. (The sum of all four PMT responses does give the energy of the incident X-ray, however, and this information was preserved separately.) Therefore, the sum of the three PMT responses was normalized to 100. This procedure allowed us to use only two of the three PMT responses in the look-up table, since the third was limited by the normalization. Using only integer responses also reduced the possible values for the PMT response from 256 to 100, which was acceptable, given the resolution of the instrument. The possible PMT responses were further reduced from 100×100 to 75×50, by consideration of the three-tube minimum and the low- and high-level thresholds on the electronics. In addition, the eight-fold symmetry of the instrument allowed us to further simplify the look-up table, although the tubes were not identical enough to have only one look-up table for all of the tubes. It turned out to be fairly easy to distinguish which tube an event was likely to have occurred over, but it was more difficult to determine which pixel an event occurred over if the event was near the corner of the imager. Thus, there was a separate look-up table for each tube.

Using the look-up table resulted in acceptable 64-pixel images of laboratory X-ray data in units of X-ray number flux per pixel, as shown in Figure 2.5. This figure shows that spatial resolution is about one pixel near the center of the imager, but about two pixels near the edge of the imager. These variations in spatial resolution with position occur because of light loss and reflection effects near the edge of the crystal, and because energy resolution of the individual PMTs depends on the amount of light detected. For an X-ray event near the edge of the imager, one PMT will detect a large amount of light, but the other three will detect very small amounts of light. The uncertainties in the measurements of the three PMTs that detect the smaller amounts of light will result in uncertainties in position. For an X-ray event occurring near the center of the imager, all four PMTs will detect moderate amounts of light, and the uncertainties in position determination will be less than for the edge case.

The energy spectra shown in Figure 2.5 also show that the energy response varies over the face of the imager. Lower energies are detected near the edge of the imager, probably

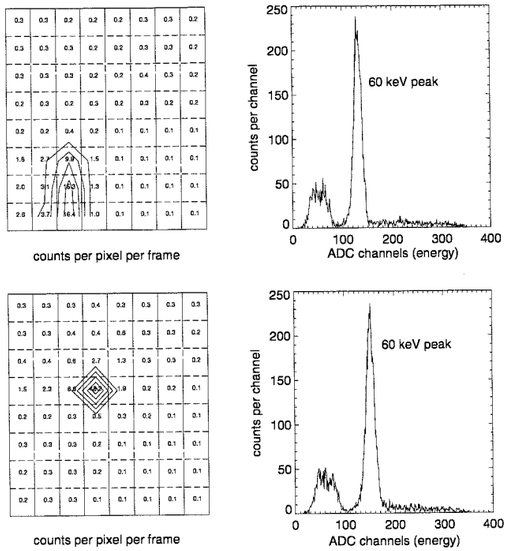

Figure 2.5: Two typical images and spectra made by holding a collimated Am-241 calibration source over individual pixels. Note that the spatial resolution of the instrument is about one pixel near the center of the imager, but about two pixels near the edge. The energy resolution is about 15% near the center and 17% near the edge.

because the diffuse reflector is not perfect, and light is absorbed in the scintillator and light pipe housing. This energy-position dependence is unimportant for making images, since it was assumed that light loss was uniform for all tubes, and PMT responses were normalized before being used to determine position. However, an energy-position correction is required to form energy spectra. Figure 2.6 is a contour plot showing how the peak energy varies across the face of the imager for a known X-ray source.

In addition to corrections to energy spectra, several other corrections are needed for producing images of the aurora. Due to the size of the pinhole and the strength of typical laboratory calibration sources, it was not possible to simulate auroral conditions in the lab, so the calibration images shown in Figure 2.5 were made without using the pinhole collimator. The software adjustments needed to create auroral images are for: geometric factor, despinning, corners, atmospheric absorption, and background subtraction. No corrections for decrease in scintillator efficiency with temperature are needed, since the crystal temperature was 20 degrees C at the time of the REP event. No corrections for dead-time are needed since the count rate was well below the instrument capabilities during the REP event. There are, however, additional corrections for instrumental problems that are only needed for the imager that flew on flight 1 and observed the relativistic electron precipitation event.

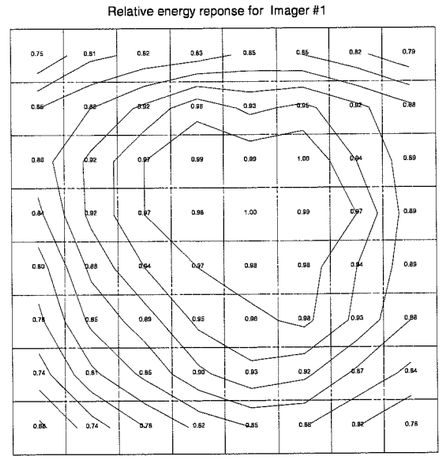

Figure 2.6: Relative energy response at various positions over the face of the imager.

Geometric factor correction

The correction for geometric factors adjusts for the fact that pixels of equal area view different solid angles, depending on their distance from the pinhole. A geometry factor per unit area is approximated using $A_p cos^2\alpha/d^2$ where A_p is the area of the pinhole, d is the distance between the pixel and the pinhole, and α is the angle between vertical and the direction of view.

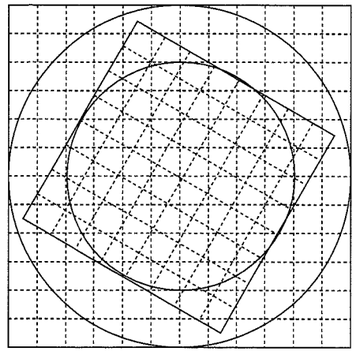

Figure 2.7: The small 8×8 pixel square shows the size of the sky viewed by the imager at one instant. The large circle shows the area of sky viewed by the imager in one revolution. The small circle shows the area of sky that is continuously viewed by the imager.

Despinning and corner correction

Since the balloons rotated at about 3 times per minutes in order to remove offsets in electric field measurements, the X-ray imagers actually observed a circular area of sky that was larger than the square field of view of the imager, as shown in Figure 2.7. To despin the data, each frame is rotated by the appropriate angle, and the square 8×8 pixel image is mapped to a stationary 12×12 pixel image that covers the circular region of sky viewed by the imager. All the pixels used still have the same size as the pinhole, to reflect the spatial resolution of the instrument. The despinning process is flux conserving, in that the flux in each pixel is mapped to the four pixels nearest to the new position and weighted according to the distance from each. Since the corners of the imager can only view a small part of the sky at one time, there will be a corner correction to the count rate for parts of the image that are not continuously viewed by the imager.

Atmospheric absorption

Although stratospheric balloons float at about 35 km, above the most dense layers of the atmosphere, the air above the balloons is still thick enough to absorb and scatter some of the X-rays that travel down from their production region at auroral altitudes. As the X-rays

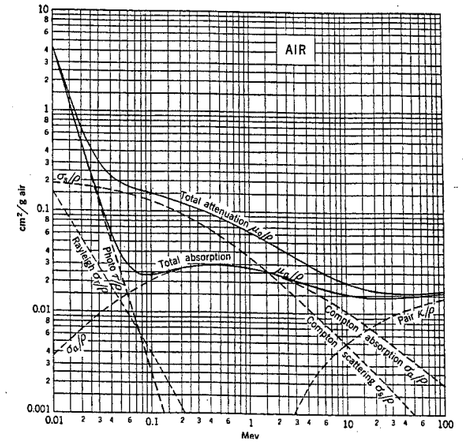

Figure 2.8: Mass attenuation coefficients for air, from *Evans* [1955].

travel down to the balloon, they can undergo a number of different attenuation processes, the most significant being photoelectric absorption and Compton scattering. The probability of these interactions depends on the energy of the X-rays and how much material lies between the source and the detector. The following formulas describe the effect of these two processes.

$$\frac{I}{I_0} = e^{-(\mu_a/\rho)(t\rho)} \tag{2.2}$$

$$\mu_a/\rho \approx \tau/\rho + \sigma_s/\rho \tag{2.3}$$

where I_0 is the initial X-ray photon intensity, I is the residual intensity of unaffected photons, μ_a/ρ is the total mass attenuation coefficient, τ/ρ is the mass attenuation coefficient for photoelectric absorption, and σ_s/ρ is the mass attenuation coefficient for Compton scattering, t is the thickness of the material and ρ is the density. Figure 2.8 gives values for these coefficients for various energies from *Evans* [1955].

Figure 2.8 shows that photoelectric absorption and Compton scattering are the most significant processes at energies between 20 and 120 keV. Also, low energy X-rays are much more likely to experience photoelectric absorption than high energy X-rays. Using

values from this plot, we can determine what fraction of auroral X-rays will actually reach the balloon unaffected by the atmosphere. For X-rays traveling straight down to altitudes of 35 km, which corresponds to an atmospheric depth of 5.7 gm/cm^2 [*Berger and Seltzer*, 1972], 94% of 20 keV X-rays and 1% of 120 keV X-rays will undergo photoelectric absorption while 64% of 20 keV X-rays and 25% of 120 keV X-rays will undergo Compton scattering. Because the atmospheric density decreases exponentially with height, it is very important to know the exact altitude of the balloon, but much less important to know the altitude at which the X-rays were created.

Since more low energy X-rays are absorbed than high energy X-rays, and typical auroral X-rays have exponentially falling spectra, a maximum in the X-ray spectra will occur at around 50 keV. Figure 2.9, from *Barcus and Rosenberg* [1966], shows how the atmosphere would affect a typical auroral electron spectrum. This figure illustrates the electron spectrum incident on the the top of the atmosphere, the X-ray spectrum produced at the top of the atmosphere, and the X-ray spectrum observed at balloon altitudes.

In order to create images of the X-rays produced at auroral altitudes, a correction is needed to account for attenuation by the atmosphere. Photoelectric absorption has the effect of removing X-rays from the images and spectra and is a significant effect that must be accounted for. The correction for photoelectric absorption varies with position. X-rays that land away from the center of the imager will have traveled a greater distance through the atmosphere than those landing near the center of the imager. X-rays landing near the edge of the imager will have had a greater probability of being photoelectrically absorbed before reaching the imager. Therefore, different correction factors are needed for different positions on the X-ray imager in order to create images of the X-ray flux at the production region.

Although Compton scattering is also significant for X-ray in the energy range 20-120 keV, it is difficult to correct for without knowing the spatial distribution of the X-ray source. If the X-rays originate from a small source, then Compton scattering smears out the images, and removes some X-rays from the detection region. However, if the X-rays originate from a larger source, some X-rays will be scattered into the detection region and some will be scattered out of it. Since we do not know the spatial distribution outside the field of view

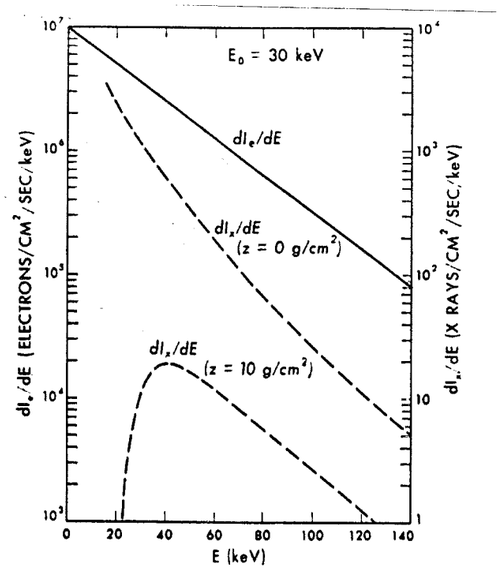

Figure 2.9: Typical electron and X-ray energy spectra, from *Barcus and Rosenberg* [1966]. dI_e/dE is the differential energy flux of incident electrons. dI_x/dE is the differential energy flux of X-rays at the top of the atmosphere ($z = 0$ g/cm^2) and at balloon altitudes ($z = 10$ g/cm^2).

of the X-ray imager, the second assumption is more reasonable, and Compton scattering is ignored in the image processing.

We use images of the X-ray flux at the production region in studying spatial characteristics of auroral electron precipitation. However, in order to really understand the processes that create the aurora, it is also useful to look at the shape of the energy spectrum for the precipitating electrons. The shape of the electron energy spectrum can provide clues to the type of mechanism that accelerates the electrons. For example, an exponential spectrum is given by

$$dI_e/dE = Ae^{-E/E_0} \tag{2.4}$$

where dI_e/dE is the differential intensity of the incident electrons, A is a constant, E is the electron energy and E_0 is the e-folding energy. This form indicates that the electrons origi-

nated in a Maxwellian velocity distribution in thermal equilibrium. A power law spectrum

$$dI_e/dE = BE^{-\gamma} \tag{2.5}$$

where, B and γ are constants, indicates a non-thermal process. Some spectra display different functional forms at different energies, indicating multiple sources. It is possible to obtain information about the precipitating electron spectra from the X-ray imager by assuming a functional form for the electron spectrum, calculating the X-ray production from this spectrum, and comparing the calculated X-ray spectrum to the observed X-ray spectrum. Such calculations can be approximated analytically for certain functional forms [*Barcus and Rosenberg*, 1966], but more complicated forms are usually studied using Montecarlo techniques.

Background subtraction

Background images and spectra made during quiet time on the flight may be subtracted from the final images and energy spectra. For the relativistic electron precipitation event, the background was taken to be the sum of two fifteen minute periods, beginning one hour before the event began and one hour after the event ended.

Correction to instrumental problems

A problem that affected only one of the four imagers was present on the first balloon flight. This problem needs to be described since it occurred during the time when the relativistic electron precipitation was observed. In this particular imager, the anti-coincidence plastic detector was not functioning properly for one of the four PMTs. In the malfunctioning PMT electronics, many 'good' X-ray events were mistakenly cancelled because these events were thought to be 'bad' plastic cosmic-ray events. Therefore, this particular tube recorded many fewer X-ray events than the other three tubes. Because the effect was energy dependent (more events were rejected at higher energies) it was also spatially dependent (more events were rejected near the corners of the problem tube). The problem was studied in detail with the recovered instrument, and it was determined that data from events that

occurred over the problem tube could not be used, but that data from over the three functioning tubes could be used. Therefore, images were constructed from a spinning L-shaped imager, rather than from a spinning square imager. Therefore the exposure time for each image is longer, since the count rate is reduced, but the overall image is not compromised.

Images are initially plotted in units of X-ray counts per pixel. Because of the effects of corners, geometric factor and atmospheric absorption, there will be more counts detected near the center of the image than at the edges of the image. Variations in the number of counts detected affects the Poisson statistics. The error associated with each pixel, $\sqrt{n}/n$, is determined before the correction factors are applied. Afterwards the correction factors for energy-position dependence, geometric factor, corners, and background are applied, and the final images are plotted in flux units of counts/cm^2-ster-sec.

2.2 The Germanium X-Ray Spectrometer

The germanium X-ray spectrometer was provided by the University of California at Berkeley (UCB). It was originally designed for astrophysical gamma-ray observations [*Johns and Lin*, 1992; *Smith et al.*, 1995], but was modified for auroral observations by lowering the upper end of its energy range to 1.4 MeV, and reducing the field of view of the instrument.

The germanium spectrometer is a coaxial solid state detector 5.5 cm tall with a diameter of 5.5 cm, illustrated in Figure 2.10. It is cooled by liquid nitrogen and has an extremely high energy resolution of about 2 keV FWHM [*Foat et al.*, 1998]. The detector is segmented into two parts, D0 and D1. Only data from D1 was used for the INTERBOA campaign. A lead collimator restricts the field of view of the germanium spectrometer to 90 degrees (narrower than shown in Figure 2.10) to match that of the X-ray imager.

Johns and Lin [1992] have derived a method for direct inversion of bremsstrahlung data to electron data. Their method requires extremely high resolution X-ray energy spectra, such as spectra from germanium detectors. The inversion method involves inverting the following integral for bremsstrahlung emission

$$\frac{dJ(k,t)}{dk} = \frac{1}{4\pi R^2}\int_V n(\vec{r},t)\int_k^\infty \frac{dJ_e}{dE}(E,\vec{r},t)\frac{d\sigma}{dk}(k,E)\,dE\,dV \tag{2.6}$$

where dJ/dk is the differential X-ray flux with photon energy k at time t, R is the distance

to the source, V is the volume of the source, n is the density of hydrogen at position $\vec{r}$ and time t, dJ_e/dE is the differential electron flux with electron energy E at position $\vec{r}$ and time t, and $d\sigma/dk$ is the differential cross section for bremsstrahlung of photons with energy k from electrons of energy E. The adjustment for nuclei heavier than hydrogen is made in $d\sigma/dk$.

To determine the electron spectrum, dJ_e/dE, from the observed X-ray spectrum, dJ/dk, this integral must be inverted. In order to invert the energy integral, numerical approximations to the bremsstrahlung cross section are used. Also the energy bins of the observed X-ray spectrum dJ/dk, must be much narrower than the energy bins of the desired electron spectrum dJ_e/dE. This criterion is satisfied for the extremely high resolution data obtained from the germanium detector, but energy spectra from the more widely used sodium-iodide spectrometers do not have high enough resolution to be used with this procedure. The direct inversion of the volume integral also requires input about the spatial distribution of the X-ray precipitation region for the most accurate results. This spatial information is provided by the X-ray imager, and can result in higher electron energy resolution than has been observed previously from balloons.

2.3 Other Balloon Instruments

Other balloon instruments included the VLF antenna provided by the University of Washington (UW). This instrument was originally designed for a rocket experiment to study auroral microbursts [*Skoug*, 1995]. It was a magnetic loop antenna designed to measure waves in the frequency range 0.5-8 kHz with amplitudes greater than 1 pT. Although the instrument functioned through three flights and recoveries, no data of interest was obtained. The instrument was probably not sensitive enough to waves that had propagated down through the ionosphere and upper atmosphere.

The CESR provided three-axis electric and magnetic field instruments. The five electric field booms made measurements of E_x, E_y and E_z between 1-500 mV/m. In order to reduce offsets on the horizontal components, the balloon payload rotated at 3 revolutions per minute. A fluxgate magnetometer made measurements of B_x, B_y, and B_z between

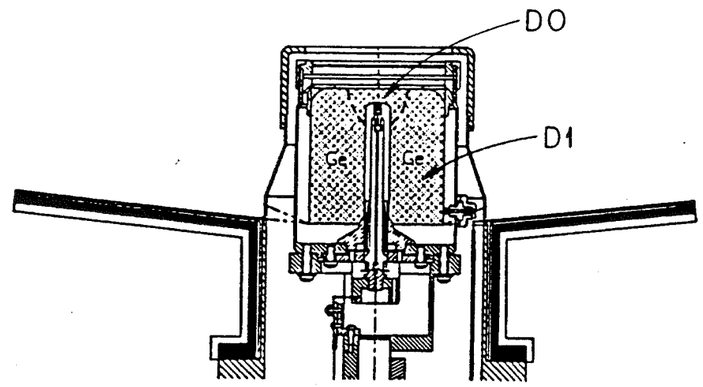

Figure 2.10: The germanium X-ray spectrometer, from *Smith et al.* [1995]. For the INTERBOA campaign, the lead collimator was much narrower, restricting the field of view to 90 degrees and only data from detector D1 was used.

1-60000 nT. However, in order to separate variations in the B_x and B_y components, due to payload motion and due to auroral phenomena, it is necessary to know the attitude of the balloon payload. A four-antenna GPS system designed to measure attitude was present on the balloon, however, it only functioned for the first 35 minutes of flight 1. Therefore, only a single northward horizontal component could be determined by taking the maximum of B_x or B_y during a revolution.

PGI provided an X-ray spectrometer that used a single scintillator and PMT. It measured X-rays in the energy range 20-200 keV in ten channels, with a field of view of 90 degrees, the same as the X-ray imager and the germanium detector. The functions of this instrument overlapped those of the germanium spectrometer on the first flight. A PGI Geiger-Muller counter was also present on all three flights.

Chapter 3

RELATIVISTIC ELECTRON PRECIPITATION DATA

3.1 Overview of Balloon Flights and Geophysical Conditions

Three stratospheric balloons were launched within a two-week window in August 1996, with the purpose of studying auroral phenomena. The launch dates were selected to coincide with favorable meteorological conditions, predicted geomagnetic activity and optimum satellite positions. Within these constraints, we were able to launch three out of four prepared balloon payloads, to collect almost one hundred hours of data, and to recover all three payloads successfully.

We chose a launch window during the stratospheric wind turn-around period in order to allow the balloons to remain close to the launch site, improving data collection and chances for payload recovery. This wind turn-around occurs twice per year and is characterized by a change in direction of prevailing winds from west to east and back again. During this turn-around period, the winds at 35 km altitude were slow, so the balloons remained between geomagnetic latitudes of 62.8° and 65.6° and within about 300 km of the launch site near Kiruna, Sweden.

In the interest of observing auroras, launches were timed to coincide with predicted geomagnetic activity. However, the conditions during the two-week launch window were moderately quiet, with K_p of less than or equal to 4-. Figure 3.1 shows magnetometer data from Kiruna for all three flights (courtesy of Ingemar Haggstrom, Swedish Institute of Space Physics). Virtually no magnetic activity was observed over Kiruna during the first flight. Moderately small auroral substorms were observed during the second and third flights.

Despite these moderately quiet geomagnetic conditions, periods of X-ray activity were observed on all the three flights. Figure 3.2 shows summary count rates from the X-ray im-

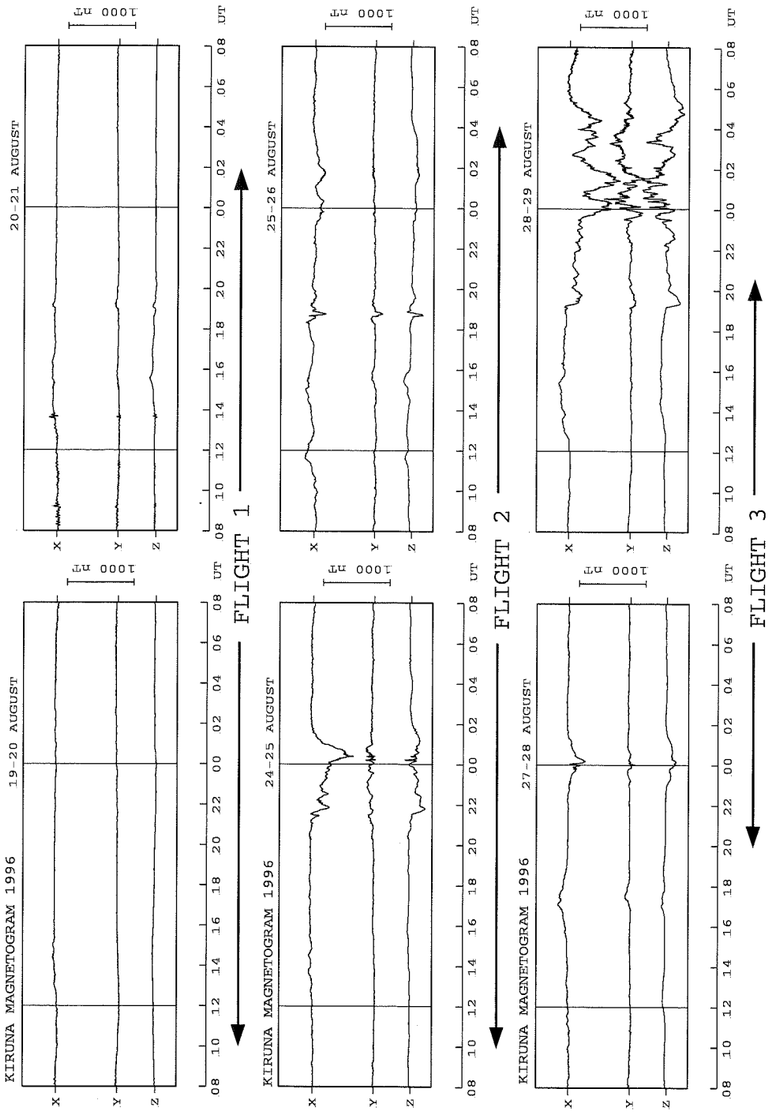

Figure 3.1: Magnetometer data from Kiruna, courtesy of Ingemar Haggstrom, Swedish Institute of Space Physics. Substorm activity is visible in data from the second and third flights.

ager for all three flights. There were three noteworthy X-ray events during the campaign. The first event occurred near 1530 UT on August 20, 1996. The X-ray imager detected count rates up to 5 times the background level at this time. The germanium detector observed a similar increase and identified it as a relativistic electron precipitation (REP) event. The second X-ray event occurred near 0030 UT on August 25, 1996, during a period that ground-based magnetometers identified as a substorm. Unfortunately, the balloon altitude at the time of the event was about 32 km, which is too low for good X-ray image production. The third X-ray event also occurred during a substorm, near 0000 UT on August 28, 1996. The germanium detector did not fly on the second and third flights and therefore did not observe these events. Because the best data were obtained for the REP event, and also because these REP observations were somewhat unusual, this dissertation focuses on that event alone.

The balloon launches were also timed so that spacecraft such as WIND and Polar would be in position to provide coordinating data. For example, the WIND satellite was scheduled to pass though its perigee in the Earth's magnetotail on August 19, 1996, so a balloon was launched on this date. Although the balloon observed no activity while WIND was in the tail, several other satellites provided useful data correlated with the August 20, 1996 REP event. As we have chosen to focus on this event, we describe only those satellite and ground based measurements that appear to be related to the REP event. The Polar satellite was conveniently in position to view the north pole during the largest three X-ray events observed. Other useful data were obtained from three Los Alamos National Laboratory (LANL) geosynchronous satellites and from Scandinavian ground-based magnetometers and riometers. Table 3.1 summarizes the experiments that observed phenomena related to the REP event. At the time of the REP event, K_p was 2. Positions in magnetic coordinates were determined using the *Tsyganenko* [1989] magnetic field model, for this value of K_p (courtesy of R. Elsen).

This chapter describes in detail the observations that were related to the August 20 REP event. We begin with observations from the balloon-borne instruments, then cover measurements from the ground-based magnetometers and riometers, and finally present related satellite observations of various regions of the magnetosphere.

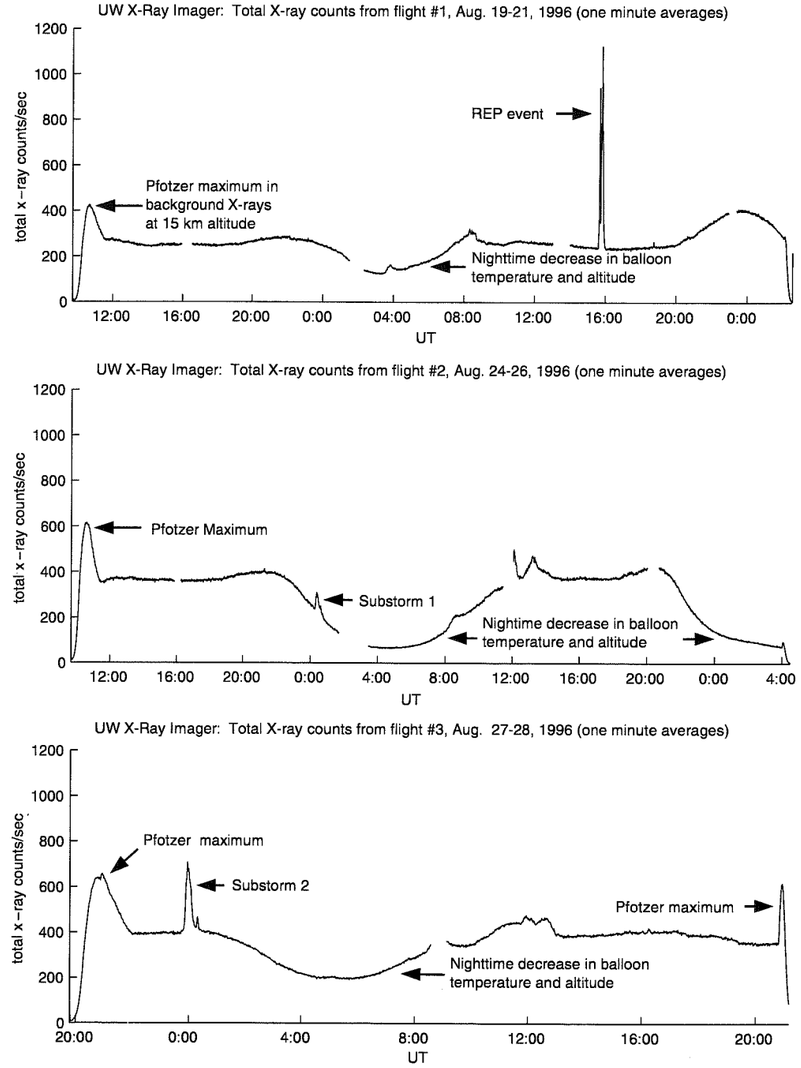

Figure 3.2: Total X-ray counts from all three balloon flights, measured by the X-ray imager. The gradual changes in the background count rate were due to changes in temperature and altitude.

Table 3.1: Experiments observing the Aug. 20, 1996 REP event at 1530 UT.

Name of Experiment	Geographic Latitude	Geographic Longitude	Magnetic L-shell	Magnetic Local Time
INTERBOA	68.4	21.7	5.8	1833
LANL 1990-095	0	323	~6.6	1254
LANL 1991-080	0.3	69.6	~6.6	1952
LANL 1994-084	0.6	102.7	~6.6	2210
Esrange magnetometer	67.9	21.1	5.6	1829
Kilpisjärvi riometer	69.1	20.8	6.1	1833
WIND satellite	Outside bow shock at $X_{GSE} = 14\,R_E, \quad Y_{GSE} = -16\,R_E, \quad Z_{GSE} = -2\,R_E$			
Polar satellite	Above north pole at 7 R_E altitude			

3.2 Balloon Data

3.2.1 X-Ray Imager Observations

Figure 3.3 shows variations in X-ray count rate measured by the X-ray imager for the REP event. The event lasted about 20 minutes. The plot shows large modulations with periods of 100-200 seconds, and smaller modulations with periods of about 10-20 seconds. Similar temporal signatures were observed by both of the other X-ray instruments on the balloon. At the beginning of the event at 1532 UT, the balloon was at 34.8 km altitude, geographic latitude 68.4° and longitude 21.7°. This location corresponds to 1835 magnetic local time (MLT), 65.5° magnetic latitude, and an L-shell of 5.8.

A series of X-ray images made from this event are shown in Figure 3.4. These images have been corrected as described in Chapter 2, and represent the X-ray flux at the X-ray production region or the 'top' of the atmosphere. No smoothing between pixels has been done, and the size of the small squares reflects the spatial resolution of the instrument.

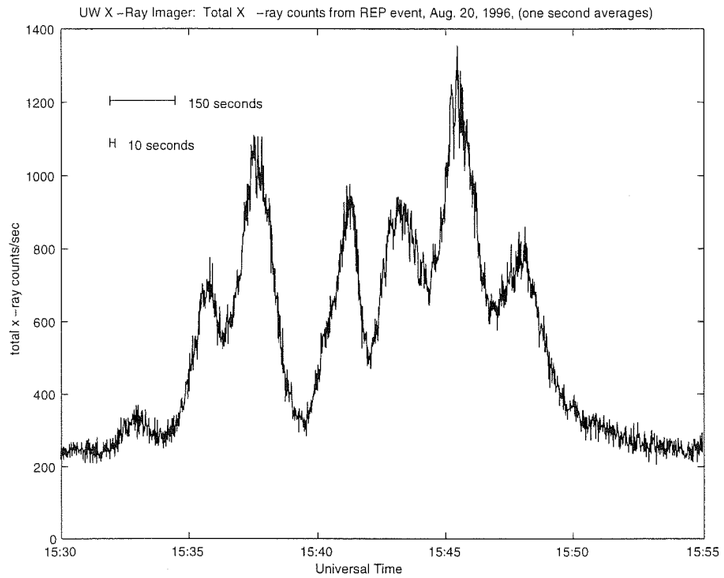

Figure 3.3: Total X-ray counts for the REP event, measured by the X-ray imager.

The diameter of the images shown in Figure 3.4 at the X-ray production region depends on the altitude of this region. The altitude of the X-ray production region depends in turn on the energy of the precipitating electrons. Higher energy electrons will penetrate further into the atmosphere before being decelerated and producing bremsstrahlung radiation. Typical 20-120 keV auroral electrons create X-rays at around 100 km altitude [*Berger and Seltzer*, 1972], where the 90 degree field of view of the X-ray imager corresponds to a circle about 100 km in diameter. Highly relativistic electrons with energies above 1 MeV can penetrate further, to altitudes of around 60 km, where the field of view of the X-ray imager corresponds to a circle about 50 km in diameter. Since observations by the germanium detector (to be discussed later in this chapter) indicate that the precipitating electrons had MeV energies, the images shown in Figure 3.4 have a diameter of about 50 km.

The exposure time for the images shown in Figure 3.4 is limited by the Poisson statistics

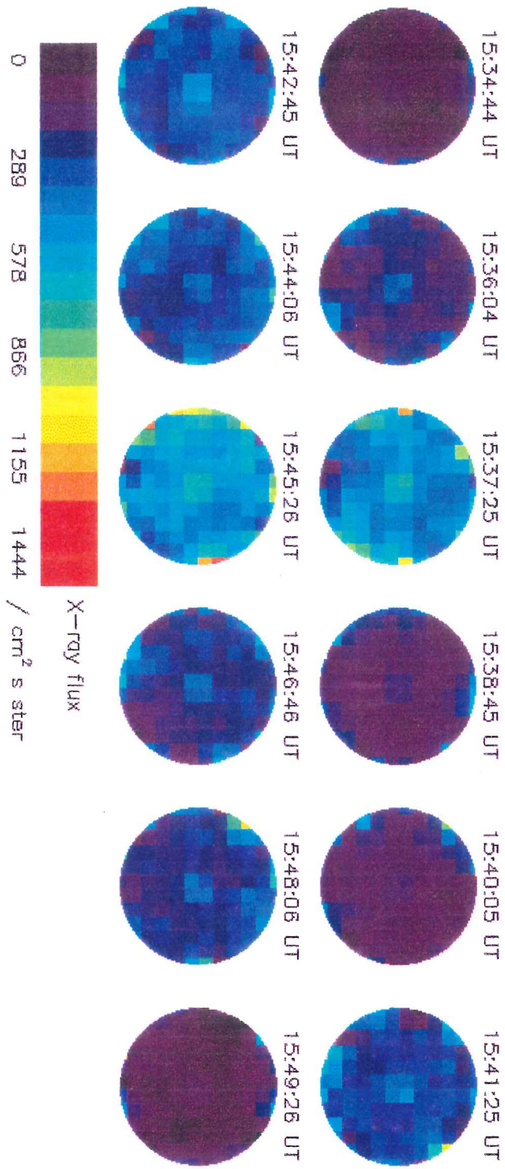

Figure 3.4: This figure shows a series of 80-second X-ray images from the REP event. The images are presented as would be seen from a satellite looking down on the earth, with north at the top. No spatial structure is obvious during the event.

governing the instrument. The 80-second exposure time was chosen so that each pixel would contain enough X-ray counts, n, for one standard deviation, $\sqrt{n}$, to be less than 10% of n. Because of atmospheric absorption, and because the corners of the instrument do not view the entire circle, one standard deviation near the edges is closer to 20% of n. The variations in color shown in Figure 3.4 are less than one standard deviation from pixel to pixel.

The bright spot in the center of the images shown in Figure 3.4 is an artifact caused by the electronic problem discussed in Chapter 2. With the exception of this artifact, the X-ray images show uniform brightening across the field of view with no obvious small-scale spatial structure in the events. The periodic brightening appears to be primarily a temporal feature, since there is no motion in and out or across the field of view.

We looked at the X-ray imager data in several ways in order to determine whether the lack of apparent spatial structure was real or simply a result of temporal and spatial resolution of the instrument. In order to construct images with shorter exposure times, we added several pixels together, sacrificing spatial resolution for temporal resolution. By creating 4 by 4 pixel images from 8 by 8 pixel images, we examined coarse images on 20-second time scales. No spatial structure was found in these images, either, so they are not shown. Another way of analyzing the spatial data is by constructing time series for count rates in different regions of the field of view, and comparing these time series to one another. Figure 3.5 shows time series for the four quadrants viewed by the X-ray imager, with a time resolution of 20 seconds. Even on this time scale, there is no significant difference between the four traces shown. All four traces show the same peaks, and no peak starts earlier in any one quadrant than another. Using this technique, time series were examined for smaller divisions of the image, and for images made up of different energy ranges (>60 keV and <60 keV). None of these techniques revealed spatial variations, either.

3.2.2 Germanium Detector Spectra

Several germanium detector energy spectra from *Foat et al.* [1998] are shown in Figure 3.6. At the bottom is the background spectrum (divided by 100) taken before the event, between 1430 and 1530 UT. The decrease in count rate below about 60 keV is due to

Figure 3.5: Background-subtracted X-ray count rate for each of the four quadrants of the X-ray imager during the REP event.

photoelectric absorption by the atmosphere. The background data also show peaks that are characteristic of lead, germanium, and electron annihilation. These peaks can be used to calibrate the instrument. In the middle of the figure are background-subtracted count spectra taken during the first and second half of the REP event (crosses and diamonds, respectively). A significant flux of X-rays is visible up to the limit of the instrument at 1.4 MeV. Note that the second half of the event is slightly harder than the first half. At the top of the figure, crosses represent the photon spectrum that has been corrected for the atmosphere and the instrument response.

Foat et al. [1998] examined variations in the spectral shape between the peaks and valleys of the event, and found no significant differences. The corrected X-ray spectrum best fits a power law spectrum, $dI_x/dE = BE^{-\gamma}$, with $\gamma = 1.6$ from 100-250 keV and with

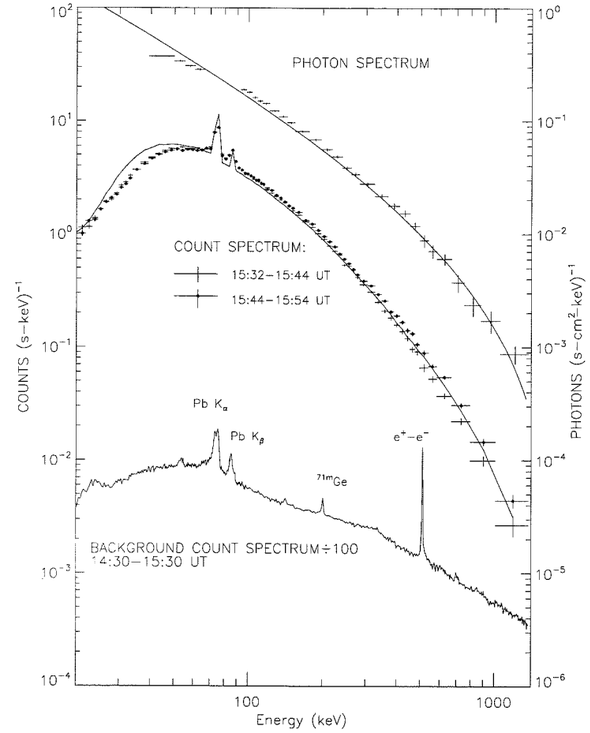

Figure 3.6: X-ray spectra from the germanium detector, from *Foat et al.* [1998]. This figure shows X-ray count spectra at balloon altitudes and the corrected X-ray photon spectrum at X-ray production altitudes. The solid lines show X-ray spectra calculated from an input electron spectrum having a mono-energetic peak at 1.7 MeV.

$\gamma = 2.8$ above 400 keV [*Foat et al.*, 1998]. A single exponential, $dI_x/dE = Ae^{-E/E_0}$, does not fit the entire energy range, but at low energies the e-folding energy, E_0, is approximately 75 keV. As described in Chapter 1, *Rosenberg et al.* [1972] observed X-rays with an e-folding energy of 100-150 keV and *West and Parks* [1984] observed X-rays with an e-folding energy of 200 keV, so the August 20 event is not the hardest X-ray spectrum ever observed. However it is an unusual event in that the X-ray flux was significantly above background up to the instrument limit of 1.4 MeV.

The solid lines in Figure 3.6 represent model calculations of the X-ray spectra at the top

of the atmosphere and at the instrument. The model calculations were made by assuming a form for the precipitating electron spectrum and using bremsstrahlung theory to calculate the X-ray spectrum produced. The shape of the calculated X-ray spectrum for various input electron spectra was then compared to the X-ray observations to find the best fit. *Foat et al.* [1998] found that the observed X-ray spectrum most closely matched X-rays produced by an input electron spectrum with a mono-energetic peak at about 1.7 MeV and a flux of 300 cm^{-2} s^{-1}. The exact energy of the peak has an error of approximately $\pm$ 0.2 MeV (D. Smith, personal communication, 1999). Because the instrument cutoff is at 1.4 MeV, the exact shape of this mono-energetic electron peak cannot be determined, and it could be a narrow spike, a broad Gaussian, or a plateau.

3.2.3 Electromagnetic Field Measurements

Figure 3.7 shows the electric and magnetic fields observed on board the balloon. The large spikes are due to data problems and are not real. No electromagnetic field signatures are directly correlated with the 100-200 second pulsations observed in the X-ray flux. However, the northward electric field component does exhibit 7-8 minute oscillations at the same time as the REP event was observed. This signal appears only in one component of the electric field. Such polarization may indicate oscillation of the field lines, correlated with the X-ray event [*Treilhou et al.*, 1998].

3.3 Ground Data

3.3.1 Magnetometer Data

Figure 3.8 shows Esrange ground magnetometer data from this event (courtesy of L. E. Sarri). Note that the eastward component of the magnetic field fluctuates with a frequency similar to the 100-200 second fluctuations in the X-ray data, but the magnetometer fluctuations are strongest half an hour before the REP event. In addition, there is a small magnetic bay (30 nT) in the northward component of the magnetic field, also half an hour before the REP event. This bay could be the westward expansion of a westward electrojet related

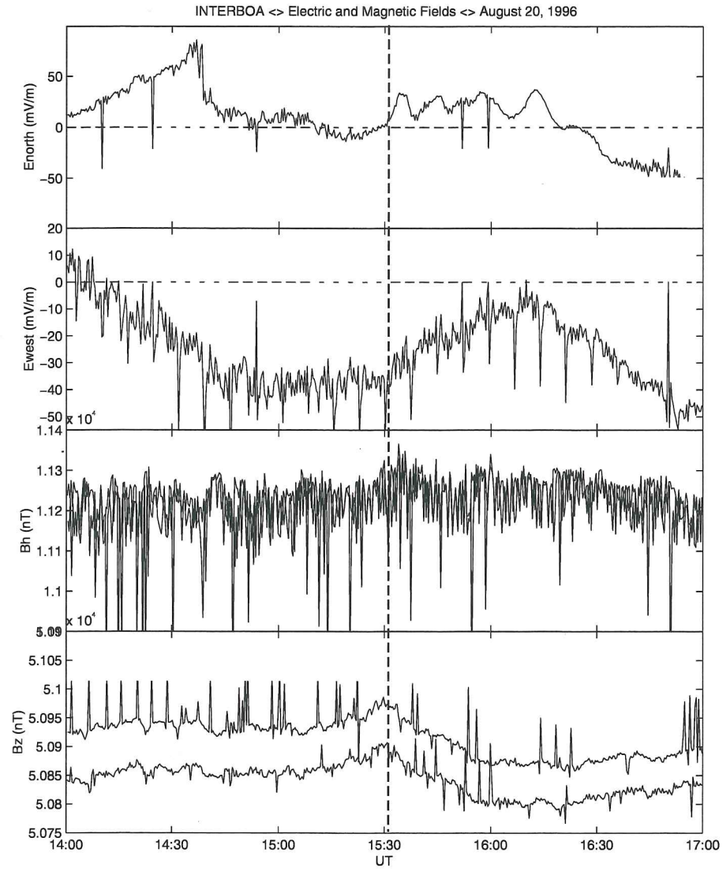

Figure 3.7: Electric and magnetic field data from balloon instruments, courtesy of J. P. Treilhou, CESR, Toulouse, France. The large spikes are due to data problems and are not real. Northward electric field data show oscillations with periods of 7-8 minutes starting at 1530 UT. The start of the REP event at 1532 UT is indicated with a dashed vertical line.

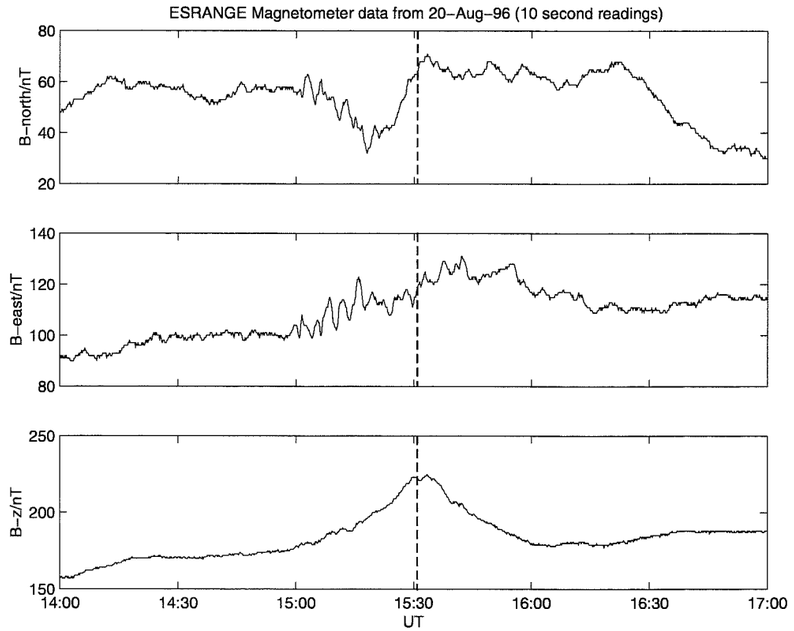

Figure 3.8: Magnetometer data from Esrange, courtesy of L. E. Sarri. The northward component shows a small magnetic bay, and the eastward component shows fluctuations that are strongest about half an hour before the REP event. The start of the REP event at 1532 UT is indicated with vertical dashed lines.

to a distant nightside substorm [*Treilhou et al.*, 1998]. A small nightside substorm was observed in satellite data, and will be discussed later in this chapter.

Data from the International Monitor for Auroral Geomagnetic Effects (IMAGE) magnetometer network showed similar temporal structure extending over a range of latitudes. Information about the magnetometer network is given by *Lühr et al.* [1998]. Analysis of data from 1400 to 1700 UT showed the presence of a field line resonance with discrete frequencies at 1.3 mHz, 1.8 mHz, 3.8 mHz, and 4.9 mHz [*Foat et al.*, 1998]. The 4.9 mHz resonance corresponds to a period of 204 seconds, which is similar to the 100-200 second period seen in the X-ray data. The 4.9 mHz field line resonance had peak power at 65.9°

magnetic latitude, very close to the balloon location. Although the field line resonance was also observed by the Super Dual Auroral Radar Network (SuperDARN), these data are not shown because they were less useful than those provided by the magnetometer chain (F. Fenrich, personal communication, 1998).

3.3.2 Riometer Data

The Imaging Riometer for Ionospheric Studies (IRIS), at Kilpisjärvi, Finland, observed ionospheric absorption at the same time as the balloon observed the X-ray bursts. The imaging riometer is made up of an array of 49 beams at 38.2 MHz, which produce 49-pixel ionospheric absorption images [*Browne et al.*, 1995]. A series of one-minute images taken during the REP event is shown in Figure 3.9 (courtesy of S. Marple, Lancaster University, UK). These images show a single absorption region that brightens twice. The region is approximately stationary, with only a slight motion to the southwest.

For typical auroral electron energies, the ionospheric absorption region is at about 90 km altitude, where the imaging riometer views an area 240 km by 240 km. However, for MeV electron precipitation, the ionospheric absorption region is much lower. The exact absorption altitude is not known, since MeV electron precipitation has been so little studied, but it is probably around 60 km altitude (J. Hargreaves, personal communication, 1998). At this altitude, the imaging riometer views an area 160 km by 160 km. From the riometer images, we can thus determine that the precipitation region is about 80 km by 160 km, oriented in an east-west direction. For an X-ray production region also assumed to be at 60 km altitude, the X-ray imager and germanium spectrometer fields of view are less than 50 km in diameter and project approximately to the lower central (south) part of the riometer images shown in Figure 3.9.

Figure 3.10 shows a time series of one-second absorption data from beam 39 of the imaging riometer, which is located at the lower center of the 49-beam array, and projects close to the center of the X-ray imager field of view. Figure 3.10 also shows the X-ray imager count rate data for comparison. From these data, we conclude that the instruments observed the same event, although the individual peaks are less pronounced in the imaging riometer. The peaks may be less pronounced in the riometer data because it takes some

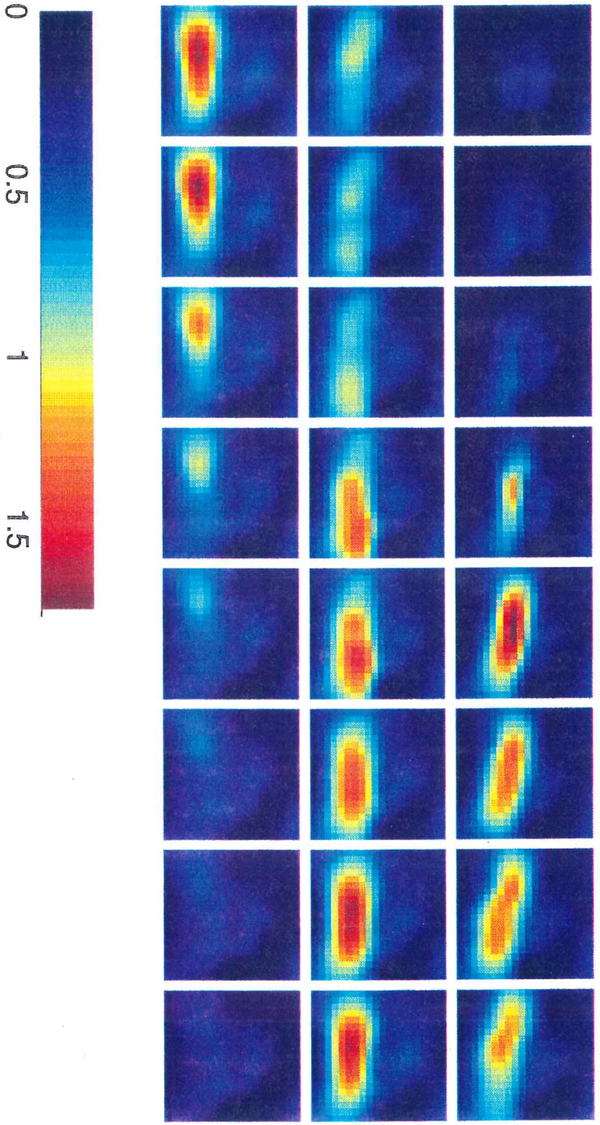

Figure 3.9: One-minute riometer absorption images from 15:32 to 15:55 UT. These images were taken by the Imaging Riometer for Ionospheric Studies (IRIS) at Kilpisjärvi, Finland (geographic latitude 69.05° and longitude 20.79°). Each image is 240 km by 240 km at an altitude of 90 km (or 160 km by 160 km altitude), looking down on the ionosphere. The images were provided by the Communications Research Centre at Lancaster University (UK), funded by the Particle Physics and Astronomy Research Council (PPARC) in collaboration with the Sodankylä Geophysical Observatory.

time for the ionized atmosphere to relax to its normal state after each burst of precipitation. However, this figure may also indicate that there is an underlying time structure to the event whose period is close to 10 minutes. A ten-minute periodicity would agree with the lowest frequency identified in the field line resonance data, as well as the change in spectra observed by the germanium detector after the first ten minutes of the event. Analysis of 10-second images (not shown here) from the imaging riometer supports the conclusion that the REP event was spatially uniform within the field of view of the X-ray imager, and that the 100-200 second periodicity seen in the X-ray data is primarily a temporal effect, not a spatial effect.

3.4 Satellite Data

There were a variety of satellites conveniently positioned to study the various regions of the magnetosphere in coordination with balloon observations of the REP event. Instruments on the Polar satellite was able to view the north pole and image the auroral oval during almost the entire event. The three LANL geosynchronous satellites were spaced around the Earth near the balloon longitude, observing particles in the inner magnetosphere. The two NOAA GOES satellites were not as close to the balloon longitude, but were able to provide equatorial magnetic field measurements not available from the LANL satellites. Although no events were observed while the WIND satellite was passing through its perigee in the magnetotail, at the time of the REP event on August 20, the WIND satellite did observe some activity while it was in the foreshock region. The foreshock region is just outside the Earth's bowshock, where solar wind particles are reflecting off the bowshock. In this region, it is difficult to determine solar wind parameters such as the orientation of the interplanetary magnetic field (IMF).

Other satellites were checked for useful data on the orientation of the IMF at the time of the REP event, including Geotail, which was just inside the bow shock in the magnetopause, and IMP-8, which was just outside the bow shock in the foreshock region. Hence, no good data are available to indicate the orientation of the IMF. Several low altitude polar-orbiting satellites were also checked for precipitating electron measurements at the time

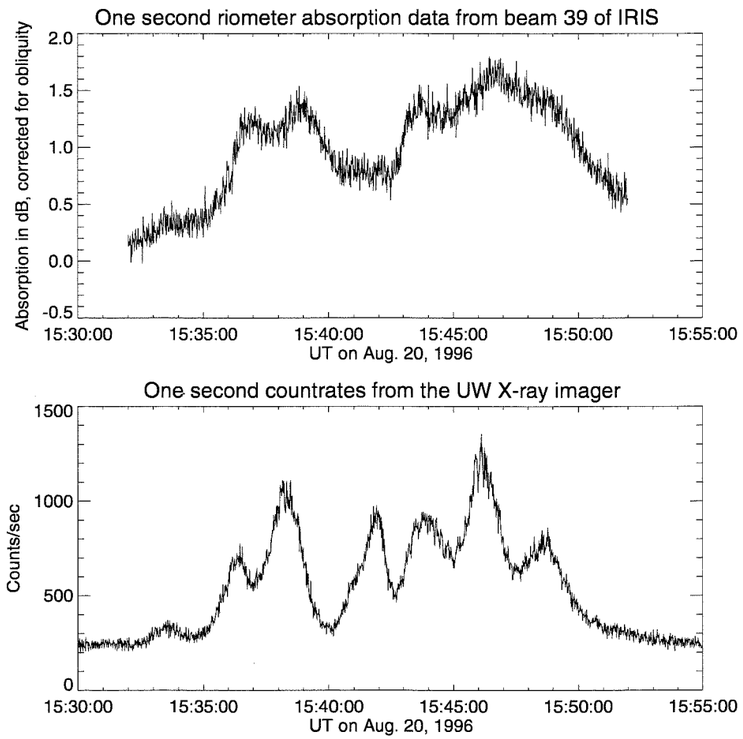

Figure 3.10: One-second riometer absorption data from the Imaging Riometer for Ionospheric Studies (IRIS) at Kilpisjärvi, Finland. These data are from beam 39, which is in the lower (southern) middle of the 49-beam array. At the 60 km projection altitude, this beam is close to the center of the X-ray imager field of view.

of the REP event, including SAMPEX, which was unfortunately in 'safe mode' (X. Li, personal communication, 1997), and DMSP F13, which was in the southern hemisphere (from the NOAA Space Physics Interactive Data Resources (SPIDR) web site).

3.4.1 Global Auroral Images from the Polar Satellite

The Polar satellite carries several different types of cameras designed to study the Earth's auroral oval. These cameras can image the aurora in the visible, ultra-violet and X-ray bands. Because the REP event occurred while the balloon was on the sunlit side of the earth, the Ultra-Violet Imager (UVI) [*Torr et al.*, 1995] and the Polar Ionospheric X-ray Imaging Experiment (PIXIE) [*Imhof et al.*, 1995] provided the most relevant images.

Polar Ultra-Violet Imager

Figure 3.11 shows four 36-second images from the Polar UVI camera, taken in the Lyman-Birge Hopfield Long (LBHL) band (courtesy of M. Brittnacher, University of Washington). Emissions in the LBHL band occur between 160 and 180 nm, and are produced by electron impact on ionospheric nitrogen molecules. The images are plotted in magnetic coordinates (APEX), and show variable auroral structure on both the dayside and nightside during this event. The auroral oval always appears well north of the balloon location, which is indicated in each image by a cross near 1800 MLT. The most intense activity appears near 2200 MLT in the 1516 UT image, before the start of the REP event at 1532 UT. Examination of a full sequence of UVI images (not shown) indicates that this intensification is the beginning of the expansion phase of a small magnetospheric substorm. After 1530 UT, the auroral oval is fairly quiet, indicating the recovery phase of the substorm. The UVI intensification at 1516 corresponds with a small substorm injection that was also seen in particle data from the LANL geosynchronous satellites, to be discussed later in this chapter. The footprint of the LANL satellite closest to the injection region is shown in each image by a cross near 2200 MLT.

Although Figure 3.11 shows only four images from the Polar UVI instrument, 36-second images were available continuously for the entire period 1500-1600 UT. Since

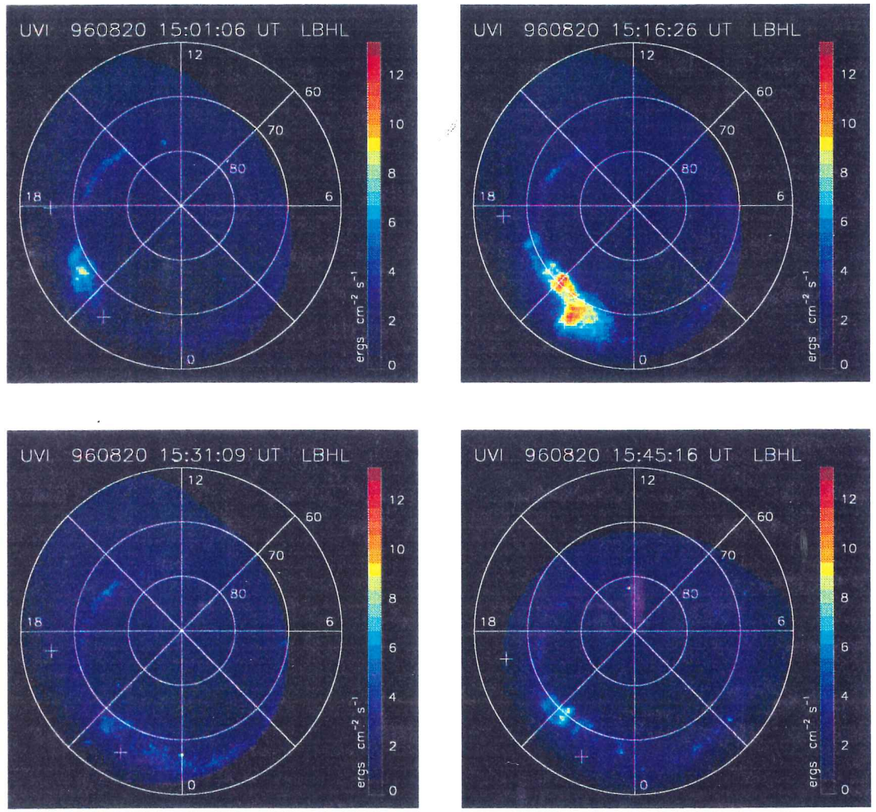

Figure 3.11: Four 37-second images taken at approximately 15-minute intervals by the Polar UVI camera before and during the REP event, courtesy of M. Brittnacher, University of Washington. Note that the auroral oval is always north of the balloon location, which is indicated by a cross near 1800 MLT. The onset of a small substorm is visible in the 15:16:26 image. The footprint of the LANL geosynchronous satellite closest to the substorm injection region is indicated by a cross near 2200 MLT.

it is difficult to look at so many images at once, Figure 3.12 displays this data in a time series format. The figure shows energy input to the atmosphere measured by the UVI for 15-minute pie slices of the images in the pre-midnight sector. Between about 19.00 and 21.00 MLT, Figure 3.12 shows that the energy input started around 14:56 UT, and then increased and decreased a few times, corresponding to the brightening seen around 70 degrees magnetic latitude in the two upper panels of Figure 3.11. At 15:12 UT, Figure 3.12 shows the energy input turning on sharply in the region between between 21.50 and 22.75 MLT, corresponding to the brightening near 65° magnetic latitude in the upper right panel of Figure 3.11. Since the activity before 15:12 UT lasts only a few minutes at a time, and is not accompanied by any significant expansion of the auroral oval, it is probably a pseudo-breakup event. The activity at 15:12 is most likely the actual substorm onset, since it lasts longer, and is accompanied by an expansion in the auroral oval.

Polar Ionospheric X-ray Imaging Experiment

Figure 3.13 shows a sequence of three images from the Polar PIXIE camera (courtesy of J. Stadsnes, University of Bergen, Norway). PIXIE can image X-rays with energies between 2 and 60 keV, but the only significant counts during the 1500-1600 UT time period came from the 2-8 keV range. The most significant activity occurred on the nightside, about half an hour before the REP event. The region of maximum X-ray production appears at approximately the same location as the region of maximum emissions in the UVI image, although extending further east. No X-rays were observed by PIXIE over Scandinavia, perhaps not surprisingly, since the size of the REP event was quite small compared to the field of view of PIXIE.

3.4.2 *Geosynchronous Satellites and Substorm Injections*

Figure 3.14 shows the how the balloon position relates to the activity observed by the Polar UVI camera during the REP event. This figure also shows how the positions of several geosynchronous satellites map to the north pole in magnetic coordinates. The footprints of the three LANL geosynchronous satellites are closest to the precipitation region. None of

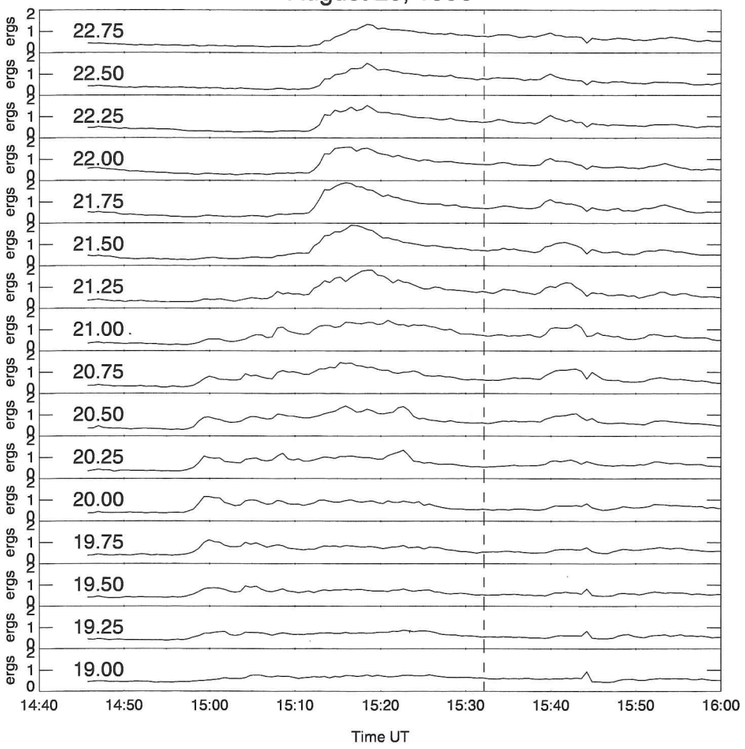

Figure 3.12: Energy input to the atmosphere measured in 15-minute pie slices in MLT by the UVI instrument. The vertical dashed line shows the start of the REP event at 1532 UT. The peak at 1544 UT corresponds to a camera platform shift and is not real.

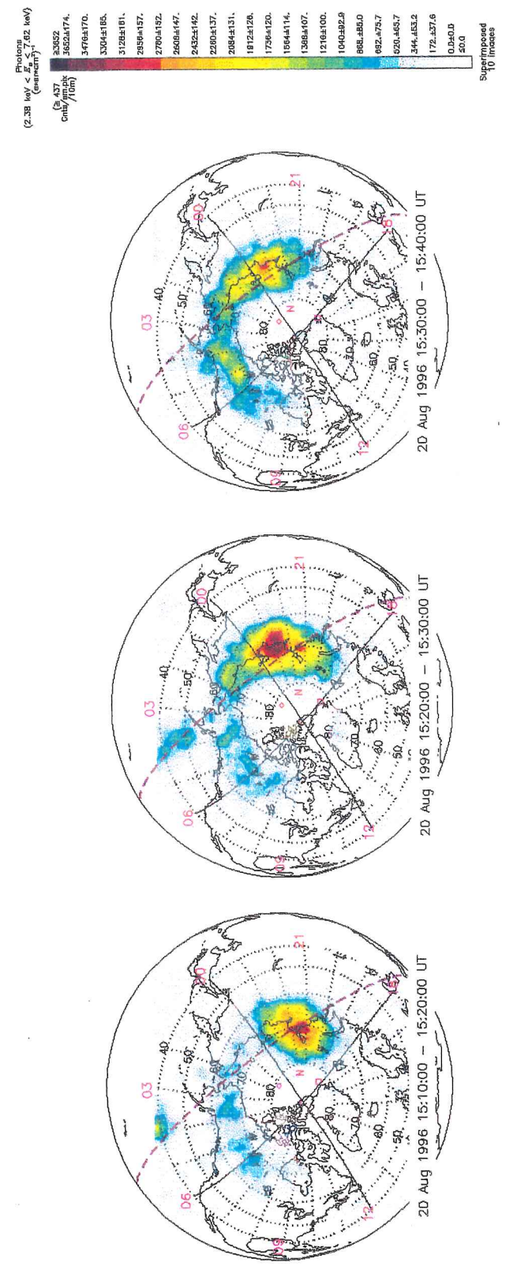

Figure 3.13: Sequence of ten-minute images from PIXIE taken before and during the REP event, courtesy of J. Stadnes, University of Bergen, Norway. The energy range is 2.38-7.62 keV. The sub-satellite point is marked with a red diamond and the center of the field of view is marked with a red square. The solid and dotted lines show magnetic latitude and magnetic local time (CGM), and the dashed line shows the terminator.

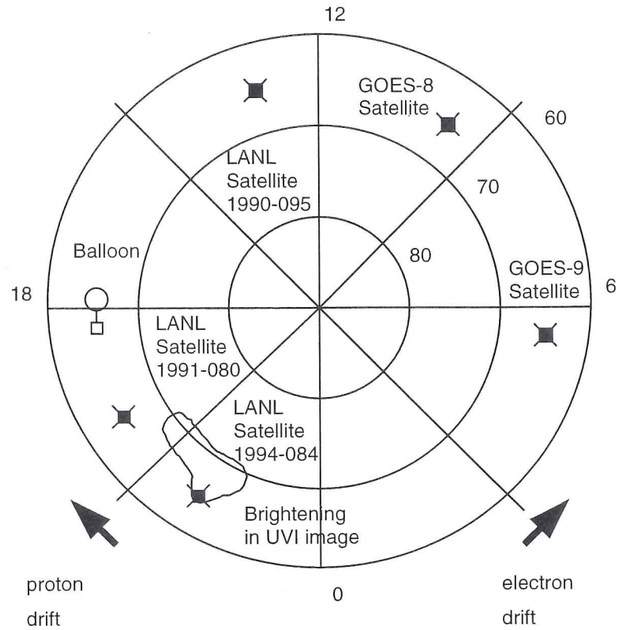

Figure 3.14: Positions of geosynchronous satellite footprints in relation to the balloon position and observed UVI activity at 1515 UT.

the satellites were located on a field line that directly mapped to the position of the balloon. However, it is possible to approximately determine the particle population at any location on the equator during the REP event, using satellite data and well-known gradient-curvature drift formulas.

Figures 3.15 and 3.16 show electron and proton data from the Synchronous Orbit Particle Analyzer (SOPA) and the Energetic Spectrometer for Particles (ESP) on the LANL geosynchronous satellites (courtesy of G. D. Reeves). Information about the SOPA instrument is given by *Belian et al.* [1992] and information about the ESP instrument is given by *Meier et al.* [1996]. Electron and proton data from satellite 1994-084 show a clear evidence of a substorm injection at 1512 UT in the lower energy channels. After injection, these particles drift around the Earth due to the gradient and curvature in the Earth's magnetic field,

with a drift velocity that depends on the energy of the particles. Electrons drift from west to east, and protons drift in the opposite direction. Electron data from all three satellites clearly show the energy dispersion that arises because higher energy particles drift faster. In data from satellite 1994-084, note that the electrons drift all the way around the earth and back to the satellite, while injected protons apparently do not return to the injection region. Note also that the lowest energy proton channels from satellite 1994-084 show several peaks on time scales comparable to those seen in the X-ray data.

Figure 3.15 also shows that although electrons with energies up to hundreds of keV were injected near the time of the REP event, there does not appear to be any increase in MeV electrons. Comparing MeV electron flux measured at the equator to MeV electron flux inferred from the balloon X-ray observations, we find that the ambient equatorial flux is more than enough to account for the precipitation. LANL satellite 1991-080 was the closest to the duskside at the time of the REP event, and it observed a flux of 2.8 $\times 10^5$ cm^{-2} s^{-1} between 0.7 and 1.8 MeV and a flux of 1.0 $\times 10^4$ cm^{-2} s^{-1} between 1.8 and 3.5 MeV. Although the LANL flux values have approximately a factor of 2 uncertainty [*Reeves*, 1998], they are still well above the precipitating electron flux of about 3×10^2 cm^{-2} s^{-1} determined from the germanium detector X-ray measurements. In order to accurately compare these fluxes, it is necessary to take into account the angular distribution of the equatorial electrons, and the change in flux tube area between the equator and the precipitation region. However, the simple comparison presented here indicates that it is not unreasonable to assume the precipitating electrons have their source in the ambient electron population measured at the equator.

In order to further investigate the ambient equatorial population of MeV electrons, data from the ESP instrument are shown in Figure 3.17 for the entire month of August. There is an obvious diurnal variation in counts, and even more variation in these count rates on multi-day time scales. When the REP event was observed on August 20 (day 233), the flux was approximately two orders of magnitude above what it had been six days earlier, in all channels.

Figure 3.18 shows data from the Magnetospheric Plasma Analyzer (MPA) on the LANL satellites (from the NASA Coordinated Data Analysis (CDA) web site, courtesy of D. Mc-

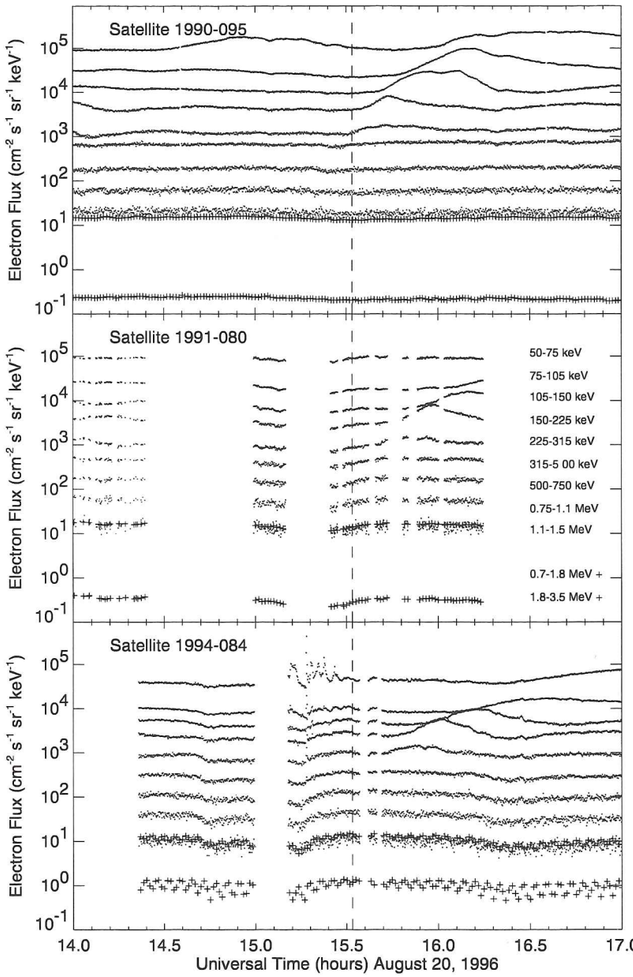

Figure 3.15: Electron data from the LANL geosynchronous satellites, courtesy of G. D. Reeves. Data from the SOPA instrument are shown by dots, and data from the ESP instrument are shown by crosses. A small substorm injection can be seen in the lower energy (50-315 keV) channels of all three satellites as the electrons drift around the earth and disperse in energy. The start of the REP event at 1532 UT is indicated with a dashed vertical line.

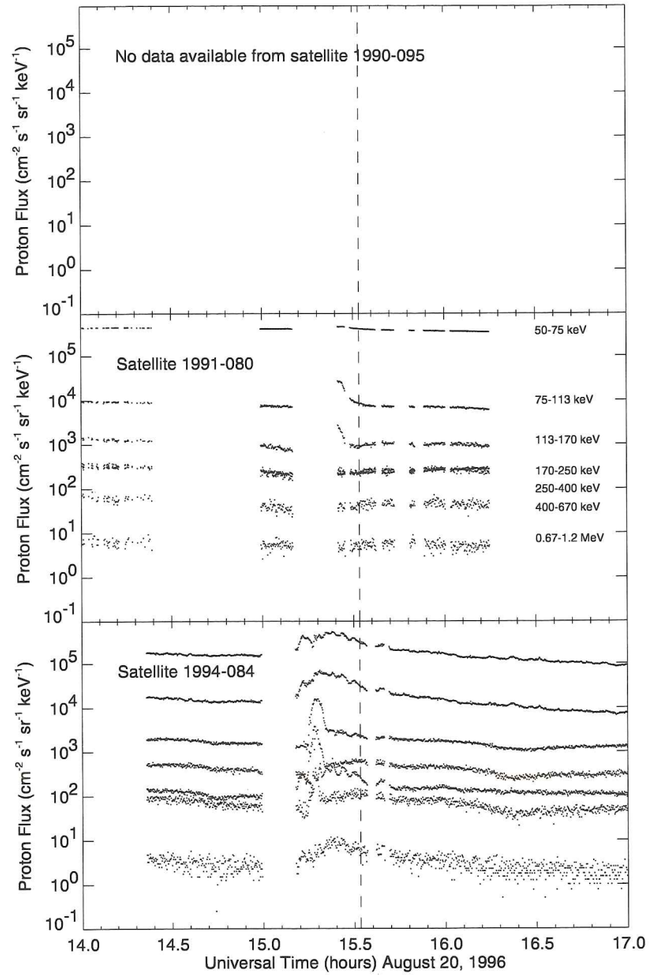

Figure 3.16: Proton data from the LANL geosynchronous satellites, courtesy of G. D. Reeves. All data are from the SOPA instrument. The substorm injection is most clearly visible in the lower energy (50-400 keV) channels of satellite 1994-084 starting at about 1512 UT. The satellite was close to the injection region, since very little energy dispersion can be seen these data. The 400-670 keV channel is contaminated with electrons. The start of the REP event at 1532 UT is indicated with a dashed vertical line.

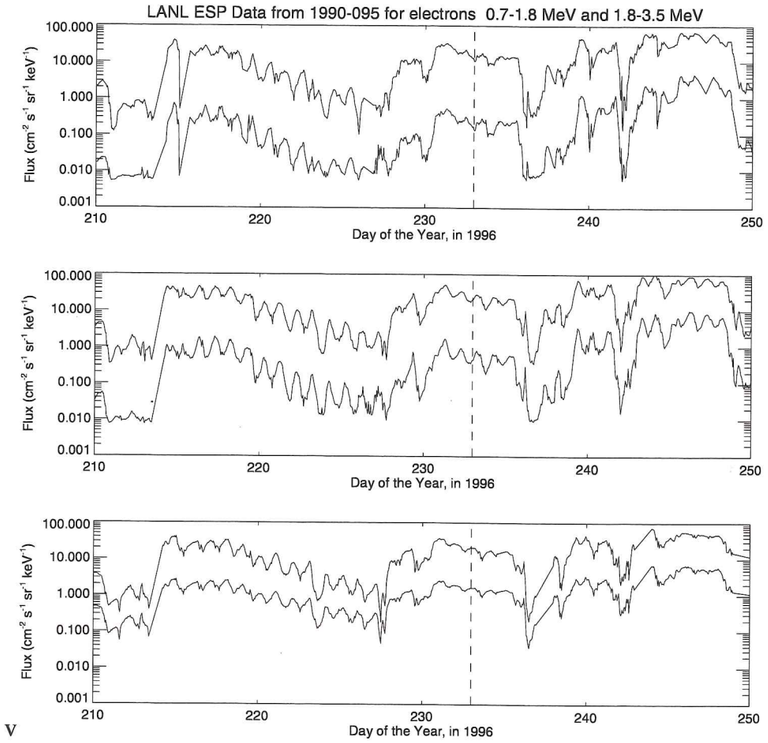

Figure 3.17: High energy electron data from the ESP instrument on the LANL geosynchronous satellites, courtesy of G. D. Reeves. The plot shows the entire month of August. Day 233 corresponds to August 20 and is indicated with a vertical dashed line.

Comas). Information about the instrument is given by *Bame et al.* [1993]. The data shown are for the low energy ions (1-130 eV), for a period of 24 hours. Relevant positions in MLT are shown with vertical lines. The regions of higher density occur when the spacecraft passes inside the plasmasphere or a detached plasma region. It is not possible to tell the difference between the plasmasphere and a detached plasma region with a single-point measurement. The plasmasphere typically has a bulge located on the duskside, but the exact position of the plasmapause can vary a great deal with magnetic activity. The data from satellite 1990-095 (upper panel of Figure 3.18) show the plasmapause bulge centered around 1830 MLT, while the other two satellites show the plasmapause bulge centered closer to MLT noon. The satellite that was closest to the local time of the REP event, 1991-080, unfortunately had a data dropout at 1830 MLT. Satellite 1994-084 shows a small peak near 1830 MLT, possibly indicating a detached plasma region. However, this satellite passed through the region well before the substorm and the REP event. Satellite 1990-095 passed through 1830 MLT a few hours after the substorm and the REP event, and observed densities around 40 cm^{-3}.

Because there was no magnetometer on the LANL satellites, magnetic field data from GOES-9 are shown in Figure 3.19. This figure shows three components of the magnetic field. H_p is the northward component, H_e is the earthward component and H_n is normal to the other two components The small daily variations in H_n and H_e occur since the spacecraft is located at the geographic equator, not the magnetic equator, and the magnetic field is perfectly northward only on the magnetic equator. The daily variations in H_p, the northward component, occur because the magnetic field is not a perfect dipole, but is stretched on the nightside, and compressed on the dayside. The equation for a magnetic dipole gives a magnetic field strength of 110 nT at $L = 6.6$, but these data show that the northward component of the magnetic field actually varied between 70 and 125 nT.

3.4.3 Other Satellites and Magnetospheric Conditions

Figure 3.20 shows data from the WIND Magnetic Field Investigation from the during the time of the REP event. (from the NASA CDA web site, courtesy of R. P. Lepping, Goddard Space Flight Center). *Lepping et al.* [1995] give details about the instrument. Figure 3.21

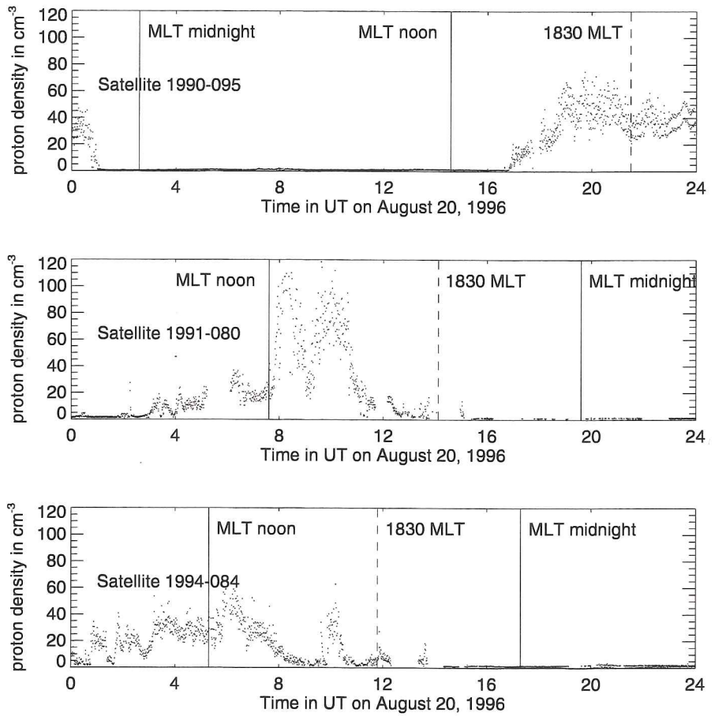

Figure 3.18: Low energy (1-130 eV) proton densities from the MPA instrument on the LANL geosynchronous satellites, from the NASA CDA web site, courtesy of D. McComas.

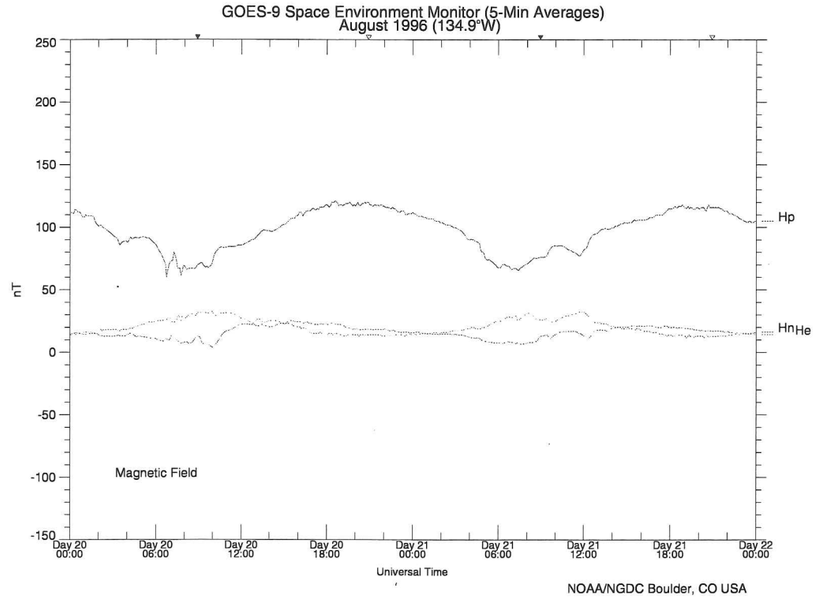

Figure 3.19: August 20-21 magnetometer data from the GOES-9 geosynchronous satellite from the NOAA SPIDR web site. H_p is the magnetic field parallel to the satellite spin axis, or northward, H_e is the earthward component, and H_n is normal to H_p and H_e, or eastward. The filled triangle indicates local midnight, and the unfilled triangle indicates local noon.

shows data from the WIND 3D Plasma Analyzer during the time of the REP event. (from the NASA CDA web site, courtesy of R. P. Lin, University of California at Berkeley). *Lin et al.* [1995] give details about the instrument. At the time of the REP event, the spacecraft had just completed a perigee pass in the Earth's tail, and was traveling back towards the sun. The spacecraft was in the foreshock region, so it is difficult to accurately determine the orientation of the IMF from these data. It is noteworthy, however, that between 1500 and 1530 UT both magnetic field and particle data show pulses of approximately the same periodicity as the bursts observed in the X-ray data and the geosynchronous particle data. Magnetic field data from Geotail, which was also in the foreshock region, exhibit similar time structure, although these data are not shown. This solar wind behavior may have triggered the substorm and X-ray precipitation observed.

3.5 Summary of Data

The data presented in this chapter describe an unusual event. The balloon data show an intense X-ray event that is best explained by electron precipitation with a 1.7 MeV monoenergetic spectrum. The X-ray data also exhibit a complex temporal structure, with periodicities of 10-20 and 100-200 seconds. Observations from the balloon-borne X-ray imager and the ground-based imaging riometer demonstrate that the precipitation event was localized, with very little small scale spatial structure. Electric and magnetic field measurements indicate the presence of magnetic field line resonance, with periodicity similar to, although not correlated with, the X-ray observations. Satellite data show the presence of a magnetospheric substorm beginning about 24 minutes before the REP event.

In the next two chapters, these data are examined in more detail. Mechanisms to account for the relativistic electron precipitation are discussed. The question of whether or not there is a relationship between the REP event, the field line resonance, and the substorm is also addressed.

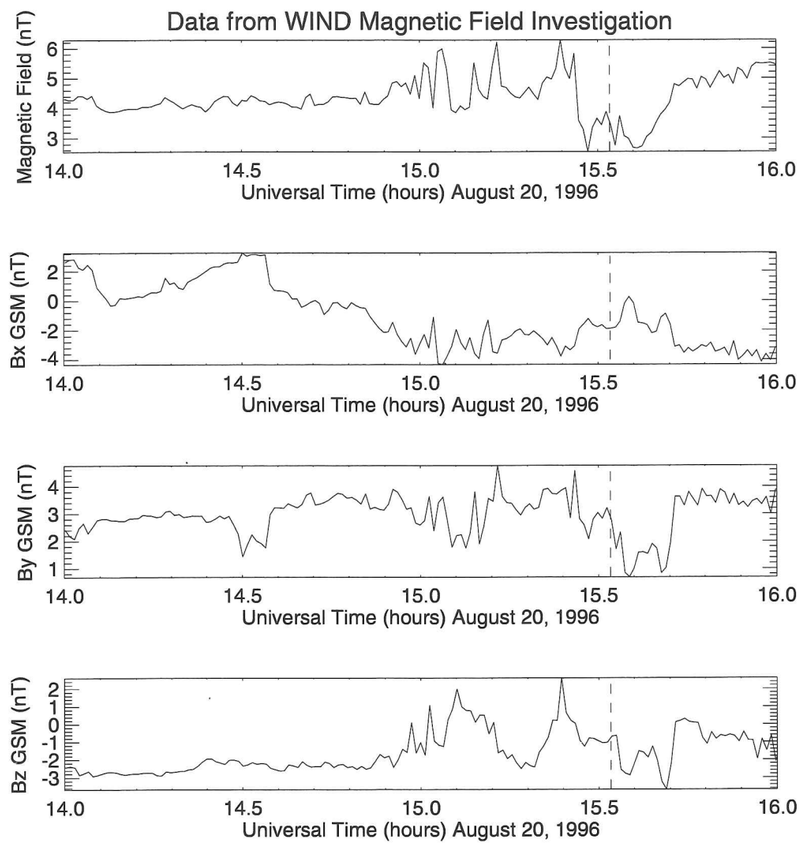

Figure 3.20: Magnetic field data from the WIND spacecraft, from the CDA web site, courtesy of R. Lepping, Goddard Space Flight Center. The start of the REP event at 1532 UT is indicated with a dashed vertical line.

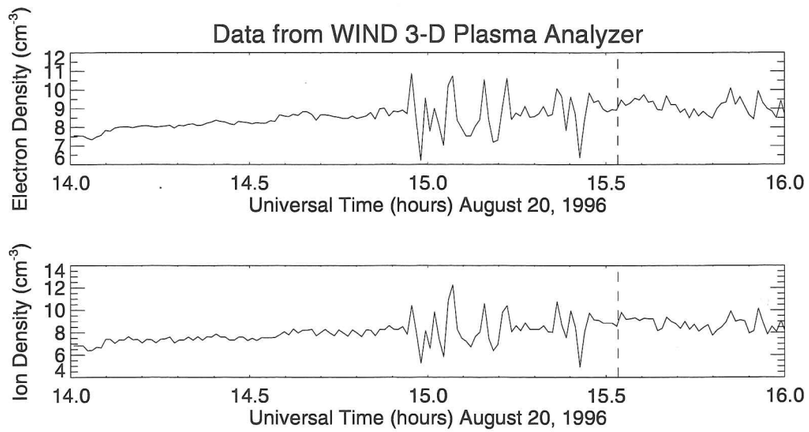

Figure 3.21: Particle data from the WIND spacecraft, from the CDA web site, courtesy of R. P. Lin, University of California at Berkeley. The start of the REP event at 1532 UT is indicated with a dashed vertical line.

Chapter 4

INTERPRETATION OF DATA IN A MAGNETOSPHERIC CONTEXT

In the previous chapter, we presented data describing the relativistic electron precipitation event of August 20, 1996 and related magnetospheric conditions. In this chapter we try to answer the question "What caused the relativistic electrons to precipitate?" We are also interested in understanding the spatial localization, the temporal structure, and the mono-energetic spectral shape of the event. We do not, however, address the question of how the electrons obtained MeV energies. Satellite data show that on the day of the observed REP event, significant fluxes of MeV electrons are present at the equator near field lines mapping to the balloon location. We simply investigate how these particles are lost through precipitation and how the particle loss is related to the magnetospheric conditions.

In the steady-state case, a particle will bounce along magnetic field lines as it gradient-curvature drifts around the Earth. However, the particle may enter the loss cone and precipitate into the atmosphere, if some mechanism decreases the particle's pitch-angle. The pitch-angle is given by $\alpha = \tan^{-1}(v_\perp/v_\parallel)$, where $v_\perp$ is the particle's velocity perpendicular to the magnetic field and $v_\parallel$ is the particle's velocity parallel to the magnetic field. A number of mechanisms can change the pitch-angle of trapped particles and cause precipitation, including field-aligned potential drops, plasma-sheet scattering, and wave-particle interactions. In the first three sections of this chapter, we evaluate the suitability of each of these mechanisms for the REP event observed on August 20, 1996. A suitable mechanism must be able to produce mono-energetic electron precipitation at 1.7 MeV and operate in a spatially localized region on the duskside. In the last two sections of this chapter, we examine the coincident observations of a field line resonance and a magnetospheric substorm, and discuss whether or not these events are related to the duskside REP event.

4.1 Field-Aligned Potential Drops

One mechanism commonly used to explain mono-energetic peaks in auroral energy spectra is that of the field-aligned potential drop [*Lyons and Williams*, 1984]. Electric fields parallel to the magnetic field can accelerate particles in the parallel direction. This mechanism will work on particles of all energies, having the effect of shifting an entire distribution to higher energies and creating a peak. Peaks observed in precipitating electron spectra are typically between 1 and 10 keV, and are associated with inverted-V events and discrete auroral arcs [*Swift*, 1981]. Satellite observations of d.c. electric fields up to 400 mV m^{-1} imply total potential drops of several kV at altitudes below 8000 km associated with inverted-V events [*Mozer et al.*, 1977]. No theoretical or observational evidence exists to link this mechanism with potential in the MV range or precipitating electrons in the MeV range.

During inverted-V auroral events, the 1-10 keV mono-energetic features typically occur along with a sizable low energy spectrum, which is believed to be the result of backscattered upgoing electrons that cannot get through the field-aligned potential [*Evans*, 1974]. For the observed REP event, no enhanced low energy component was present, giving further evidence that the field-aligned potential drop was not the mechanism responsible for this event.

4.2 Plasma Sheet Scattering

A mechanism that has been invoked to explain mono-energetic peaks at larger electron energies is plasma sheet scattering. If the radius of curvature of the magnetic field is small enough that the field varies significantly over distances less than one gyroradius, then the first adiabatic invariant will not be conserved. The first adiabatic invariant for relativistic electrons is given by

$$\mu = \frac{\gamma m_e c^2}{2B} \tag{4.1}$$

where $\gamma = (1 - v^2/c^2)^{-1/2}$, v is the electron velocity, c is the speed of light, m_e is the electron mass, and B is the magnetic field strength. In the non-adiabatic case, pitch-angle scattering can occur, and particles can be precipitated. *Speiser* [1965] has computed particle

trajectories for a simple analytic model plasma sheet, and found that particles encountering this plasma sheet are ejected with smaller pitch-angles.

Using the empirical magnetospheric magnetic field model of *Tsyganenko and Usmanov* [1982], more recent work has been done by *Sergeev and Tsyganenko* [1982] and *Sergeev et al.* [1983]. They found that pitch-angle scattering increases when the radius of field line curvature, R_c, is less than ten times the gyroradius, r_c. This mechanism has been used to account for MeV peaks in electron spectra observed by the low-altitude satellite UARS [*Imhof et al.*, 1997].

The relativistic electron gyroradius is given by

$$r_c = \gamma v_\perp / \Omega_e \tag{4.2}$$

where Ω_e is the unsigned electron cyclotron frequency given by $|q_e|B/m_e c$, with q_e the charge on an electron. For a given B, electrons with higher velocities will have larger gyroradii, and will be more likely to satisfy the Sergeev condition, $R_c < 10 r_c$. Therefore this mechanism can produce peaks at relativistic energies in precipitating electron spectra. For an electron of energy 1 MeV and gyrofrequency of 4 kHz (such as would be found at the equator of a dipole field line at $L = 6$), the gyroradius is 33 km. The radius of curvature is 13000 km. In this case, the Sergeev condition would not be satisfied, but if the magnetic field were stretched, such as in the nightside tail region, then its radius of curvature would be smaller, and the Sergeev condition could be satisfied. However, since the balloon observations were made on the duskside, where the stretching of the tail does not have much effect, we do not believe that the plasma sheet scattering mechanism can reasonably account for the observed REP event.

4.3 Wave-Particle Interactions

Another mechanism that has been used to explain electron precipitation for a variety of energy ranges and spectral shapes is wave-particle interactions. To examine the effects of electromagnetic waves on charged particles in a magnetic field, it is useful to consider a guiding center frame of reference. The guiding center of a particle in a homogenous magnetic field is the center of the gyration [*Parks*, 1991]. In an inhomogenous, dipole magnetic

field, the guiding center follows the center of gyration as the particle experiences bounce and drift motion. Therefore, we can transform into a guiding center frame of reference in order to focus on the gyration of the particle. In the transformation, we neglect the guiding center drift velocity, since it is much smaller than the bounce velocity, and we are interested in effects that occur on time scales smaller than the drift time scale. Thus, the transformation is into a reference frame in which the particle has no velocity component parallel to the magnetic field [*Walker*, 1993]. In the guiding center frame of reference, the particle just gyrates around the field line, simplifying analysis of the effects of the wave electric field on the particle. Since the transformation into this frame of reference is parallel to the magnetic field, there is no electric field introduced.

The direction of the electron gyration around the ambient magnetic field, $\vec{B_0}$, is determined by the magnetic part of the Lorentz force, $q_e(\vec{v} \times \vec{B_0})$. If the thumb of the right hand is aligned along the magnetic field then the fingers will give the direction of the electron motion.

If an electron sees a circularly polarized electromagnetic wave whose electric field is in the same direction as the electron velocity at all times, then the electron will be decelerated by the electric part of the Lorentz force, $\vec{F} = q_e\vec{E}$. If the wave electric field is exactly 180° out of phase with the direction of the electron velocity then the electron will instead be accelerated. If the Doppler-shifted wave frequency is not an integer multiple of the electron gyrofrequency, then the effects of the electric field will cancel out when averaged over a cycle, and there will be no net acceleration or deceleration.

When the Doppler-shifted wave frequency equals an integer multiple of the gyrofrequency in the particle guiding center frame of reference, the electron and wave are said to be in resonance. This resonance can lead to a change in pitch-angle and thus to precipitation of the particle. The process is referred to as pitch-angle diffusion, because the direction of change in the pitch-angle is random, depending on the relative phases of both wave and particle.

In order to determine which type of wave can resonate with electrons, we need to consider the wave polarization. Right-hand circularly polarized waves have an electric field that rotates in the direction of the fingers of the right hand when the thumb is placed

along the direction of the ambient magnetic field. Electrons can resonate with waves that are right-hand polarized in their guiding center frame of reference. Left-hand circularly polarized waves have an electric field that rotates in the direction of the fingers of the left hand when the thumb is placed along the direction of the magnetic field. Electrons cannot resonate with waves that are left-hand polarized in their guiding center frame of reference.

Note that the plasma definition of wave polarization differs from the radio and optical definitions, which define the polarization with respect to the direction of the wave vector, $\vec{k}$, and not the direction of the ambient magnetic field, $\vec{B_0}$. For waves in a plasma, however, the definition with respect to the magnetic field makes more physical sense, since ions and electrons gyrate around the field line in the same direction independent of the direction of their velocity along the magnetic field. In the plasma frame of reference, whistler mode waves are right-hand polarized, and ion cyclotron mode waves are left-hand polarized. However, the polarization is not necessarily the same in the plasma and guiding center frames of reference.

The top panel of Figure 4.1 shows an example of a resonance where the polarization is the same in both plasma and guiding center frames of reference, and the bottom panel shows an example of an anomalous resonance where the polarization is different in the plasma and guiding center frames of reference. For simplicity, Figure 4.1 illustrates the non-relativistic case, but the additional factor of γ for the relativistic case does not affect the basic principles shown here. In this figure, the electron parallel velocity, $v_\parallel$, and wave phase velocity, $v_p = (\omega/k)$, in the plasma frame are compared with the the electron parallel velocity, $v'_\parallel$, and wave phase velocity, $v'_p = (\omega'/k')$, in the electron guiding center frame.

The top panel of Figure 4.1 illustrates $\vec{v_p}$ and $\vec{v_\parallel}$ pointing in opposite directions in the plasma frame. In the electron guiding center frame, the wave phase velocity will appear to be in the same direction, but larger than in the plasma frame. The figure also shows the electric field vectors at four different times for a wave that is right-hand circularly polarized in the plasma frame (*i.e.* a whistler mode wave). It is helpful to consider four different times, t_{1-4}, as the wave propagates to the right in the electron guiding center frame, for a Doppler-shifted wave frequency matching the electron gyrofrequency. At all four times the electron perpendicular velocity and the wave electric field are in the same direction.

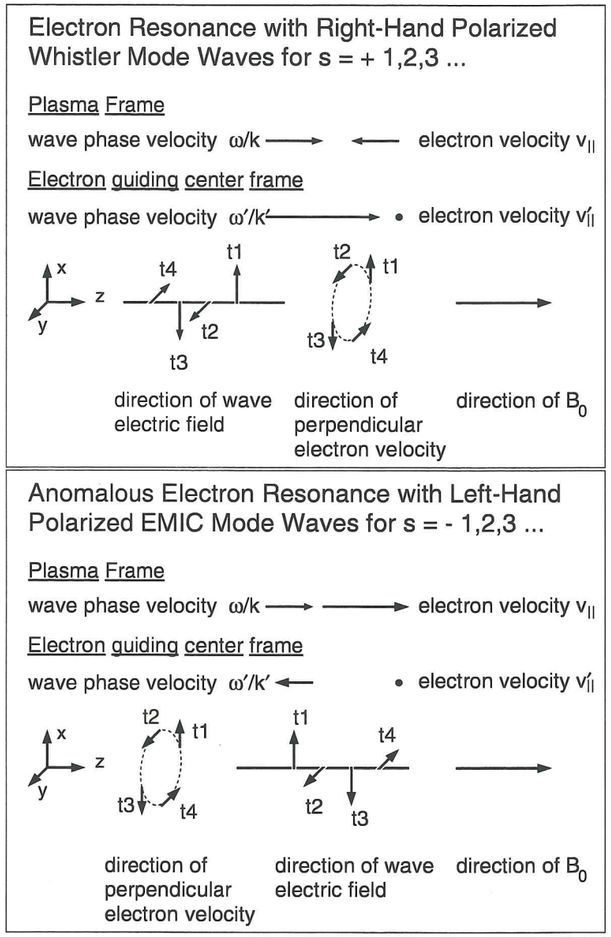

Figure 4.1: Electron resonance for regular and anomalous Doppler shifts. The top panel shows how an electron can resonate with a right-hand polarized whistler mode wave. The bottom panel shows how an electron can resonate with a left-hand polarized EMIC mode wave.

Therefore resonance can occur and the electron can be accelerated. In this example the wave appears to be right-hand polarized in both the plasma frame and the electron guiding center frame. Examination of the vectors drawn for v_p and $v_\parallel$ shows that this case will result in the same polarization for any magnitudes of v_p and $v_\parallel$, as long as they point in opposite directions.

The bottom panel of Figure 4.1 illustrates $\vec{v_p}$ and $\vec{v_\parallel}$ pointing in the same direction in the plasma frame, with $v_\parallel > v_p$. In the electron guiding center frame, the wave phase velocity will appear to be in the opposite direction as in the plasma frame. This figure shows the electric field vectors at four different times for a wave that is left-hand circularly polarized in the plasma frame (*i.e.* an ion cyclotron mode wave). Again consider four different times t_{1-4}, as the wave propagates to the left in the electron guiding center frame, for a Doppler-shifted wave frequency matching the electron gyrofrequency. At all four times, the electron perpendicular velocity and the wave electric field are in the same direction, so resonance can occur. In this example, the wave appears to be left-hand polarized in the plasma frame, and right-hand polarized in the electron frame. This change in polarization is known as the anomalous Doppler shift. Examination of the vectors drawn for v_p and $v_\parallel$ shows that this case will result in the anomalous Doppler shift only for $v_p < v_\parallel$.

In order to determine the frequency that the electron sees in the guiding center reference frame, we need to consider the relativistic Doppler shift,

$$\frac{\omega'}{\gamma} = \omega\left(1 - \frac{v_\parallel}{v_p}\right) = (\omega - v_\parallel k_\parallel) \tag{4.3}$$

where ω is the frequency in the plasma frame and ω' is the frequency in the electron guiding center frame. Both $k_\parallel$ and $v_\parallel$ are signed quantities. The factor of γ accounts for time dilation when velocities approach the speed of light.

The Doppler-shifted frequency given by Equation 4.3 will be greater or less than the frequency in the plasma frame, depending on the sign and magnitude of v_p, $v_\parallel$, and γ. Because whistler and ion cyclotron mode waves both have frequencies less than the electron cyclotron frequency in the plasma frame, a Doppler shift that results in $\omega' > \omega$ is necessary for electron cyclotron resonance.

Using the relativistic Doppler shift given in Equation 4.3, the resonance condition can

be expressed as

$$\omega - k_{\|} v_{\|} = s\Omega_e/\gamma \tag{4.4}$$

where s is an integer accounting for harmonics of the resonance. Positive s gives the regular Doppler shift, illustrated in the top panel of Figure 4.1 and negative s gives the anomalous Doppler shift illustrated in the bottom panel of Figure 4.1. The special case of $s = 0$ corresponds to the Landau or Čerenkov resonance.

For the non-relativistic case where $\gamma \approx 1$, the resonance condition given in Equation 4.4, shows that for $\omega < \Omega_e$ and s positive, $k_{\|}$ and $v_{\|}$ must have the opposite sign, so the wave and electron must travel in opposite directions (top panel in Figure 4.1). These are the conditions needed for resonance of non-relativistic electrons with whistler mode waves. The relativistic case is slightly more complicated, and will be discussed later in this chapter. For $\omega < \Omega_e$ and s negative, $k_{\|}$ and $v_{\|}$ must be of the same sign, and so the wave and electron must travel in the same direction (bottom panel in Figure 4.1). These are the conditions needed for anomalous electron resonance with ion cyclotron mode waves. In this case, the electron velocity must be greater than the wave phase velocity. For typical magnetospheric conditions, only relativistic electron velocities satisfy Equation 4.4 for negative s.

The cyclotron resonant interaction can take place anywhere Equation 4.4 is satisfied. However, for the very high energy electrons, the interaction is most likely near the equator, as will be shown later. Figure 4.2 shows the interaction region and typical vector directions for both types of interaction. In the next two subsections, we examine in detail the whistler and the EMIC mode waves, and calculate the electron energies that these wave modes can interact with.

4.3.1 Whistler Mode Waves

Whistler mode waves are right-hand circularly polarized waves, whose cold-plasma dispersion relation for parallel propagation, assuming $\Omega_i \ll \omega < \Omega_e \ll \omega_{pe}$ [*Kennel and Petschek*, 1966], is given by

$$n^2 = \frac{c^2 k^2}{\omega^2} = \frac{\omega_{pe}^2}{\omega(\Omega_e - \omega)} \tag{4.5}$$

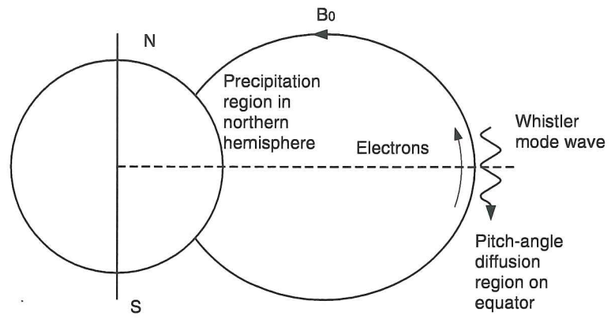

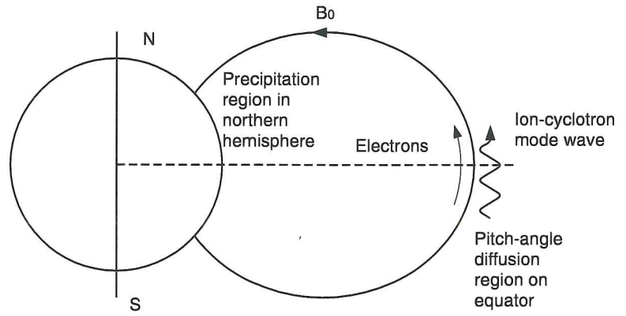

Figure 4.2: Pitch-angle diffusion interaction region and vector directions for electron resonance with whistler and ion cyclotron mode waves.

where n is the index of refraction, k is the wave number, and ω_{pe} is the electron plasma frequency, $\sqrt{4\pi N_e q_e^2/m_e}$, where N_e is the electron number density.

Combining this dispersion relation with the relativistic electron resonance condition from Equation 4.4 for $s = 1$ gives

$$E_{res} = 2E_{mag}\frac{\Omega_e}{\omega(\gamma+1)}\left[1-\gamma\left(\frac{\omega}{\Omega_e}\right)\right]^2\left[1-\left(\frac{\omega}{\Omega_e}\right)\right] \tag{4.6}$$

where E_{res} is the resonant electron kinetic energy in the parallel direction ($v_\perp/c \ll 1$) given by $m_e c^2(\gamma-1)$, and $E_{mag} = B^2/8\pi N_e$ is the magnetic energy. A similar treatment is presented in *Chang and Inan* [1983], solving for a parallel resonant velocity instead of a resonant energy.

This equation has γ on both sides, making it difficult to solve. By assuming that the term $1-\gamma(\omega/\Omega_e)$ was approximately $1-(\omega/\Omega_e)$, *Thorne and Andreoli* [1980] simplified this equation to become

$$E_{res} = \left\{\left[\frac{2E_{mag}}{m_e c^2}\frac{\Omega_e}{\omega}\left(1-\frac{\omega}{\Omega_e}\right)^3+1\right]^{1/2}-1\right\}m_e c^2. \tag{4.7}$$

Since the MeV electrons of interest are relativistic, $\gamma \approx 1$ is not a very good approximation, but it does provide a way to easily see the form of the function. The approximation overestimates the value of E_{res} for higher velocities. Figure 4.3 shows the relation between frequency and resonant electron energy for various densities on the equator at $L = 6$ for this low-gamma approximation. The figure shows that whistler resonance with electrons of 1.7 MeV is most likely to occur for low densities and low frequencies.

The formula for the resonant electron energy given in Equation 4.7 and plotted in Figure 4.3 involves three significant assumptions. The first is $v_\perp/c \ll 1$, the second is $\gamma \approx 1$, and the third is $s = 1$. A more correct treatment accounts for a range of $v_\perp$, s, and γ. This treatment begins with rewriting the resonance condition in Equation 4.4 as

$$\omega - k_\parallel v_\parallel = s\Omega_e\sqrt{1 - v_\parallel^2/c^2 - v_\perp^2/c^2}. \tag{4.8}$$

Although this equation will not give a simple analytical expression for E_{res}, it can be interpreted graphically by rearranging into the familiar form of an ellipse in velocity space [*Melrose*, 1986],

$$\frac{(v_\parallel/c-h)^2}{b^2}+\frac{(v_\perp/c-0)^2}{a^2} = 1. \tag{4.9}$$

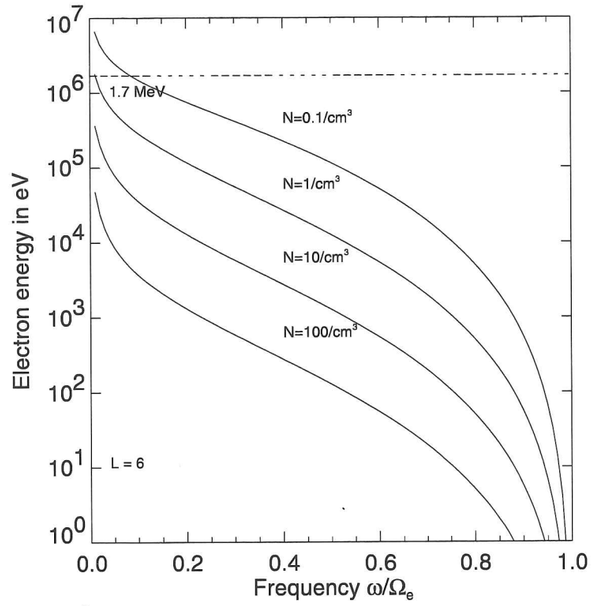

Figure 4.3: Electron parallel resonance energy for various densities and whistler wave frequencies calculated using the low-gamma approximation from Equation 4.7.

Here, h is the center of the ellipse,

$$h = \frac{\omega k_\parallel c}{s^2\Omega_e^2 + k_\parallel^2 c^2}, \tag{4.10}$$

a is the major radius of the ellipse,

$$a = \left(\frac{s^2\Omega_e^2 + k_\parallel^2 c^2 - \omega^2}{s^2\Omega_e^2 + k_\parallel^2 c^2}\right)^{1/2}, \tag{4.11}$$

and b is the minor radius of the ellipse,

$$b = \left(\frac{s^2\Omega_e^2(s^2\Omega_e^2 + k_\parallel^2 c^2 - \omega^2)}{s^2\Omega_e^2 + k_\parallel^2 c^2}\right)^{1/2}. \tag{4.12}$$

The ellipse is easily plotted by choosing values for $|s|$ and ω and determining $k_\parallel$ from the dispersion relation for a particular wave mode. Note that s is always squared in the

expressions for a, b, and h, so ellipses for positive and negative s will look the same. The value for $k_\parallel$ can have a sign, but we choose $k_\parallel$ to be positive, and allow $v_\parallel$ to be either positive or negative, in order to examine the cases of wave and electron traveling in the same and opposite directions.

Figure 4.4 shows a plot of Equation 4.9 for a whistler mode wave of frequency $0.5\Omega_e$ at $L = 6$ for a density of 1 cm^{-3} and harmonic of $s = |1|$. The left side (solid part) of the resonance ellipse gives the normal resonance and the right side (dashed part) gives the anomalous resonance. Since whistler mode waves are right-handed, only the solid part is a physical solution for electrons. Kinetic energy is given by $m_e c^2(\gamma - 1)$, so circles of constant $v_\perp^2 + v_\parallel^2$ define circles of constant kinetic energy. Therefore, the ellipse shows that electrons of various energy can resonate with whistler mode waves in the relativistic case. The diamond on the $v_\parallel$ axis gives the low-gamma approximation for E_{res} from Equation 4.7, which can be considered to be the minimum resonant energy, when the assumption $\gamma \approx 1$ is valid.

The solid outer circle in Figure 4.4 is the light circle, where $v = c$. The resonance ellipse touches the light circle where $v_\parallel = v_p = \omega/k_\parallel$. For whistler mode waves (and also for ion cyclotron waves), the index of refraction is $n = kc/\omega > 1$, so the phase speed is always less than the speed of light. The point where $v_\parallel = v_p$ is the point where the resonance changes from regular to anomalous.

The inner dotted circle in Figure 4.4 shows the velocity of an electron of energy 1.7 MeV. The resonance ellipse crosses the 1.7 MeV circle in the region of positive $v_\parallel$, which corresponds to the case of an the electron and wave traveling in the same direction in the plasma frame. This case is different than that shown previously in the upper panel of Figure 4.1. By determining where the resonance ellipse crosses the 1.7 MeV circle, the pitch-angle of the resonant electrons, can easily be determined from the parallel and perpendicular velocities. For the case shown in Figure 4.4, a 1.7 MeV electron would need a pitch-angle of about 83° to resonate with the wave. Since this pitch-angle is very large, it is unlikely that this electron would be scattered into the loss cone by resonating with a whistler mode wave. In order for the whistler mode to resonate with 1.7 MeV electrons of smaller pitch-angles at $L = 6$, we need either lower densities, lower frequencies, or higher

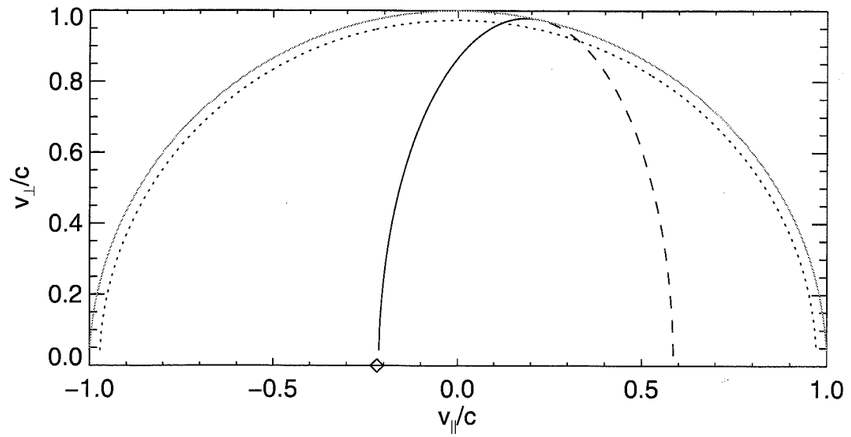

Figure 4.4: The resonance ellipse for whistler mode waves of frequency $0.5\Omega_e$ at $L = 6$ for a density of 1 cm^{-3} and harmonic of $s = |1|$.

harmonics.

Figure 4.5 shows how the shape of the ellipse would change by varying each of these three variables: density, frequency, and harmonic. Figure 4.5a shows that lower densities result in resonance with 1.7 MeV electrons of smaller pitch-angle. However, densities smaller than about 0.1 cm^{-3} are not very reasonable for the duskside region at $L = 6$ [*Chappell et al.*, 1970]. Figure 4.5b shows that lower wave frequencies also result in resonance with 1.7 MeV electrons of smaller pitch-angle. However, whistler waves are usually not observed at low frequencies because the group and phase velocities become zero at low frequencies. Figure 4.5c shows that higher harmonics also result in resonance with 1.7 MeV electrons of smaller pitch-angle. However, it is unlikely that high energy electrons would resonate with a whistler mode wave at $s = 4$, without lower energy electrons simultaneously resonating with the same wave at $s = 1$. Therefore, this mechanism would not account for a mono-energetic 1.7 MeV precipitating electron spectrum.

The conclusion to be drawn from Figure 4.5 is that for 1.7 MeV electrons to resonate with whistler mode waves, an unlikely combination of physical parameters is necessary. Therefore we will examine the electromagnetic ion cyclotron mode instead.

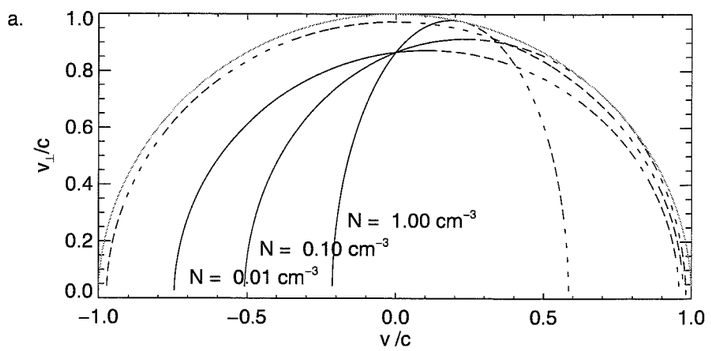

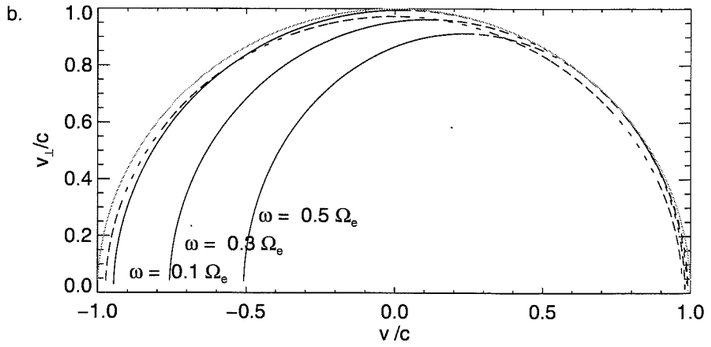

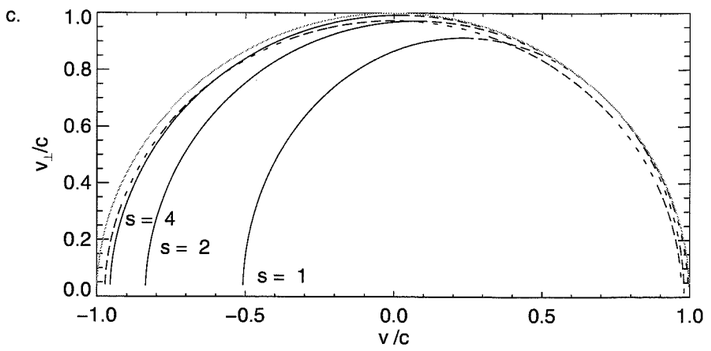

Figure 4.5: Variation in whistler resonance ellipse with a) density for $|s| = 1$ and $\omega = 0.5\Omega_e$, b) frequency for $N = 0.1$ cm^{-3} and $|s| = 1$, and c) harmonic for $N = 0.1$ cm^{-3} and $\omega = 0.5\Omega_e$ The outer solid circle is where $v = c$ and the inner dashed circle is for electrons of energy 1.7 MeV.

4.3.2 *Electromagnetic Ion Cyclotron Mode Waves*

Electromagnetic ion cyclotron waves are left-hand circularly polarized waves whose cold-plasma dispersion relation for parallel propagation, where $\omega < \Omega_i \ll \omega_{pi}$ [*Kennel and Petschek*, 1966], is given by

$$n^2 = \frac{c^2k^2}{\omega^2} = \frac{\omega_{pi}^2}{\Omega_i(\Omega_i - \omega)} \tag{4.13}$$

where ω_{pi} is the unsigned ion plasma frequency, $\sqrt{4\pi N_i q_e^2/m_i}$, where N_i is the ion number density, m_i is the mass of an ion, and Ω_i is the ion cyclotron frequency, $|q_e|B/m_ic$.

Combining the EMIC dispersion relation with the relativistic electron resonance condition given in Equation 4.4, and using $\omega \ll \Omega_e$ (reasonable for all cases, since for the ion cyclotron mode $\omega < \Omega_i = \Omega_e/1836$), we can obtain a formula for E_{res}, the parallel electron kinetic energy that is resonant with the waves [*Thorne and Andreoli*, 1980]. No approximations for γ are used in this derivation.

$$E_{res} = \left\{ \left[\frac{2E_{mag}}{m_ec^2} \left(\frac{m_i}{m_e}\right) \left(\frac{\Omega_i}{\omega}\right)^2 \left(1 - \frac{\omega}{\Omega_i}\right) + 1 \right]^{1/2} - 1 \right\} m_ec^2 \tag{4.14}$$

Figure 4.6 shows the resonance ellipse obtained by using Equation 4.9 with the EMIC dispersion relation in Equation 4.13. Since EMIC mode waves are left-hand polarized, we are interested in the anomalous resonance, which is the solid part of the ellipse on the right side. The dashed part of the ellipse on the left side is not a physical solution for electrons. The diamond shows the minimum resonance energy calculated from Equation 4.14. As in the whistler case, this form for E_{res} assumes that all of the electron velocity is in the parallel direction. In other words, this resonant energy is the minimum possible resonant energy. It is reasonable to look at this value, since the electrons that are most likely to be pitch-angle scattered and precipitated are those that have small pitch-angles, or large parallel velocities.

The minimum energy for electron resonance with EMIC mode waves can be easily calculated from Equation 4.14, given input values for B, N, and ω. Figure 4.7 shows the relation between minimum resonant energy and frequency for various densities on the equator at $L = 6$. From this figure, we see that electron resonant energies in the MeV

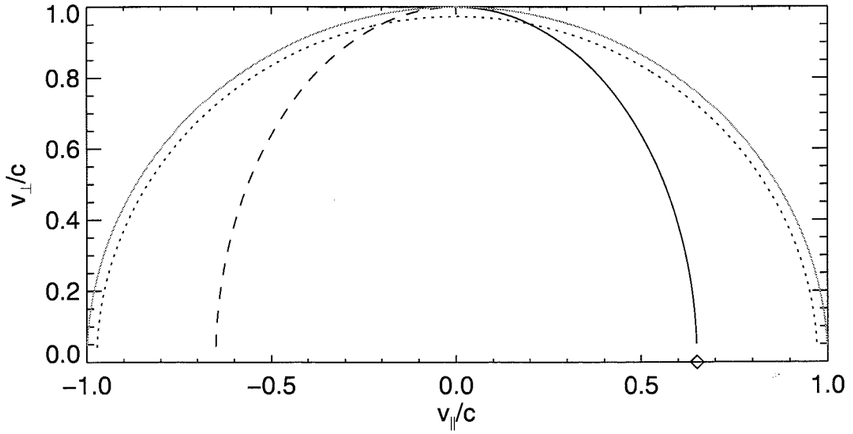

Figure 4.6: The resonance ellipse for EMIC mode waves of frequency $0.5\Omega_i$ at $L = 6$ for a density of 1000 cm^{-3} and harmonic of $s = |1|$.

range are more likely for higher densities. Wave growth closer to the ion gyrofrequency is unlikely due to damping. For reasonable values of plasma density (10-100 cm^{-3}) the curves show that resonant interactions with electrons of energy $<$ MeV are unlikely, as previously suggested by *Davidson* [1978]. The values for minimum resonant energy shown in the figure are calculated for the equator. However, moving off the equator will only result in a larger value for E_{mag} in Equation 4.14. Therefore, the interaction is most likely to occur on the equator, as shown previously in Figure 4.2.

The next question to address is whether or not the high density values determined from Figure 4.7 are reasonable for the equatorial region mapping to the balloon location during the REP event. Typical satellite measurements of equatorial plasma density are shown in Figure 4.8. These measurements were obtained on the nightside, for various levels of magnetic activity. From this figure, we see that densities of 10-1000 cm^{-3} are typically observed near the plasmapause. For $K_p \sim 2$, as observed during the REP event, the nightside plasmapause is located around $L = 4.5$, mapping to a somewhat lower latitude than the balloon location at $L = 5.8$.

However, these satellite measurements were taken on the nightside, and Figure 4.9

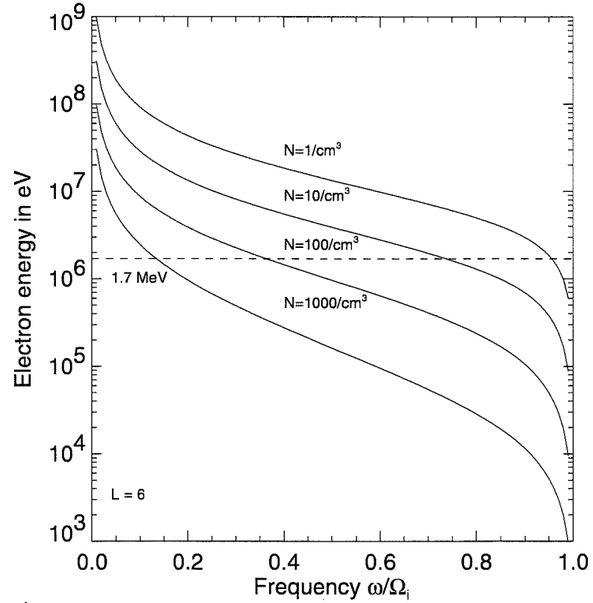

Figure 4.7: Electron parallel resonance energy for various densities and EMIC mode frequencies calculated using Equation 4.14.

shows that the plasmapause location varies with local time, and that there is a bulge in the plasmapause located on the duskside. The bulge in the plasmasphere occurs because plasma near the Earth is corotating, while plasma further away from the Earth is governed by the dawn-dusk electric field. Combining convection from both these effects creates a bulge on the duskside. Changes in the dawn-dusk electric field with magnetic activity will vary the shape and position of the bulge region. In Figure 4.9, the bulge extends to about $L = 5.5$, but these data were taken when K_p was about 2-4, higher than when the REP event was observed. The plasmapause is more compressed during magnetically active times. Therefore, it is reasonable to assume that the field line mapping to the balloon location was near the plasmapause, and the relativistic electrons could have been precipitated by interaction with EMIC waves on the equator.

In addition to the main plasmapause bulge, smaller, detached plasma regions are also

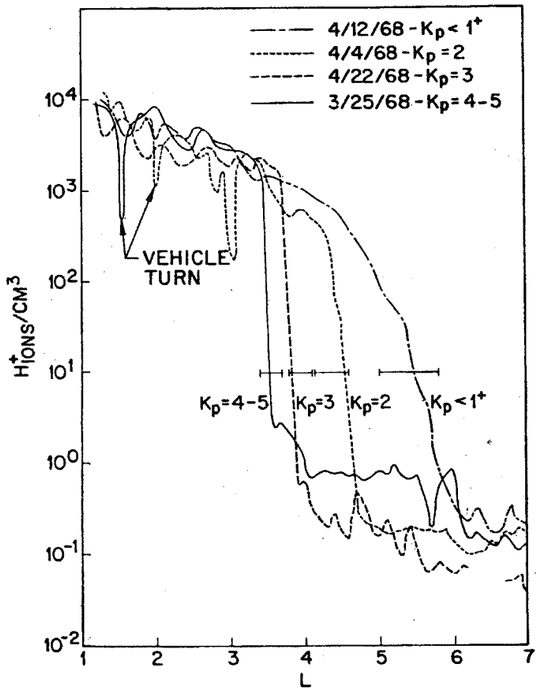

Figure 4.8: Typical nightside equatorial ion densities indicating plasmapause locations for various levels of magnetic activity [*Chappell et al.*, 1970].

observed on the duskside. These regions contain cold, dense plasma as in the plasmasphere, but are either not connected to the main plasmasphere or are connected only in a small region. *Moldwin et al.* [1996] has found that these regions are observed in association with the growth phase of magnetic substorms.

We do have cold plasma density measurements from the LANL geosynchronous satellites, which were shown in Figure 3.18 in the previous chapter. Unfortunately, no satellites were located at exactly the same local time as the balloon, but the data indicate that densities between 50 and 100 cm^{-3} are not unreasonable for that day.

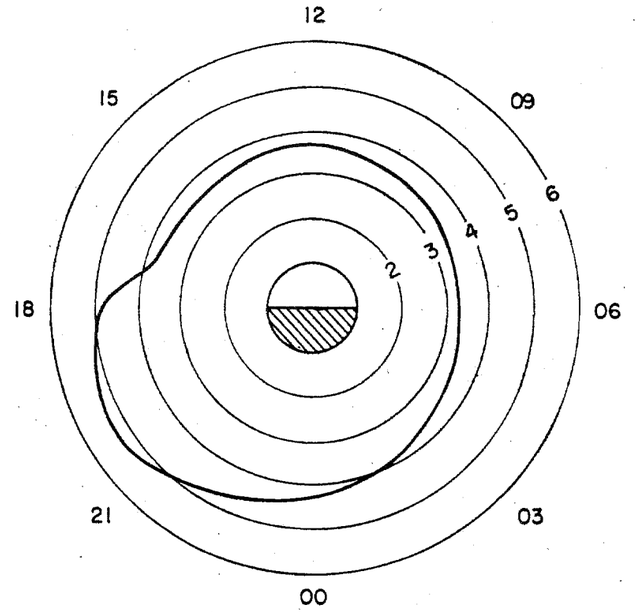

Figure 4.9: The position of the duskside bulge in the plasmapause, as determined from whistler data at moderately active times (K_p = 3-4) [*Carpenter*, 1970].

It was suggested by *Foat et al.* [1998] that the 10-20 second periodicity (0.05-0.10 Hz) seen in the X-ray count rate was the frequency of the ion cyclotron wave that was resonating with the electrons. For an L-shell of 6, Ω_i will be about 2 Hz, so the X-ray modulation frequency corresponds to 0.025-0.050Ω_i on this L-shell. From Figure 4.7, it can be seen that for such a low wave frequency, the densities needed for resonance with the 1.7 MeV electrons would be unphysically high. However, it is likely that the frequency of the X-ray modulations does not actually represent the EMIC mode wave frequency, since the mechanism pitch-angle scatters the electrons independent of the wave phase. Another mechanism, such as modulation of the EMIC wave growth, is probably responsible for producing the 10-20 second periodicity.

4.4 Field Line Resonances

Another way that relativistic electrons could be precipitated is through interaction with a field line resonance. A field line resonance is simply an Alfvén wave whose wavelength is equal to an integer multiple of the length of the magnetic field line on which it propagates. Frequencies are usually in the Pc 5 ULF range. This mechanism is suggested by the similarities in the period of the observed field line resonance, ~200 seconds, and the period of the X-ray bursts, 100-200 seconds. We compare Esrange magnetometer data to the X-ray data to see if the similarity in frequency is more than coincidental. Figure 4.10 shows the variation of the eastward magnetic field component measured on the ground and the X-ray counts measured on the balloon. The complete magnetometer measurements were shown previously in Figure 3.8. A cross-correlation between magnetometer and X-ray data gives a coefficient of about 0.5 for a 4-minute time lag, indicating the likelihood of a relationship.

Observations linking Pc 5 ULF waves with relativistic electrons have been confined to electrons trapped in the radiation belts. Recently, *Rostoker et al.* [1998] and *Hudson et al.* [1999a, b] have focused attention on these observations. Their models use Pc 5 ULF waves to energize electrons in a range of L-shells over periods of hours. While these mechanisms may account for the relativistic electrons trapped in the radiation belts, they do not specifically link the Pc 5 ULF waves to localized precipitation of relativistic electrons.

On the other hand, observations linking Pc 5 ULF waves with precipitation of electrons have been restricted to much lower energy electrons. Although field line resonances occur frequently, there have only been a small number of observations relating field line resonances to modulation in precipitating electrons of keV energies [*Samson et al.*, 1991; *Xu et al.*, 1993]. The exact mechanism linking field line resonances to precipitation is not known, although several candidates have been suggested. These mechanisms can be divided into two categories, direct and indirect. Field line resonances can play a direct role in precipitating electrons through mode conversion to electron inertia waves or kinetic Alfvén waves. These waves can then directly resonate with the electrons, causing precipitation. However, the electron energies involved in direct modulation are on the order of 2 keV or less [*Xu et al.*, 1993]. Field line resonances can also play an indirect role in precipitation electrons by modulating the growth of another wave mode or current instability. The electron energies involved in indirect modulation are greater than 3 keV [*Samson et al.*, 1991].

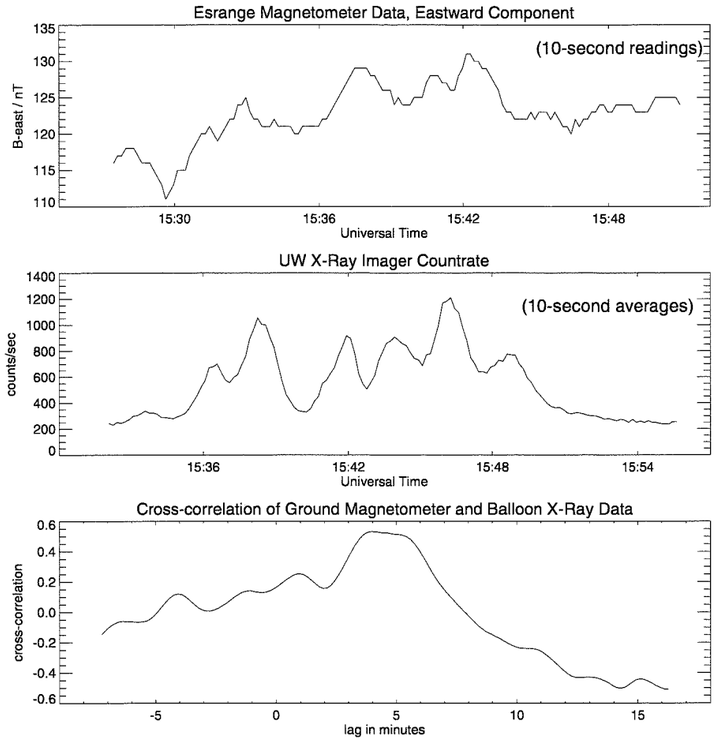

Figure 4.10: Cross-correlation between field line resonances and X-ray bursts reveals that the data agree best with a 4-minute time lag.

Since we determined in the previous section that wave-particle interaction with EMIC mode waves could produce relativistic electron precipitation of the observed type, it is possible that the field line resonance was indirectly involved in modulating the EMIC mode wave-particle interaction, and thus modulating the precipitation. This modulation could occur through the mechanism suggested by *Coroniti and Kennel* [1970], in which the growth of the waves is modulated by the magnetic pulsations. Alternatively, the modulation could

occur because the field line resonance was modulating the magnetic field strength or density, and changing the relativistic electron resonant energy for interaction with EMIC mode waves.

This situation can be illustrated by a simple calculation of the resonant electron energy using Equation 4.14. Although we do not know the amplitude of the field line resonance at the equator, we estimate 10 nT based on observations of duskside Pc 5 waves associated with EMIC mode waves [*Mauk and McPherron*, 1980; *LaBelle et al.*, 1988]. If the magnetic field strength changed by 10 nT at the equator at $L = 6$, E_{res} would change from 1.5 MeV to 1.6 MeV, assuming a density of 50 cm^{-3} and a wave frequency of $0.5\Omega_i$. If there were significantly fewer 1.6 MeV electrons than 1.5 MeV electrons at the equator, this variation in resonant energy could translate into bursts in the data. However, it would also result in a change in spectral shape between peaks and valleys, which was not observed in the August 20 REP event.

Further evidence to suggest that any field line resonance effects on the REP event were indirect, is the fact that the field line resonance began before the REP event and lasted for a much longer time. If the field line resonance directly caused the precipitation, then both events should have started and ended at the same time.

4.5 Relationship Between REP Event and Substorm

Previous statistical studies of radio wave observations of REP events and substorms have shown some connection between these two types of events [*Thorne and Larsen*, 1976]. In addition, riometer observations also suggest a correlation between substorms and localized, high-energy electron precipitation in the afternoon sector [*Ranta et al.*, 1997]. The substorm framework also provides some information as to what was happening in the magnetosphere at the time of the REP event. Therefore, we will look at the substorm data in some detail. The REP event began when the balloon was located at ~1835 MLT, on an L-shell of 5.8. There were no satellites near this particular field line, so the magnetospheric characteristics must be determined from knowledge of the general shape of the magnetosphere and from calculations of the expected motion of particles observed by

geosynchronous satellites.

Based on the Polar UVI data shown in Figure 3.12 of the previous chapter, the substorm onset was at 1512 UT. This onset time also agrees with the time when the almost dispersionless injection was observed at the LANL geosynchronous satellite 1994-084 in the proton data, although there was an unfortunate data dropout in the satellite telemetry from about 1500 UT to 1508 UT. See Figures 3.15 and 3.16 in the previous chapter for geosynchronous data.

In order to determine the time difference between the substorm onset and the REP event, it is also necessary to determine when the X-ray event began. Looking back at Figure 3.3 in the previous chapter, we see that the REP event could be considered to start at 1533 UT, with the first small burst, or at 1536 UT, when the larger bursts started. For purposes of comparing with satellite data, we choose the later time since the X-ray event was much more intense then. It seems likely that the first of the seven bursts was so small that its signature would not be visible in satellite data sets. Therefore, we conclude that the REP event began 24 minutes after the substorm injection.

Because of the gradient and curvature in the Earth's magnetic field, charged particles in the magnetosphere drift around the Earth in longitude. Electrons drift eastward and protons drift westward. The bounce-averaged drift velocity for particles in the Earth's magnetosphere is dependent only on the magnetic field strength and the particle energy and pitch-angle. The gradient-curvature drift velocity in a dipole magnetic field can be estimated from the following formula

$$V_D = 2.56 \times 10^6 \left(0.7 + 0.3 \sin \alpha\right) L \, \gamma m v^2 \tag{4.15}$$

where V_D is the drift velocity in degrees per minute, α is the pitch-angle on the equator, and L is the magnetic L-shell where the particles are located [*Roederer*, 1970]. Equatorially mirroring particles correspond to the $\alpha \approx 90°$ case, and marginally trapped particles correspond to the $\alpha \approx 0°$ case. This equation is not as accurate for pitch angles less than $40°$, but is acceptable for the purpose of finding an approximate range of arrival times.

Since the balloon was located on the duskside of the Earth, protons injected near midnight have a shorter distance to drift around to the balloon region, and will arrive much

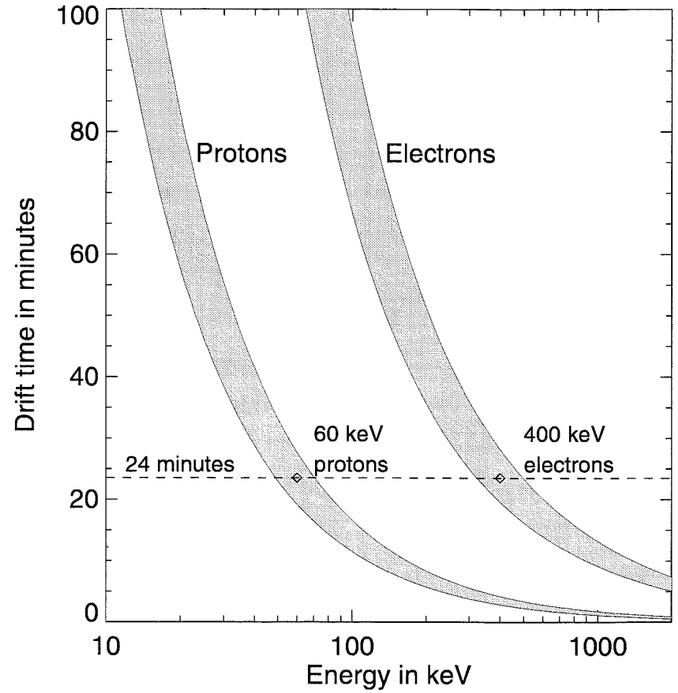

Figure 4.11: Gradient-curvature drift times in minutes for particles drifting around the Earth at $L = 6$, from the LANL satellite 1991-084 at 175° magnetic longitude (near midnight) to the balloon field line at 118° magnetic longitude (near dusk). The shaded region of each curve gives the range of drift times for $\alpha \approx 0°$ to $\alpha \approx 90°$.

more quickly than electrons of the same energy, which must drift a longer distance. Figure 4.11 gives values for the time it would take particles of various pitch-angles and energies to drift from the substorm injection region to the magnetospheric region that maps to the balloon. Refer back to Figure 3.14 for the relative positions of the satellites, the balloon and the substorm injection in magnetic coordinates. Although the balloon was located at $L \sim 5.8$ and the geosynchronous satellites were located at $L \sim 6.6$, it is reasonable to assume that the injection region was large enough to cover both L-values, based on Polar satellite images of the latitudinal width of the substorm injection region.

Since the substorm onset occurred about 24 minutes before the REP event, Figure 4.11 provides further evidence that the mono-energetic 1.7 MeV electrons did not originate in the substorm injection. Such high energy electrons would have drifted past the balloon field lines well before any precipitation was observed, about 6-8 minutes after the substorm onset. In addition, as mentioned in Chapter 3, none of the geosynchronous satellites observed an increase in the MeV electron population, which leads to the conclusion that the REP event was not due to a substorm-related enhancement of relativistic electrons in the magnetosphere. The REP event must therefore have been caused by some mechanism that selectively precipitates only the high-energy part of the ambient electron population.

Figure 4.11 does give some clues as to the nature of a possible energy-selective precipitation mechanism. The figure shows that 24 minutes after the substorm injection, protons of energy ~60 keV would arrive at the region of the magnetosphere mapping near the balloon. This coincidence is significant because a drifting warm proton population could lead to the growth of ion cyclotron waves that have been shown to interact with relativistic electrons. The figure also shows that 24 minutes after the substorm injection, ~400 keV electrons would arrive at the region of the magnetosphere mapping near the balloon. However, data shown previously in Figure 3.15, does not show much enhancement in the electron flux at these energies. If we had chosen the earlier X-ray event start time and determined a 21-minute lag between the substorm injection and the REP event, this interpretation would not change significantly.

A further indication that the substorm proton injection may be related to the REP event is the similarity in the time structure of 50-75 keV electrons and X-ray count rates. We can perform a simple cross-correlation analysis to determine the likelihood of a relationship between these two events. Figure 4.12 shows LANL proton data, X-ray imager data and the cross-correlation coefficients for different time lags. Note that there are two almost identical peaks of height 0.6 in the cross-correlation data, corresponding to offsets of 20.7 and 23.5 minutes. Data in the upper two panels are plotted with a 20.7 minute offset, lining up the LANL data with the first of the seven X-ray imager peaks.

Based on these simple drift calculations and estimates of wave-particle interactions presented in this chapter, we conclude that the most likely mechanism for precipitation of

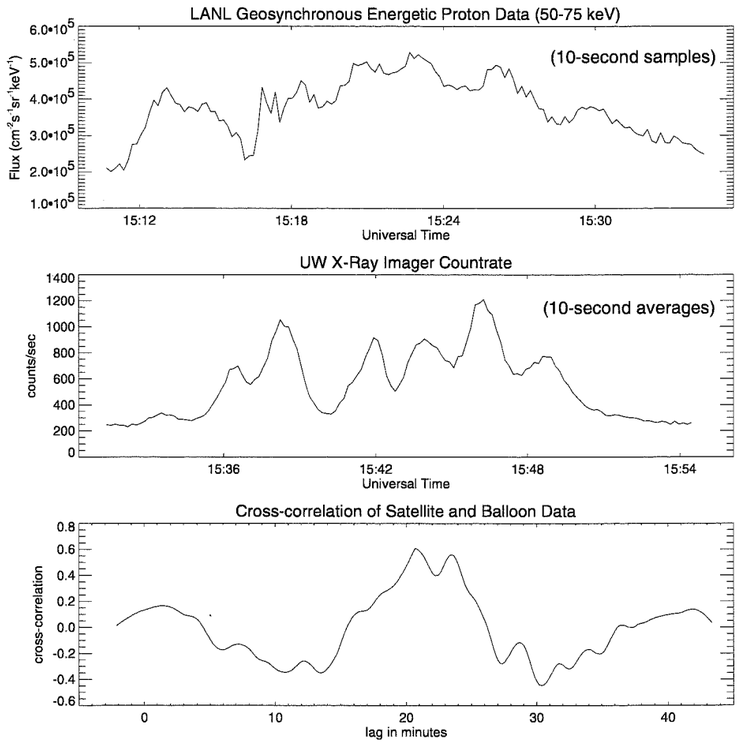

Figure 4.12: Cross-correlation between protons observed by the LANL satellite and X-rays observed by the balloon.

MeV electrons is interaction with electromagnetic ion cyclotron waves. In the next chapter, the growth of this wave mode due to drift anisotropies in the substorm injected protons, and associated pitch-angle diffusion are investigated in more detail.

Chapter 5

A SIMPLE MODEL FOR DUSKSIDE RELATIVISTIC ELECTRON PRECIPITATION

In the previous chapter, we discussed several different mechanisms for precipitation of relativistic electrons, and concluded that wave-particle interactions are the best candidate for matching the characteristics of the observed REP event. In particular, the electromagnetic ion cyclotron mode is the most probable wave mode for producing mono-energetic 1.7 MeV electron precipitation on the duskside, in association with a magnetospheric substorm. In this chapter, we present a simple model using wave-particle interactions to link the substorm observations with the REP observations.

Figure 5.1 shows a cartoon representation of the model. The cartoon shows an equatorial slice through the magnetosphere, with an idealized view of the plasmapause and its duskside bulge. Three main components of the model are: 1) the westward drift of substorm-injected warm protons, 2) the region of wave growth inside the high-density plasmasphere, and 3) the location of wave interaction with eastward-drifting ambient relativistic electrons, also preferentially inside the high-density plasmasphere. This basic idea was first proposed by *Thorne and Kennel* [1971] and was further expanded upon by *Lyons and Thorne* [1972] and *Thorne* [1974]. In addition to explaining the observed electron energies and localized duskside precipitation, this model also accounts for the slight westward drift seen in the riometer images of Figure 3.9.

Previous satellite observations have shown that electromagnetic ion cyclotron waves are preferentially excited on the duskside in high-density regions. Detailed analysis of several observations of electromagnetic ion cyclotron waves by *Mauk and McPherron* [1980] has shown that these waves are excited when warm ring current ions encountered a cooler region of dense plasma on the duskside. *LaBelle et al.* [1988] have observed examples

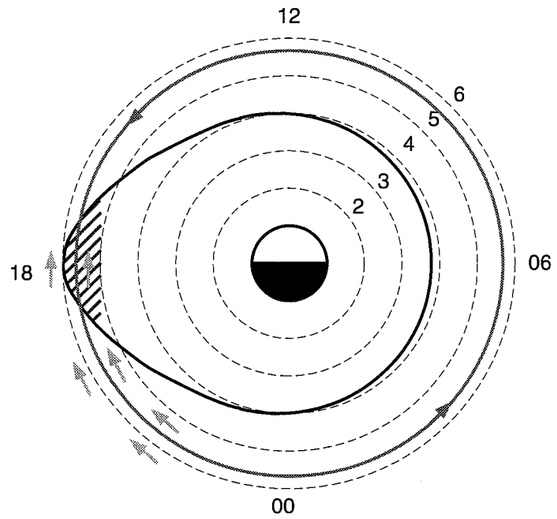

Figure 5.1: A cartoon explanation of the duskside REP model, after *Thorne and Kennel* [1971]. The egg-shaped region represents an idealized plasmapause. The short arrows show the drift of substorm-injected protons towards dusk. The hatched region inside the plasmapause represents the region where electromagnetic ion cyclotron wave growth is driven. The solid circle shows the approximate direction of drift of ambient relativistic electrons in the radiation belts. These electrons are present at all local times, but interact with ion cyclotron waves only in the hatched region inside the plasmapause.

of EMIC mode waves inside the plasmasphere coincident with the arrival of warm ring current ions. *Anderson et al.* [1992] carried out a statistical study of the occurrence of Pc 1-2 EMIC waves. They found that although these waves occur most commonly for $L > 7$, waves do occur predominantly in the afternoon sector in the $L = 6$-7 range. These observations agree with theoretical predictions of *Cornwall et al.* [1970], *Perraut and Roux* [1975], and *Jordanova et al.* [1997].

In Chapter 4, we showed that the interaction of EMIC mode waves with relativistic electrons depended upon plasma density and wave frequency. Although we have plasma density measurements from LANL geosynchronous satellites, we have no direct wave frequency measurements. However, we can determine if waves are likely to be present, and at what frequencies, by examining sources of free energy for the wave growth. One source of free energy that can cause EMIC wave growth is a proton temperature anisotropy. When protons have a greater average kinetic energy in the perpendicular direction than in the parallel direction, EMIC waves can grow. Gradient-curvature drift can produce such a temperature anisotropy since particles with more perpendicular velocity drift faster.

In the first section of this chapter, the drift of substorm-injected protons is investigated, and the distribution of protons on the duskside is determined using input data from geosynchronous satellites. In the second section, linear theory is used to calculate EMIC wave growth from the duskside proton distribution. In the third section, model predictions are compared to observations, and limitations of the model are discussed.

5.1 Drift of Substorm-Injected Protons

5.1.1 Overview of the Drift Model

Following the method of *Solomon* [1975] and *Lin and Parks* [1976], we determine how the distribution of substorm-injected protons changes as the particles gradient-curvature drift in a magnetic field. This method uses the same approximation for drift velocity as given previously in Equation 4.15. Before describing the drift model, we define some necessary terms.

In order to investigate the motion of particles, we consider a distribution in phase space, $f(\vec{r}, \vec{v}, t)$, where $\vec{r}$ is position, $\vec{v}$ is velocity, and t is time. Note that this distribution is in velocity phase space and not momentum phase space. Since we are interested in the distribution of non-relativistic protons, velocity phase space is more convenient. The distribution function satisfies the Vlasov equation,

$$\frac{\partial f}{\partial t} + \vec{v} \cdot \nabla f + \vec{a} \cdot \nabla_v f = 0, \tag{5.1}$$

where $\vec{a}$ is an acceleration that is determined by forces independent of velocity, such as the Lorentz force. The Vlasov equation is simply a continuity equation for a collisionless plasma.

Liouville's theorem, which can be derived from the Vlasov equation [*Kivelson and Russell*, 1995], says that phase space density is constant along a particle trajectory. Therefore we can take differential elements in phase space, calculate how long they will take to drift from nightside to duskside, and determine the new distribution functions on the duskside for various time intervals.

One typical distribution function is an isotropic Maxwellian, which is given by

$$f(v_x, v_y, v_z) = \left(\frac{N}{(2\pi)^{3/2} V_T^3}\right) \exp\left(-\frac{v_x^2 + v_y^2 + v_z^2}{2V_T^2}\right) \tag{5.2}$$

where N is the number density, v_x, v_y ,and v_z give the particle velocity, and V_T is the thermal velocity. The exponential part of this equation is sometimes written as $\exp(-E/E_0)$ where $E = mv^2/2$ and $E_0 = mV_T^2$.

Another distribution function that is frequently seen where particles are constrained by a magnetic field is a bi-Maxwellian, which is given by

$$f(v_\parallel, v_\perp) = \left(\frac{N}{(2\pi)^{3/2} V_{T\perp}^2 V_{T\parallel}}\right) \exp\left(-\frac{v_\perp^2}{2V_{T\perp}^2} - \frac{v_\parallel^2}{2V_{T\parallel}^2}\right) \tag{5.3}$$

where $v_\parallel$ ($v_\perp$) is the particle velocity parallel (perpendicular) to the magnetic field and $V_{T\parallel}$ ($V_{T\perp}$) is the thermal velocity parallel (perpendicular) to the magnetic field.

The distribution given in Equation 5.3 can be completely characterized by three parameters, the number density, N, the average kinetic energy, E_{avg}, and the temperature anisotropy, A. The number density can be determined from

$$\begin{aligned} N &= \int f \, d^3v \\ &= 2\pi \int_0^\infty \int_{-\infty}^\infty f \, v_\perp \, dv_\perp \, dv_\parallel. \end{aligned} \tag{5.4}$$

The average kinetic energy can be determined from

$$\begin{aligned} E_{avg} = \left\langle \frac{1}{2} m v^2 \right\rangle &= \frac{1}{N} \int \frac{1}{2} m v^2 \, f \, d^3v \\ &= \frac{2\pi}{N} \int_0^\infty \int_{-\infty}^\infty \frac{1}{2} m v^2 \, f \, v_\perp \, dv_\perp \, dv_\parallel. \end{aligned} \tag{5.5}$$

For a bi-Maxwellian distribution this equation gives

$$E_{avg} = \left\langle \frac{1}{2} m v^2 \right\rangle = m V_{T\perp}^2 + \frac{1}{2} m V_{T\parallel}^2. \tag{5.6}$$

This average kinetic energy is related to the parallel and perpendicular temperatures by

$$E_{avg} = k_B T_\perp + \frac{1}{2} k_B T_\parallel \tag{5.7}$$

where k_B is the Boltzmann constant. Note that for the case of an isotropic Maxwellian distribution defined in Equation 5.2, $T = T_\perp = T_\parallel$ and $E_0 = k_B T = (2/3) E_{avg}$. The temperature anisotropy is defined by

$$A = \frac{T_\perp}{T_\parallel} - 1 = \frac{V_{T\perp}^2}{V_{T\parallel}^2} - 1. \tag{5.8}$$

Using these definitions, a simple computer program is used to determine the distribution function at a particular location on the duskside, given an initial bi-Maxwellian distribution in space and time on the nightside.

5.1.2 *Initial Conditions for the Drift Model*

The initial distribution is a combination of a bi-Maxwellian distribution in velocity space, some spatial distribution in longitude, and some temporal distribution. Since we assume a dipole magnetic field, all calculations are done for $L = 6$. We choose a longitudinal distribution with a Gaussian shape,

$$f(\phi) = \exp\left(-\frac{\phi^2}{(\Delta\phi)^2}\right) \tag{5.9}$$

where ϕ is longitude and $\Delta\phi$ was taken to be $5°$, which approximately matches the width of the brightening region in the Polar UVI image near the footprint of the geosynchronous satellite (see figure 3.11 in Chapter 3). We assume that the longitudinal width of the brightening region in the ionosphere is approximately the same as the longitudinal width of the injection region at the equator.

No angular data were available to constrain the value of A for the bi-Maxwellian distribution, so we chose a value of 3. Previous observations of temperature anisotropies in substorm-injected particles have extended up to values near 2 observed for energies between a few eV and 81 keV [*Parks et al.*, 1980]. Since this model separates the ions into a cold isotropic component and a warm anisotropic component, a large anisotropy in the

warm component is acceptable since the overall anisotropy for both ion components is still small. Values for N and E_{avg} are determined from 50-400 keV proton data from the SOPA instrument on the LANL geosynchronous satellite. The top panel of Figure 5.2 shows the proton substorm injection period with more detail than in Chapter 3. The dashed horizontal lines show the level of the average background flux observed between 1423 and 1458 UT. The solid vertical lines identify the time periods shown in the bottom two panels. At the beginning of the injection, the flux increases only in the lowest energy channels, 50-113 keV. A few minutes later, flux increases in the three higher energy channels, 113-400 keV, while remaining high in the lowest energy channels. About halfway through the injection, the flux in the three higher channels returns almost to the background level, while the flux in the two lowest energy channels remains high.

Since the energy spectra appear to switch between two distinct forms, we plot spectra from two representative time periods in the lower panels of Figure 5.2. The lower left panel shows spectra from when all five channels are high, and the lower right panel shows spectra from when only the two lowest energy channels are high. Values for the energy and density of the injected particles are determined as described below.

The SOPA instrument measures flux, $j(E)$, in units of $\mathrm{cm}^{-2}\ \mathrm{s}^{-1}\ \mathrm{ster}^{-1}\ \mathrm{keV}^{-1}$. In order to determine values for the distribution function, $f(v)$, in units of $\mathrm{cm}^{-6}\ \mathrm{s}^{3}$, we use

$$j(E) = \frac{2E}{m^2} f(v). \tag{5.10}$$

We assume the distribution is Maxwellian, so we fit the flux data to $j(E) \propto E \exp(-E/E_0)$ and determine E_0. The two lower panels of Figure 5.2 show typical fits to the four lowest-energy channels of the background-subtracted flux data. Clearly, the data are not perfectly Maxwellian, but the fit gives an adequate estimate for use in our simple model.

In order to find the density, N, we use Equation 5.4, converted from an integral over distribution function to a sum over flux,

$$N \approx 4\pi \sum j(E) \sqrt{\frac{m}{2E}} \Delta E \tag{5.11}$$

Densities for the hot injected protons are calculated using this equation for the energy channels between 50 and 400 keV. As with the values for E_0, the density values obtained in this manner should be considered to be approximate guidelines only.

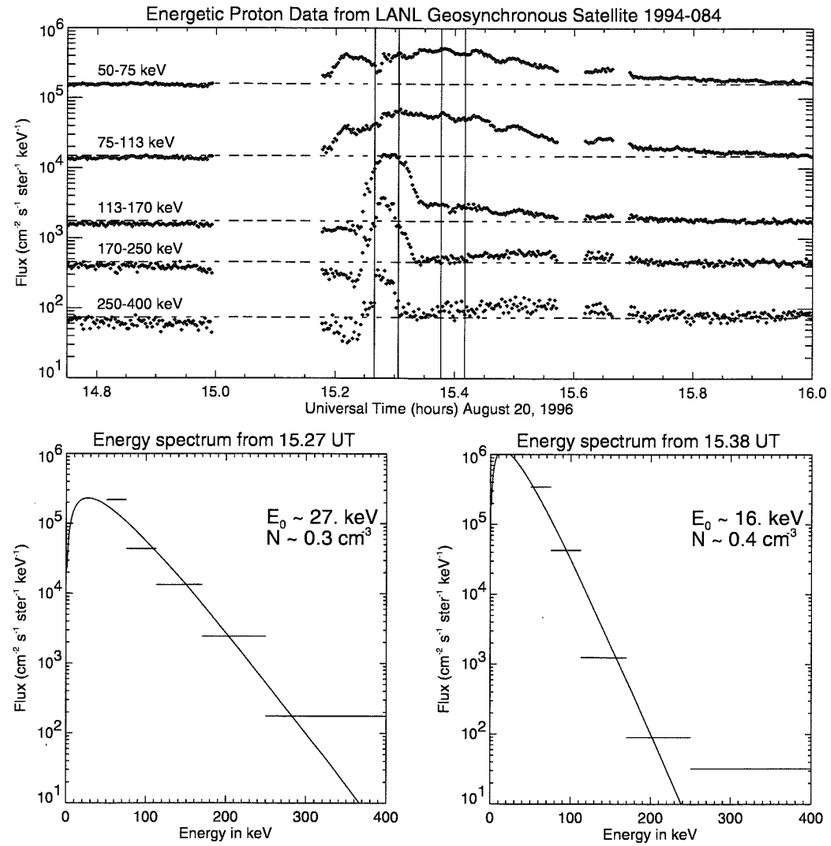

Figure 5.2: Proton injection data from LANL geosynchronous satellite 1994-084. The top panel shows the proton flux during the substorm injection. The horizontal dashed lines give the background flux, determined from 1423 to 1458 UT. The solid vertical lines identify the 2.5 minute intervals shown in the bottom two panels. These two panels show background-subtracted spectra and a least squares fit to $E \exp(-E/E_0)$ for the four lowest-energy channels.

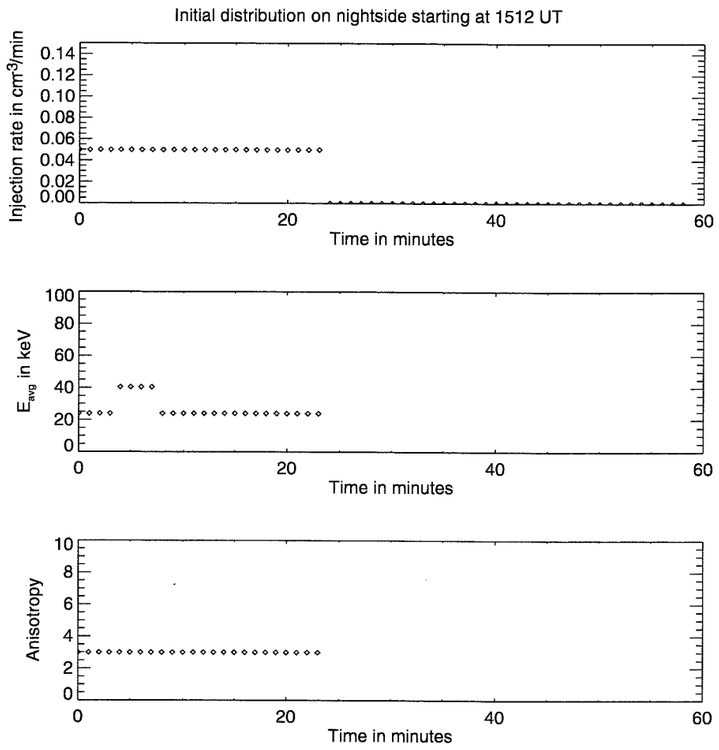

Figure 5.3: Initial nightside conditions for the injection rate, average energy and temperature anisotropy of the proton drift simulation.

Since we do not have angular distributions from the SOPA instrument, we assume $A = 3$ as a starting point. Figure 5.3 shows the initial conditions on the nightside for the drift calculation. We choose a constant injection rate lasting for 20 minutes, to roughly match the satellite observations. The substorm injection rate is chosen to be 0.05 cm^{-3} min^{-1}, to produce a maximum density of 0.4 cm^{-3} on the nightside.

From these initial conditions, we follow elements in phase space from the nightside injection point at magnetic longitude 175° to the duskside observation point at magnetic longitude 118°, and accumulate new distribution functions. We then calculate the density,

average energy, and anisotropy from these new distribution functions.

5.1.3 Results of Drift Model

Figure 5.4 shows the final conditions on the duskside for the drift calculation. The upper panel shows that the density starts low, and gradually increases with time, until the maximum density occurs 40 minutes after the injection started. The middle panel shows that the average energy starts high and decreases. This decrease in average energy occurs because the higher energy particles drift faster and arrive earlier on the duskside. The bottom panel shows that the anisotropy also starts high and decreases. This decrease in anisotropy occurs because the particles with larger pitch-angle, or more perpendicular velocity, drift faster. These larger pitch-angle particles arrive earlier on the duskside, creating higher temperature anisotropies.

We also use this model to investigate the temporal variations in the injected proton data. We take as input a time series that has approximately the same temporal variations as the satellite data and some that have more pronounced pulsations, but find that the pulsations are completely smoothed out of the time series after the protons drift to the duskside. From these results we conclude that the temporal variations in the X-ray data are not related to the temporal structure in the substorm injection, despite the high correlation shown previously in Figure 4.12.

In the next section, we use the density, average energy, and anisotropy obtained from this drift model to determine the growth of EMIC mode waves.

5.2 Growth of Electromagnetic Ion Cyclotron Mode Waves

5.2.1 Ion Cyclotron Dispersion Relation for Parallel Propagation

The cold-plasma dispersion relation for parallel-propagating EMIC mode waves, given in Equation 4.13 of the previous chapter, is an approximation that gives only the real part of the wave frequency. The equation tells nothing about the imaginary part of the frequency, or the wave growth. To evaluate wave growth, a complex form of the dispersion relation is needed. Kinetic theory, which takes into account the distribution function of the particles,

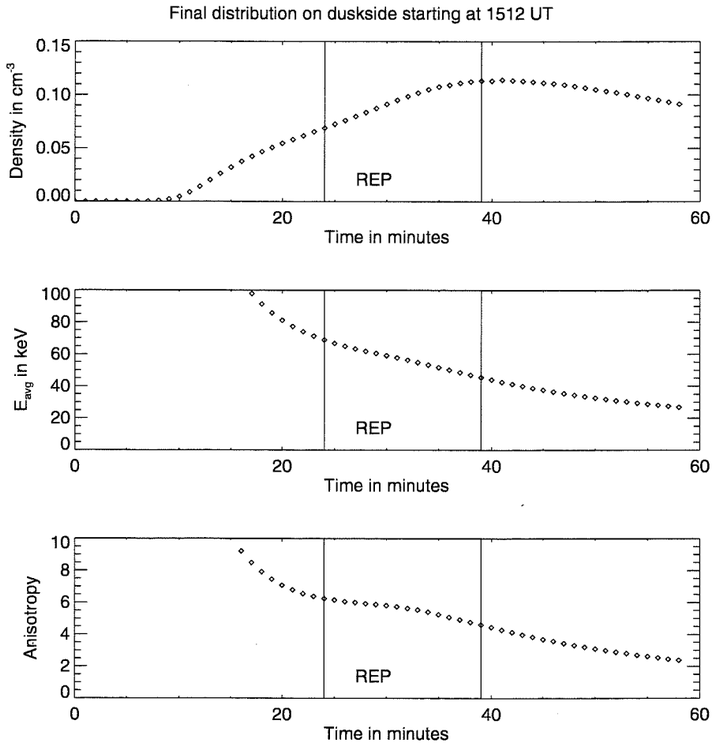

Figure 5.4: Final duskside results for the density, average energy and temperature anisotropy of the proton drift simulation.

gives such a dispersion relation, assuming that $\omega_{real} \gg \omega_{imag}$ so that equations can be linearized.

By combining the Vlasov equation given in Equation 5.1 with Maxwell equations for a bi-Maxwellian particle distribution, the wave equation can be written as

$$\Lambda_{ij}(\omega, \vec{k}) E_j(\omega, \vec{k}) = 0. \tag{5.12}$$

Here, E_j is the wave electric field and Λ_{ij} is given by

$$\Lambda_{ij}(\omega, \vec{k}) = \frac{c^2}{\omega^2}(k_i k_j - k^2 \delta_{ij}) + K_{ij}(\omega, \vec{k}). \tag{5.13}$$

For a bi-Maxwellian distribution function such as given in Equation 5.3, the following expression for the dielectric tensor is obtained [*Melrose*, 1986]

$$K_{ij}(\omega, \vec{k}) = \delta_{ij} - \sum_{\alpha} \frac{\omega_{p\alpha}^2}{\omega^2} \left[A_\alpha a_{ij}(k) - \frac{\omega^2}{k_\parallel^2 V_{T\alpha\parallel}^2} b_i b_j + \sum_{s=-\infty}^{\infty} \zeta_{\alpha s} Z(\zeta_{\alpha s}) \left\{ \frac{\omega}{\omega - s\Omega_\alpha} + A_\alpha \right\} N_{ij}(\omega, \vec{k}, s) \right] \tag{5.14}$$

where the magnetic field is in the z-direction, α is the plasma component (for example: cold electrons, cold ions, or warm ions), ω is the complex frequency, $\omega_{p\alpha}$ is the plasma frequency, Ω_α is the gyrofrequency, A_α is the temperature anisotropy defined in Equation 5.8, a_{ij} is a tensor involving only k, b_i is a unit vector in the magnetic field direction, and N_{ij} is a tensor involving Bessel functions. The other terms in this expression are the plasma dispersion function [*Stix*, 1992],

$$Z(\zeta) = \frac{1}{\sqrt{\pi}} \int_{-\infty}^{\infty} \frac{e^{-z^2}}{z - \zeta} \, dz, \tag{5.15}$$

and

$$\zeta_{\alpha s} = \frac{(\omega - s\Omega_\alpha)}{\sqrt{2} k_\parallel V_{T\alpha\parallel}}. \tag{5.16}$$

For cold plasma, ζ_α is large, and the plasma function can be approximated using an asymptotic expansion

$$Z(\zeta) \approx i\sqrt{\pi} \exp(-\zeta^2) - \left(\frac{1}{2\zeta} + \frac{1}{4\zeta^3} + \ldots \right) \tag{5.17}$$

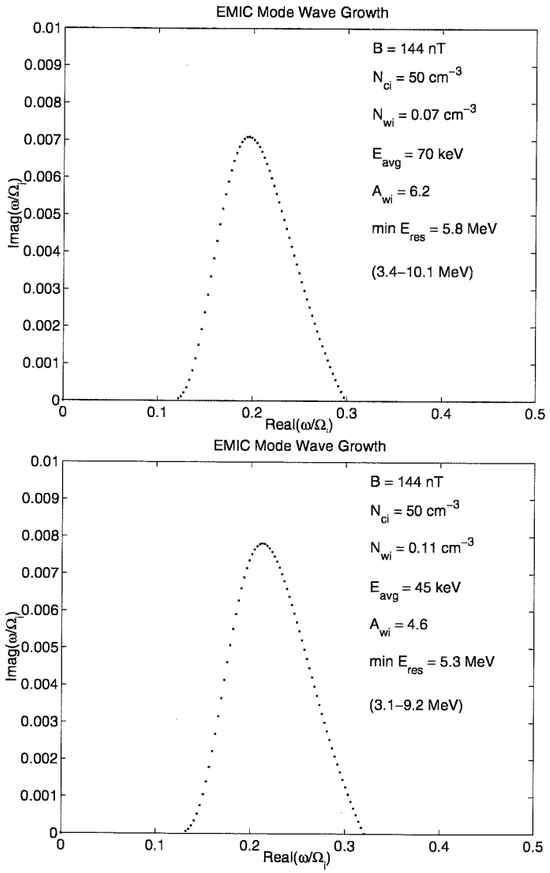

Figure 5.5: Electromagnetic ion cyclotron growth rate for parallel approximation. The top (bottom) panel shows growth rates corresponding to the conditions at the start (end) of the REP event predicted by the drift model.

Magnetic field strength

The top panel of Figure 5.6 shows the the wave frequency as a function of the magnetic field strength, B. The top horizontal axis shows values for the dipole L-value corresponding to each magnetic field strength. The vertical lines indicate the parameter used in calculating the wave growth shown previously in the bottom of Figure 5.5. The bottom panel of Figure 5.6 has the same format as the top panel, except that the values for the minimum resonant electron energy are calculated for each frequency. Note that the upper limit for positive wave growth corresponds to the lower limit for electron resonant energy, since Equation 4.14 says that the resonant energy is inversely related to the wave frequency.

Figure 5.6 shows that the frequency of peak wave growth increases with increasing magnetic field strength. The corresponding electron resonant energy also increases with B. From Equation 4.14, the resonant energy is directly related to the square root of the magnetic energy, $B^2/8\pi N$, and inversely related to the frequency. The reason for the increase in resonant energy is that the variations due to magnetic energy dominate the variations due to frequency.

Figure 5.6 shows that if the balloon were located on a field line of larger L, it would be more likely to see precipitating electrons of energy close to 1.7 MeV. However, in our initial calculation of wave growth the L-value was chosen to be 6 because of the position of the balloon, at $L \sim 5.8$, and the satellite, at $L \sim 6.6$. Although there is no reason to believe that the actual L-value was as large as 7 or 8, if the field line strength varied due to a mechanism such as a field line resonance, the strength of the magnetic field could change causing electrons of different energy to resonate.

The calculation of field line resonance effects on REP events presented in the previous chapter considered only the effects of changing magnetic field strengths on the electron resonance energy. Here we examine the additional effect of wave growth. The effect of B on the wave frequency serves to reduce the effect of B on the electron resonance energy. A decrease in magnetic field strength of 10 nT would still reduce the electron resonance energy, as found in the earlier calculation, but by a smaller amount than if wave growth were not considered.

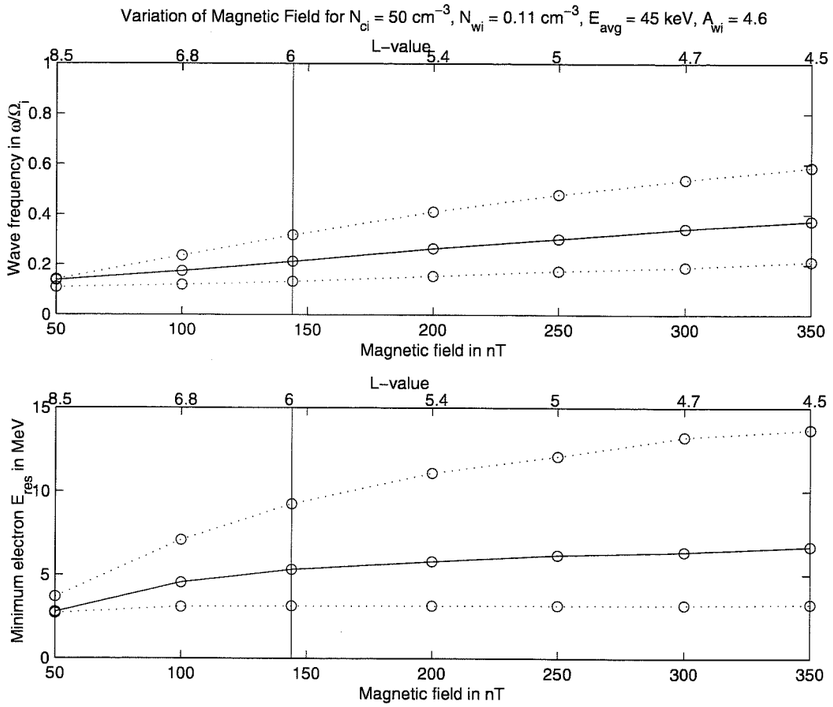

Figure 5.6: Wave frequency and electron resonance energy vs. magnetic field strength. The top axis of each panel shows the corresponding L-values and the vertical line shows the parameters used to determine the wave growth shown in the bottom of Figure 5.5.

Cold ion density

Figure 5.7 shows the variation of the wave frequency and electron resonant energy with cold ion density, N_{ci}. Again, the vertical lines in each panel indicate the parameters used in calculating the wave growth shown previously in the bottom of Figure 5.5. The top panel shows that peak wave growth frequency decreases with increasing cold ion density. However, the corresponding electron resonant energy does not show much change with density, except at cold ion densities below 10 cm^{-3}. Above this density, the line for resonant electron energy is quite flat. This result was somewhat surprising. Equation 4.14 says that the electron resonant energy is inversely dependent on cold ion density (again through the magnetic energy, $B^2/8\pi N$). However, the electron resonant energy is also inversely dependent on the wave frequency, which is in turn inversely dependent on the cold ion density. The interrelationship of these values results in an electron resonant energy independent of cold ion density above about 10 cm^{-3}.

The initial choice of this free parameter, 50 cm^{-3}, was chosen based on measurements of LANL geosynchronous satellite measurements from several hours after the event. Therefore this value is not known very accurately. If the satellite is inside the plasmapause or a detached plasma region, the cold plasma density would probably be above 10 cm^{-3}. However, if the satellite is outside the plasmapause, then the density would probably be below 1 cm^{-3}.

Warm ion density

Figure 5.8 shows the variation of the wave frequency and electron resonant energy with warm ion density, N_{wi}. The figure shows that as the warm ion density increases, the peak wave growth frequency increases, too. Correspondingly, the electron resonant energy decreases with warm ion density. This decrease in resonant energy is as expected from the equation for electron resonant energy, Equation 4.14, since the only dependence of the resonant energy on the warm ion density is through the wave frequency. Increasing the warm ion density to 1 cm^{-3} decreased the resonant electron energy to 2.7 MeV, much closer to our observations of August 20, 1996. Higher values of warm plasma density could not be

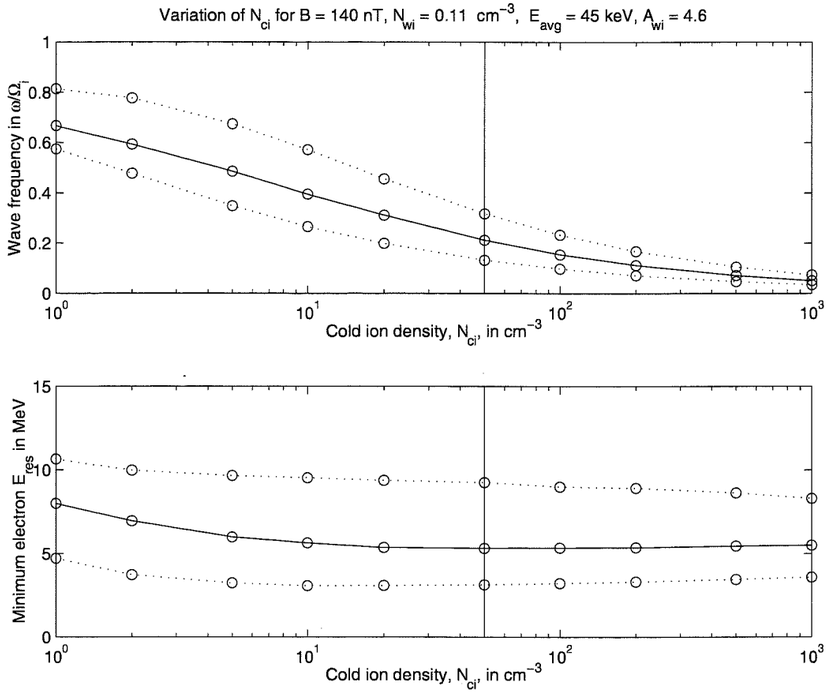

Figure 5.7: Wave frequency and electron resonance energy vs. cold ion density. The vertical line shows the parameters used to determine the wave growth shown previously in the bottom of Figure 5.5.

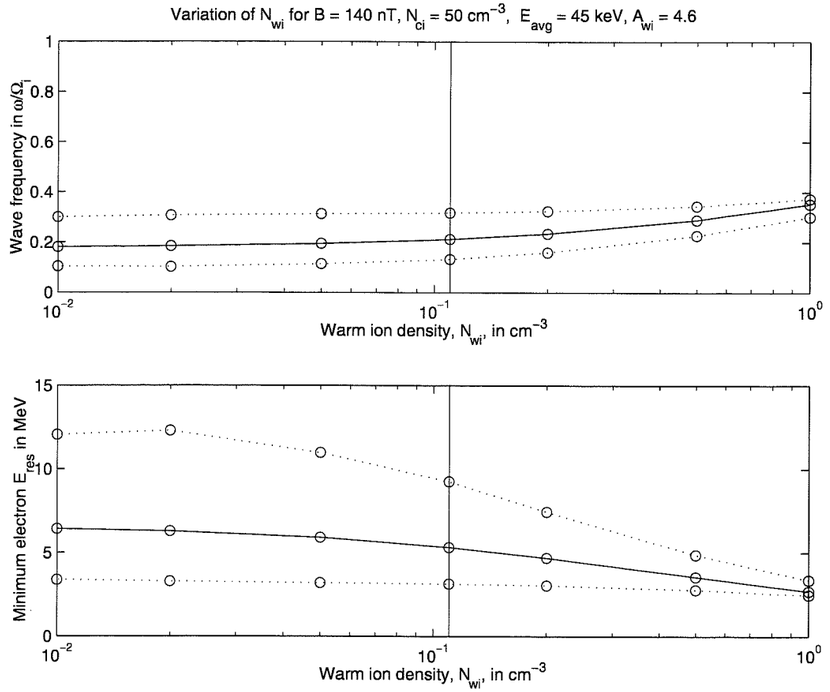

Figure 5.8: Wave frequency and electron resonance energy vs. warm ion density. The vertical line shows the parameters used to determine the wave growth shown previously in the bottom of Figure 5.5.

examined in detail, however, because our wave growth calculation assumed $\omega_{real} \gg \omega_{imag}$. This assumption begins to break down as the warm ion density increases.

The actual value for the warm ion density is not known very accurately. The value used in the initial calculations, 0.11 cm^{-3}, was estimated from drifts calculated from the geosynchronous satellite observations of proton injection. However, error could have been introduced in the satellite measurement, the drift calculation, or both. The satellite measurements extend only down to 50 keV, so if the injected particles include lower energies, this density value could be higher. Approximations such as using a dipole field in the drift calculations could also result in the actual warm ion density being somewhat higher than

the parameter used. In addition, the value for density depends on the initial temperature and anisotropy chosen for the drift calculations. We cannot set an exact limit on these errors without constructing a much more complicated model, but we can set an upper limit for reasonable warm ion density parameter using previous satellite observations. Based on ring current measurements by *Gloeckler et al.* [1985], the warm ion density could be as high as 1 cm^{-3}, but is unlikely to be higher, given the moderately quiet geomagnetic conditions on August 20, 1996.

Average energy of warm ions

Figure 5.9 shows the variation of the wave frequency and electron resonant energy with the average energy of the warm ions, E_{avg}. The figure shows that as the average energy of the warm ions increases, the peak wave growth frequency decreases. Correspondingly, the electron resonant energy increases with warm ion thermal energy. This increase in resonant electron energy with warm ion thermal energy is as expected from the equation for electron resonant energy, Equation 4.14, since the only dependence of the resonant energy on the warm ion thermal energy is through the wave frequency. Decreasing the average energy of the warm ions to 5 keV decreased the resonant electron energy to 2.1 MeV, much closer to the REP observations of August 20, 1996.

The value used for the warm ion thermal energy was determined in the same way as the value used for the warm ion density, and suffers from the same two sources of error, the satellite measurement and the drift calculation. In addition, further error could have been introduced by fitting a Maxwellian to each energy spectrum to determine the average energy.

Temperature anisotropy of warm ions

Figure 5.10 shows the variation of the wave frequency and electron resonant energy with the temperature anisotropy of the warm ions, A_{wi}. The figure shows that as the warm ion anisotropy increases, the peak wave growth frequency increases and the electron resonant energy decreases. Increasing the anisotropy to 12.6 results in a resonant electron energy

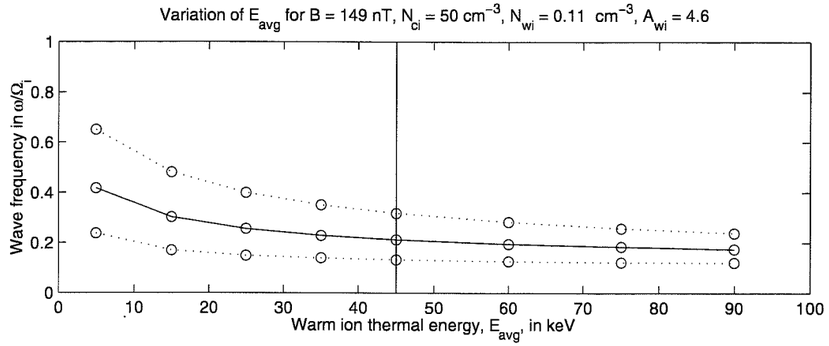

Figure 5.9: Wave frequency and electron resonance energy vs. warm ion average thermal energy. The vertical line shows the parameters used to determine the wave growth shown previously in the bottom of Figure 5.5.

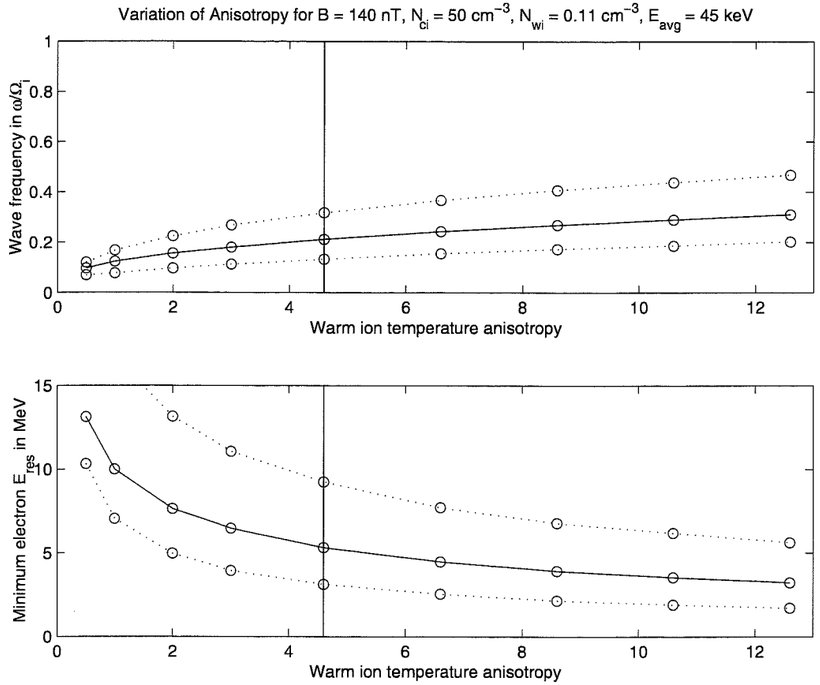

Figure 5.10: Wave frequency and electron resonance energy vs. warm ion anisotropy. The vertical line shows the parameters used to determine the wave growth shown previously in the bottom of Figure 5.5.

of 3.2 MeV, closer to the observed REP event. Since no information at all was available for the temperature anisotropy, this value is somewhat arbitrary. The values shown in this figure represent a reasonable range, since the anisotropic warm ion component is only a small part of the total ion component.

Conclusions

The conclusions to be drawn from this study of varying the five free parameters are: 1) decreasing the magnetic field strength (*i.e.* increasing the L-value) decreases the electron resonant energy, but not by much, 2) varying the cold plasma density has very little effect

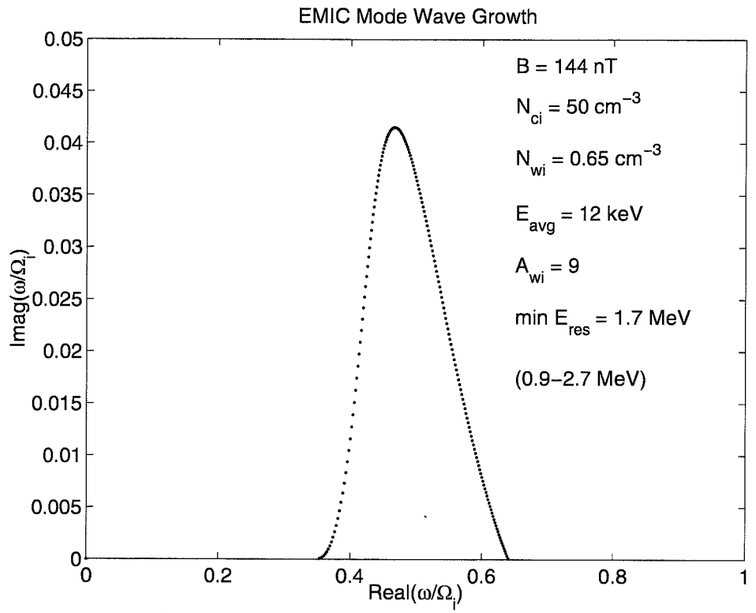

Figure 5.11: Electromagnetic ion cyclotron growth rate for the parallel approximation, using parameters selected to produce interaction with 1.7 MeV electrons.

on the electron resonant energy for plasmaspheric densities, and 3) varying the three warm ion parameters can decrease the electron resonant energy. Therefore the next question to examine is what combination of warm ion parameters is consistent with the substorm and REP observations and produces resonant electron energy closer to the observed value of 1.7 MeV.

Figure 5.11 shows wave growth from one such combination of warm ion parameters. Here we have used $L = 6$, $N_{ci} = 50$ cm^{-3}, $N_{wi} = 0.65$ cm^{-3}, $E_{avg} = 12$ keV, and $A_{wi} = 9$. The minimum electron resonant energy obtained using these conditions is 1.7 MeV, matching the REP balloon observations on August 20, 1996. This figure represents only one possible combination of parameters, whose purpose is to show that this model can account for the observations of mono-energetic 1.7 MeV precipitating electrons on the duskside.

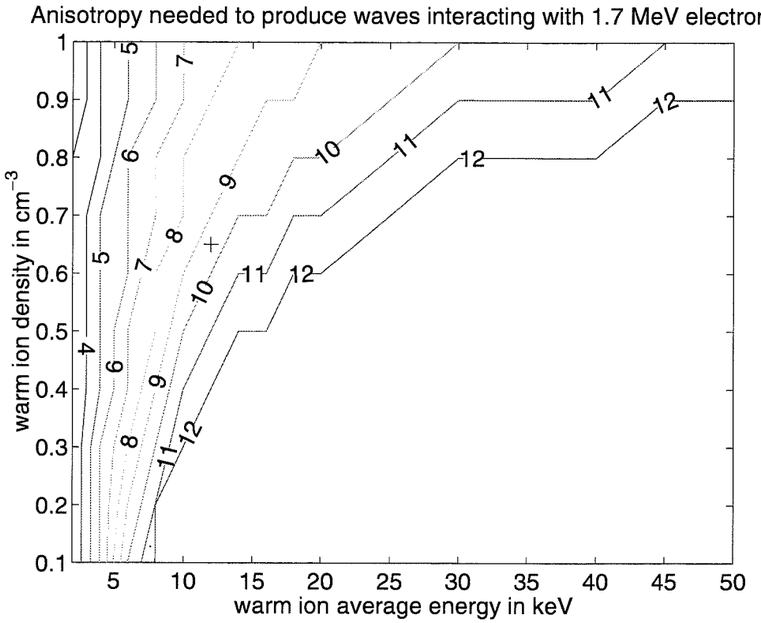

Figure 5.12: Range of parameters interacting with 1.7 MeV electrons. The contours show the anisotropy needed to produce waves that will interact with 1.7 MeV electrons, for various combinations of warm ion density and energy. The magnetic field strength was chosen to correspond to $L = 6$ and the cold ion density was 50 cm^{-3}. The point marked with a cross indicates the parameters used to calculate the growth shown in Figure 5.11.

Figure 5.12 shows a range of warm ion parameters that will produce waves interacting with 1.7 MeV electrons. The warm ion density, energy, and anisotropy, were varied keeping B and N_{ci} constant at 140 nT and 50 cm^{-3}, respectively. The average energy and density are shown on the X and Y axes of the plot, the anisotropy needed to produce waves interacting with 1.7 MeV electrons is shown by the contour lines. The region with no contours shows warm ion energy-density combinations for which no anisotropy below 12 produced the desired waves. Wave growth due to anisotropies greater 12 is not considered.

5.3 *Precipitation of Relativistic Electrons*

We would like to be able to take the wave frequencies and growth rates and translate them directly into a precipitating electron spectrum. Unfortunately, we do not have enough information to adequately address that problem. However, we can use quasi-linear diffusion theory to make a few more estimates about the electron precipitation, which can be compared to observed quantities.

The rate of pitch-angle scattering is given by *Kennel and Petschek* [1966]

$$D_{\alpha\alpha} \approx \frac{\langle \Delta\alpha \rangle^2}{2\Delta t} \approx \left(\frac{B'}{B}\right)^2 \frac{\Omega_e}{\gamma} \frac{k^*}{\Delta k} \tag{5.20}$$

where $D_{\alpha\alpha}$ is the pitch-angle diffusion coefficient, $\langle \Delta\alpha \rangle$ is the average change in pitch angle, Δt is the time that the wave interacts with the particle, B' is the wave magnetic field, B is the ambient magnetic field, k^* is the typical wave number and Δk is the wave number spread. From Figure 5.11 it is estimated that $k^*/\Delta k$ is 1. We have no way of determining B' from our wave growth rates, so we estimate $B' \sim 1$ nT based on observations of *Mauk and McPherron* [1980], who measured 3 nT waves on the duskside and calculated a growth rate of 0.08 Ω_i, for similar model parameters. From Equation 5.20, we obtain a diffusion coefficient of 0.04 s^{-1}.

The diffusion coefficient in the limit of strong pitch-angle diffusion is given by [*Kennel*, 1969]

$$D_{SD} \approx \frac{\alpha_{loss}^2}{2\tau_{1/4}} \approx \frac{\sqrt{E(keV)}}{L^4} \tag{5.21}$$

where α_{loss} is the angular size of the loss cone at the equator, and $\tau_{1/4}$ is the quarter bounce period. This equation gives 0.03 s^{-1} for 1.7 MeV electrons at $L = 6$. Since $D_{\alpha\alpha} \approx D_{SD}$, the interaction is in the strong diffusion region. Thus the precipitating electron flux should be approximately equal to the trapped flux, if estimates for the wave amplitude are correct. If the wave amplitude is over estimated, then the interaction may not be in the strong diffusion region and the precipitating flux should be less than the trapped flux.

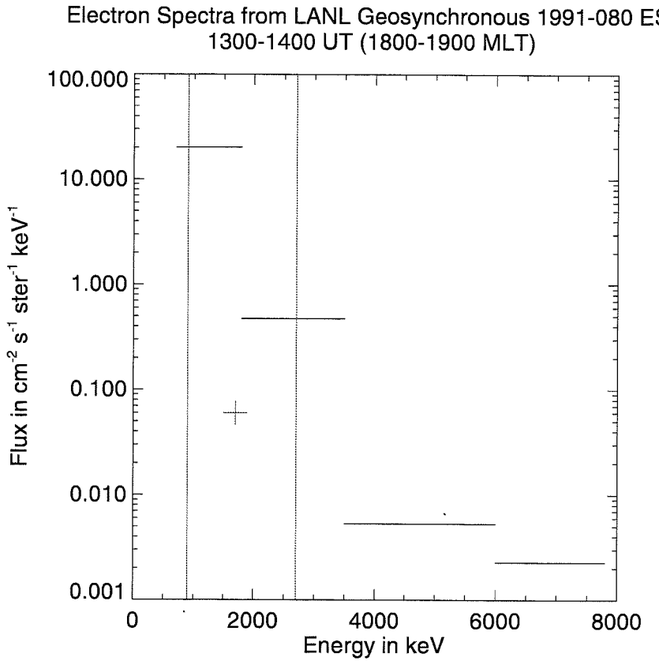

Figure 5.13: The horizontal lines show data from the LANL geosynchronous satellite 1991-080 for energy bins from 0.7 MeV to 7.8 MeV. The vertical lines show the range of electrons that would interact with the predicted EMIC mode waves shown previously in Figure 5.11. The cross marks the flux level inferred from the germanium detector measurements, assuming a 400 keV peak width.

5.3.1 *Predicted Energy Spectra*

Figure 5.13 shows a four-channel energy spectrum from the LANL geosynchronous satellites for electron energies between 700 and 7800 keV. Also indicated on this figure by a cross is the precipitating electron flux inferred from the germanium detector measurements, assuming a peak width of 400 keV. The vertical lines show the range of electron energies that would interact with the predicted EMIC mode waves shown previously in Figure 5.11. The values shown in this figure indicate that the wave-particle interaction is probably not in the strong diffusion region.

5.3.2 *Predicted Spatial Characteristics*

The spatial characteristics predicted by the model match well with the observed spatial characteristics of the REP event. The precipitation was localized to a small region on the duskside, with no small-scale spatial structure. The model predicts that precipitation by this mechanism will occur only in regions where the drift of substorm-injected protons intersects the plasmasphere or a detached plasma region. The area in which this intersection occurs therefore depends on the geometry in the equatorial plane. Lacking information about this geometry, we can only conclude that the region would be small, and spatially uniform. A westward motion in the brightening, as observed in the riometer data, is expected from the westward drift of the substorm-injected protons.

5.3.3 *Predicted Temporal Behavior*

The model does not offer much information about the origin of the two periodicities visible in the precipitation data, 100-200 seconds and 10-20 seconds. The 100-200 second periodicity is possibly the result of an interaction with the coincident field-line resonance. However, more theoretical work is needed before a definite conclusion can be reached.

5.3.4 *Effects of Simplifications on Model Results*

The model presented in this chapter is designed to demonstrate a simple method to investigate the effects of electromagnetic ion cyclotron waves on relativistic electron precipitation. Simplifying approximations include using a dipolar magnetic field, considering only parallel wave propagation, ignoring heavy ions, and neglecting ion losses.

Using a dipolar magnetic field

In the drift model, a dipole magnetic field was assumed. However, the magnetic field is actually stretched on the nightside and compressed on the dayside, resulting in a variable magnetic field strength at geosynchronous altitudes. As particles gradient-curvature drift around the Earth conserving their adiabatic invariants, the distance to their equatorial crossing point changes. Particles injected on the equator at a radius of 6.6 R_E will end up at

larger equatorial distances on the duskside. In addition, this change in radius is dependent on the particle energy, resulting in drift-shell splitting. Particles of different energies injected at the same point on the nightside do not pass through the same point on the duskside in a non-dipolar field. Implications for our model are that the particles observed by the geosynchronous satellite on the nightside may not be the same particles that would drift around to the duskside to drive the wave growth. However, lacking other magnetospheric particle or field measurements, this method provides a reasonable estimate for the duskside particle population.

Considering only parallel propagation

In this dissertation, we examined only waves propagating parallel to the magnetic field. For a more complete treatment of the problem, the growth of whistler and EMIC mode waves propagating at angles to the magnetic field should be examined, along with other waves modes such as the electrostatic ion cyclotron wave mode. However, whistler and EMIC waves are generally only excited at small angles to the magnetic field, and must be refracted in order to propagate at larger angles [*Horne and Thorne*, 1993, 1998]. Electrostatic ion cyclotron mode waves have been shown to be unlikely to resonate with electrons of energies greater than 1 MeV [*Thorne and Andreoli*, 1980]. Therefore, the simple parallel propagating case presented here represents a reasonable first approximation.

Ignoring heavy ions

A magnetospheric plasma typically also contains small amounts of helium and oxygen, in addition to hydrogen. In this model, we assume all ions are H^+. The addition of heavy ions to a plasma will result in stop bands in the wave growth that start at the heavy ion gyrofrequencies and extend to higher frequencies [*Gomberoff and Neira*, 1983; *Kozyra et al.*, 1984]. The width of the stop bands will depend on the energy and density of the heavy ion population. Since the mass of helium is four times that of hydrogen, its gyrofrequency, Ω_{He+}, will be one fourth of the proton (hydrogen) gyrofrequency, Ω_{H+}. Since the mass of oxygen is sixteen times that of hydrogen, its gyrofrequency, Ω_{O+}, will be one sixteenth of

the hydrogen gyrofrequency. However, for the cold plasma density used here (50 cm^{-3}), the wave frequency must be greater than 0.25 Ω_{H+} to resonate with 1.7 MeV electrons, so the heavy ion stop bands will have little effect. If the cold plasma density were greater, then 1.7 MeV electrons could resonate with waves of lower frequencies, so the helium and oxygen stop bands would be more important.

Oxygen ions typically originate from the ionosphere and their presence at the equator at geosynchronous altitudes is strongly dependent on magnetic and solar activity [*Young et al.*, 1982]. Since the REP observations were made at fairly high L-shells when conditions were quiet, it is reasonable to ignore the oxygen stop band. Observations show that helium is typically about 3% of the number density at quiet times [*Gloeckler et al.*, 1985], so it may provide more of a contribution.

In addition, the stop bands resulting from the inclusion of heavy ions also can cause reflection of waves, causing the waves to be trapped near the equator. Ray tracing in a plasma containing heavy ions shows that waves guided along the plasmapause density gradient experience a large convective amplification due to multiple reflections [*Horne and Thorne*, 1993]. This reflection of waves may be the reason why no EMIC waves were observed at the balloon during the REP event.

Neglecting ion losses

In our model, we calculated the wave growth assuming that the substorm protons drifted unchanged around the Earth. In reality, some of these protons would be precipitated before reaching the duskside, reducing the density of the warm ions and increasing their anisotropy. In addition, the growth of electromagnetic ion cyclotron waves would change the proton distribution, possibly limiting the wave growth. However, if the wave growth occurs only in a very localized spatial region on the duskside, then these effects would be less important than if wave growth and proton loss occur over a large region of space.

Chapter 6

CONCLUSION

6.1 Results

6.1.1 Observations

In this dissertation, we have presented new observations of a duskside relativistic electron precipitation event. These observations were made using a set of complementary balloon-borne X-ray detectors. An X-ray imager measured the spatial characteristics of the electron precipitation while a liquid nitrogen cooled germanium spectrometer determined the energy spectrum of the electron precipitation. This combination of instruments had not been flown together previously, and the results presented in this dissertation demonstrate the promise of this set of instruments.

The X-ray energy spectrum of the observed event was unusual in the 1.7 MeV mono-energetic electron precipitation implied. No previous X-ray observations had been able to determine this type of electron precipitation before. This event may have been of a different type than REP events previously observed, or previous experiments may have lacked the energy range and resolution to distinguish mono-energetic 1.7 MeV electron precipitation from a hard exponentially falling electron spectrum.

The X-ray imager was able to show that the event had very little small-scale spatial structure or motion, but was larger than the field of view of the instrument, 50 km in diameter at 60 km altitude. Ground-based riometer images were consistent with the X-ray images and established the size of the precipitation region to be 80 km by 160 km at 60 km altitude. The region of ionospheric absorption was spatially localized, with only a slight south-westward motion.

Data from other ground and satellite-based experiments established that the REP event

occurred at about the same time as a field line resonance and a small substorm. However, the event was not auroral in nature, since the auroral oval was north of the balloon location. There was also no increase in relativistic electrons observed in the equatorial region, leading to the conclusion that the REP event was the result of selective precipitation of ambient relativistic electrons from the radiation belts.

6.1.2 Theory

We examined several different mechanisms for selective precipitation of relativistic electrons, including field aligned potential drops, plasma-sheet scattering and wave-particle interactions. For the mono-energetic energy spectrum inferred from X-ray observations during this duskside REP event, wave-particle interactions with electromagnetic ion cyclotron waves were determined to be most likely. In order for electromagnetic ion cyclotron waves to grow, they must have a source of free energy, and the substorm onset was timed such that injected protons would arrive on the duskside at the same time the REP event began.

A model was constructed to evaluate what parameters would produce EMIC mode waves that would interact with 1.7 MeV electrons at the correct local time. The model calculated gradient-curvature drifts for a bi-Maxwellian proton distribution in a dipole magnetic field. The density, temperature, and temporal behavior of the proton population were taken from geosynchronous satellite observations.

From these input conditions, we determined the resulting proton distribution on the duskside, and evaluated numerically the EMIC wave growth produced. Wave growth was calculated by numerically solving the dispersion relation for parallel-propagation in a three-component plasma consisting of ambient cold electrons and protons, and warm protons from the substorm injection. The wave growth calculation involved five free parameters: 1) magnetic field strength, 2) cold plasma density, 3) warm ion density, 4) warm ion average energy, and 5) warm ion temperature anisotropy. The magnetic field strength was determined using the dipole approximation, which is reasonable on the duskside. The cold plasma density was determined using measurements from a geosynchronous satellite which passed through the same local time region several hours after the event. The three

warm ion parameters were determined using the drift simulation with input from the LANL geosynchronous satellite located in the injection region.

These input parameters resulted in waves that interacted with 5 MeV electrons, about three times more energetic than the electrons inferred from the X-ray measurements. So we examined how the resonant electron energy would change if each of the five free parameters were varied individually. Variation with the magnetic field strength was small for reasonable variations in the magnetic field. Surprisingly, variation with the cold plasma density was also minimal for densities above 10 cm^{-3}. Variations with the three warm ion parameters were more significant, and we found that either increasing the warm ion density, decreasing the warm ion average energy, increasing the warm ion temperature anisotropy, or some combination of the preceding changes could reduce the electron resonant energy to the 1.7 MeV level.

Thus satisfied with how the model reproduces the energy spectra of the REP event, we next look at the spatial structure of the event. The duskside local time occurrence of the event is explained by the need for high densities in the model. The equatorial interaction region must either be inside the plasmasphere or inside a detached plasma region for both the wave growth and the electron resonance to occur. The spatial localization and lack of small-scale structure are also consistent with a model of protons drifting through a localized region of high-density plasma on the equator. The slight westward motion visible in the riometer images is further evidence for this model.

The complex temporal structure of the event is less well addressed by the model. Although there was some correlation between the 100-200 second period and temporal structure in the substorm injection observed on the nightside, the model indicates that this structure would be smoothed out by the time the protons drifted around to the duskside. The drift period for an equatorially mirroring 1.7 MeV electron is about 420 seconds, so it is unlikely that the periodicity in the bursts is drift related. Indirect interaction with the field line resonance is a possible source for the 100-200 seconds REP periodicity, but the lack of a strong one-to-one correspondence between the magnetometer and precipitation data makes it difficult to definitively establish a relationship for this case.

We were not able to come up with a mechanism to explain the origin of the 10-20

second modulations superposed on the larger X-ray bursts, or why these modulations are more noticeable during the second half of the event. However, it is worth noting that this frequency is comparable to that observed in pulsating aurora, so further theoretical work on that phenomenon may also shed light on this REP event.

6.2 Future Work

6.2.1 Observations

In most space physics processes, the events take place over a large region of space, and it is difficult to figure out what is happening based on individual single-point measurements. To really understand the causes of duskside REP events, we need either more single-point observations of similar events, or additional single-event case studies correlated with satellites in multiple regions of space.

It would seem that mono-energetic relativistic electron precipitation by interaction with EMIC mode waves is most likely to be observed on the duskside during geomagnetically quiet times. Balloon campaigns could be planned around these times in order to increase the possibility to observing further REP events. The event we observed was larger than the field of view of the X-ray instruments, so future REP campaigns would ideally utilize instruments with larger fields of view. Balloon-borne X-ray instruments are ideal for studying REP events, since X-ray measurements can determine the precipitating electron energy spectra, and they can observe the sky for moderately long periods of time.

Since it is somewhat difficult to increase the field of view of the X-ray instruments without significantly reducing the quality of data, imaging riometers could be used to supplement the balloon observations. In addition, imaging riometers can operate continuously, so they can be used to look for duskside behavior similar to that observed here, although they cannot distinguish the energies of the precipitating electrons.

Low-altitude satellites can also be of some use in distinguishing precipitating electron spectra, although they are limited since they would move very quickly through regions of the size observed in this event. Spectra can be examined for mono-energetic peaks in electron precipitation, and association with electromagnetic ion cyclotron waves. Since ion

cyclotron waves do not usually propagate to the ground, they are difficult to observe. However, they would be expected to produce proton precipitation, so experimenters could look for that, too. Additionally, statistical studies relating REP events with field line resonances and substorms would be useful.

6.2.2 Theory

The theoretical work presented in this dissertation consisted of a relatively simple model, designed to illustrate the feasibility of EMIC mode waves producing mono-energetic relativistic electron precipitation. As discussed in the previous chapter, this simple model neglected the effects of a non-dipolar magnetic field, heavy ions, non-parallel wave propagation and ion losses. Further theoretical effort could focus on incorporating these factors into the model and reevaluating the August 20, 1996 REP event.

However, the observations of this REP event were somewhat limited. Thus, there is no way of adequately testing a more complex model with additional free parameters. Therefore, our recommendation is that future work on duskside relativistic electron precipitation concentrate on obtaining further observations before continuing with theoretical efforts.

BIBLIOGRAPHY

Anderson, B. J., R. E. Erlandson, and L. J. Zanetti, A statistical study of Pc1-2 magnetic pulsations in the equatorial magnetosphere 1. Equatorial occurrence distributions, *J. Geophys. Res.*, *97*, 3075, 1992.

Anger, H. O., Scintillation camera, *Rev. Sci. Instr.*, *29*, 27, 1958.

Bailey, D. K., and M. A. Pomerantz, Relativistic electron precipitation into the mesosphere at subauroral latitudes, *J. Geophys. Res.*, *70*, 5823, 1965.

Baker, D. N., J. B. Blake, R. W. Klebesadel, and P. R. Higbie, Highly relativistic electrons in the Earth's outer magnetosphere 1. Lifetimes and temporal history 1979-84, *J. Geophys. Res.*, *91*, 4265, 1986.

Bame, S., et al., Magnetospheric plasma analyzer for spacecraft with constrained resources, *Rev. Sci. Instr.*, *64*, 1026, 1993.

Barcus, J. R., and T. J. Rosenberg, Energy spectrum for auroral-zone X-rays 1. Diurnal and type effects, *J. Geophys. Res.*, *71*, 803, 1966.

Belian, R. D., G. R. Gisler, T. Cayton, and R. Christensen, High-Z energetic particles at geosynchronous orbit during the great solar proton event of October 1989, *J. Geophys. Res.*, *97*, 16897, 1992.

Berger, M. J., and S. M. Seltzer, Bermsstrahlung in the atmosphere, *J. Atmos. Terr. Phys.*, *34*, 85, 1972.

Blake, J. B., M. D. Looper, D. N. Baker, R. Nakamura, B. Klecker, and D. Hovestadt, New high temporal and spatial resolution measurements by SAMPEX of the precipitation of relativistic electrons, *Adv. Space Res.*, *18*, 191, 1996.

Browne, S., J. K. Hargreaves, and B. Honary, An imaging riometer for ionospheric studies, *Electronics Comm. Eng. J.*, *7*, 209, 1995.

Callis, L. B., D. N. Baker, J. B. Blake, J. D. Lambeth, R. E. Boughner, M. Natarajan, R. W. Klebesadel, and D. J. Gorney, Precipitating relativistic electrons: their long-term effect on stratospheric odd nitrogen levels, *J. Geophys. Res.*, *96*, 2939, 1991.

Carpenter, D. L., Whistler evidence of the dynamic behavior of the duskside bulge in the plasmasphere, *J. Geophys. Res.*, *75*, 3837, 1970.

Chang, H. C., and U. S. Inan, Quasi-relativistic electron precipitation due to interactions with coherent VLF waves in the magnetosphere, *J. Geophys. Res.*, *88*, 318, 1983.

Chappell, C. R., K. K. Harris, and G. W. Sharp, A study of the influence of magnetic activity on the location of the plasmapause as measured by OGO 5, *J. Geophys. Res.*, *75*, 50, 1970.

Cornwall, J. M., and M. Schulz, Electromagnetic ion-cyclotron instabilities in multicomponent magnetospheric plasmas, *J. Geophys. Res.*, *76*, 7791, 1971.

Cornwall, J. M., F. V. Coroniti, and R. M. Thorne, Turbulent loss of ring current protons, *J. Geophys. Res.*, *75*, 4699, 1970.

Coroniti, F. V., and C. F. Kennel, Electron precipitation pulsations, *J. Geophys. Res.*, *75*, 1205, 1970.

Davidson, G. T., Relativistic electron precipitation and resonance with ion cyclotron waves, *J. Atmos. Terr. Phys.*, *40*, 1085, 1978.

Evans, D. S., Precipitating electron fluxes formed by a magnetic field aligned potential difference, *J. Geophys. Res.*, *79*, 2853, 1974.

Evans, R. D., *The Atomic Nucleus*, McGraw-Hill Book Company, New York, 1955.

Foat, J. E., et al., First detection of a terrestrial MeV X-ray burst, *Geophys. Res. Lett.*, *25*, 4109, 1998.

Fujimoto, M., and A. Nishida, Energization and anisotropization of energetic electrons in the Earth's radiation belt by the recirculation process, *J. Geophys. Res.*, *95*, 4265, 1990.

Gloeckler, G., B. Wilken, W. Stüdeman, F. M. Ipavich, D. Hovestadt, D. C. Hamilton, and G. Kremser, First measurements of the bulk of the storm-time ring current (1 to 300 keV/e) with AMPTE-CCE, *Geophys. Res. Lett.*, *12*, 325, 1985.

Gomberoff, L., and R. Neira, Convective growth rate of ion cyclotron waves in a H^+-He^+ and H^+-He^+-O^+ plasma, *J. Geophys. Res.*, *88*, 2170, 1983.

Herrero, F. A., D. N. Baker, and R. A. Goldberg, Rocket measurements of relativistic electrons: new features in fluxes, spectra and pitch angle distributions, *Geophys. Res. Lett.*, *18*, 1481, 1991.

Horne, R. B., and R. M. Thorne, On the preferred source location for the convective amplification of ion cyclotron waves, *J. Geophys. Res.*, *98*, 9233, 1993.

Horne, R. B., and R. M. Thorne, Potential waves for relativistic electron scattering and stochastic acceleration during magnetic storms, *Geophys. Res. Lett.*, *25*, 3011, 1998.

Hudson, M. K., S. R. Elkington, J. G. Lyon, and C. G. Goodrich, Increase in relativistic electron flux in the inner magnetosphere: ULF wave mode structure, *submitted to Adv. Space Res.*, 1999a.

Hudson, M. K., S. R. Elkington, J. G. Lyon, C. G. Goodrich, and T. J. Rosenberg, Simulation of radiation belt dynamics driven by solar wind variations, in *Physics of Sun-Earth Plasma, in press*, edited by J. L. Burch, AGU, Washington, D. C., 1999b.

Imhof, W. L., et al., The polar ionospheric X-ray imaging experiment (PIXIE), *Space Sci. Rev.*, *71*, 385, 1995.

Imhof, W. L., H. D. Voss, J. Mobilia, D. W. Datlowe, and E. E. Gaines, The precipitation of relativistic electrons near the trapping boundary, *J. Geophys. Res.*, *96*, 5619, 1991.

Imhof, W. L., D. L. Chennete, E. E. Gaines, and J. D. Winningham, Characteristics of electrons at the trapping boundary of the radiation belts, *J. Geophys. Res.*, *102*, 95, 1997.

Johns, C. M., and R. P. Lin, The derivation of parent electron spectra from bremsstrahlung hard X-ray spectra, *Solar Phys.*, *137*, 121, 1992.

Jordanova, V. K., J. U. Kozyra, A. F. Nagy, and G. V. Khazanov, Kinetic model of the ring current-atmosphere interactions, *J. Geophys. Res.*, *102*, 14279, 1997.

Kennel, C. F., Consequences of a magnetospheric plasma, *Rev. Geophys.*, *7*, 379, 1969.

Kennel, C. F., and H. E. Petschek, Limit on stably trapped particle fluxes, *J. Geophys. Res.*, *71*, 1, 1966.

Kivelson, M. G., and C. T. Russell, *Introduction to Space Physics*, Cambridge University Press, Cambridge, UK, 1995.

Knoll, G. F., *Radiation Detection and Measurement*, John Wiley & Sons, New York, 1989.

Kozyra, J. U., T. E. Cravens, A. F. Nagy, E. G. Fontheim, and R. S. B. Ong, Effects of energetic heavy ions on electromagnetic ion cyclotron wave generation in the plasmapause region, *J. Geophys. Res.*, *89*, 2217, 1984.

LaBelle, J., R. A. Treumann, W. Baumjohann, G. Haerendel, N. Sckopke, G. Paschmann, and H. Lühr, The duskside plasmapause/ring current interface: Convection and plasma wave observations, *J. Geophys. Res.*, *93*, 2573, 1988.

Lepping, R., et al., The WIND magnetic field investigation, *Space Sci. Rev.*, *71*, 207, 1995.

Li, X., et al., Multisatellite observations of the outer zone electron variation during the November 3-4, 1993, magnetic storm, *J. Geophys. Res.*, *102*, 14123, 1997.

Lin, C. S., and G. K. Parks, Further discussion of the cyclotron instability, *J. Geophys. Res.*, *79*, 2894, 1974.

Lin, C. S., and G. K. Parks, Ion cyclotron instability of drifting plasma clouds, *J. Geophys. Res.*, *81*, 3919, 1976.

Lin, R., et al., A three-dimensional plasma and energetic particle investigation for the WIND spacecraft, *Space Sci. Rev.*, *71*, 125, 1995.

Liu, W. W., and G. Rostoker, Energetic ring current particles generated by recurring substorm cycles, *J. Geophys. Res.*, *100*, 21897, 1995.

Lühr, H., A. Aylward, S. C. Bucher, A. Pajunää, K. Pajunpää, T. Holmboe, and S. M. Zalewski, Westward moving dynamic substorm features observed with the IMAGE magnetometer network and other ground-based instruments, *Ann. Geophys.*, *16*, 425, 1998.

Lui, A. T. Y., Extended consideration of a synthesis model for magnetospheric substorms, in *Magnetospheric Substorms, Geophys. Monogr. 64*, edited by J. R. Kan, T. A. Potemra, S. Kokubun, and T. Ijima, p. 43, AGU, Washington, D. C., 1991.

Lyons, L. R., and R. M. Thorne, Parasitic pitch angle diffusion of radiation belt particles by ion cyclotron waves, *J. Geophys. Res.*, *77*, 5608, 1972.

Lyons, L. R., and D. J. Williams, *Quantitative Aspects of Magnetospheric Physics*, D. Reidel Publishing Company, Dordrecht, Holland, 1984.

Matthews, D. L., and D. J. Simons, Observation of relativistic electron precipitation at L=6, *J. Geophys. Res.*, *78*, 7539, 1973.

Mauk, B. H., and R. L. McPherron, An experimental test of the electromagnetic ion cyclotron instability within the Earth's magnetosphere, *Phys. Fluids*, *23*, 2111, 1980.

Mauk, B. H., J. Chin, and G. K. Parks, Auroral X-ray images, *J. Geophys. Res.*, *86*, 6827, 1981.

Meier, M., R. Belian, T. Cayton, R. Christensen, B. Garcia, K. Grace, J. Ingraham, J. Laros, and G. Reeves, The energy spectrometer for particles (ESP): Instrument description and orbital performance, in *Workshop on the Earth's Trapped Particle Environment*, edited by G. Reeves, p. 203, AIP Press, Woodbury, NY, 1996.

Melrose, D. B., *Instabilities in Space and Laboratory Plasmas*, Cambridge University Press, Cambridge, UK, 1986.

Moldwin, M. B., M. F. Thomsen, S. J. Bame, D. J. McComas, L. A. Weiss, G. D. Reeves, and R. D. Belian, The appearance of plasmaspheric plasma in the outer magnetosphere in association with the substorm growth phase, *Geophys. Res. Lett.*, *23*, 801, 1996.

Mozer, F. S., C. W. Carlson, M. K. Hudson, R. B. Torbert, B. Parady, J. Yatteau, and M. C. Kelley, Observations of paired electrostatic shocks in the polar magnetosphere, *Phys. Rev. Lett.*, *38*, 292, 1977.

Nagai, T., "Space weather forecast": Prediction of relativistic electron intensity at synchronous orbit, *Geophys. Res. Lett.*, *15*, 425, 1988.

Nakamura, R., D. N. Baker, J. B. Blake, S. Kanekal, B. Klecher, and D. Hovestadt, Relativistic electron precipitation enhancements near the outer edge of the radiation belt, *Geophys. Res. Lett.*, *22*, 1129, 1995.

Parks, G. K., *Physics of Space Plasmas*, Addison-Wesley Publishing Co., Redwood City, CA, 1991.

Parks, G. K., C. Gurgiolo, and R. West, Relativistic electron precipitation, *Geophys. Res. Lett.*, *6*, 393, 1979.

Parks, G. K., B. Mauk, C. Gurgiolo, and C. S. Lin, Observations of plasma injection, in *Dynamics of the Magnetosphere*, edited by S.-I. Akasofu, p. 371, D. Reidel Publishing Company, Dordrecht, Holland, 1980.

Parks, G. K., S. H. Werden, and M. P. McCarthy, Pinhole X-ray cameras for imaging small-scaled auroral structures, *Optical Engineering*, *32*, 3164, 1993.

Paulikas, G. A., and J. B. Blake, Effects of the solar wind on magnetospheric dynamics: energetic electrons at the synchronous orbit, in *Quantitative Modeling of Magnetospheric Processes*, edited by W. P. Olson, p. 180, AGU, Washington, D. C., 1979.

Perraut, S., and A. Roux, Respectrive role of the cold and warm plasma densities on the generation mechanism of ULF waves in the magnetosphere, *J. Atmos. Terr. Phys.*, *37*, 407, 1975.

Press, W., S. Teukolsky, W. Vetterling, and B. Flannery, *Numerical Recipes in C, Second Edition*, Cambridge University Press, Cambridge, UK, 1992.

Ranta, H., A. Ranta, J. K. Hargreaves, and S. Browne, Localized absorption events in the afternoon sector, *J. Atmos. Solar-Terr. Phys.*, *59*, 891, 1997.

Reeves, G. D., Relativistic electrons and magnetic storms: 1992-1995, *Geophys. Res. Lett.*, *25*, 1817, 1998.

Rice, J. A., *Mathematical Statistics and Data Analysis, Second Edition*, Duxbury Press, Belmont, California, 1995.

Roederer, J. G., *Dynamics of Geomagnetically Trapped Radiation*, Springer-Verlag, New York, 1970.

Rosenberg, T. J., L. J. Lanzerotti, D. K. Bailey, and J. D. Pierson, Energy spectra in relativistic electron precipitation events, *J. Atmos. Terr. Phys.*, *34*, 1977, 1972.

Rostoker, G., S. Skone, and D. N. Baker, On the origin of relativistic electrons in the magnetosphere associated with some geomagnetic storms, *Geophys. Res. Lett.*, *25*, 3701, 1998.

Samson, J. C., T. Hughes, F. Creutzberg, D. D. Wallis, R. A. Greenwald, and J. M. Ruohoniemi, Obervations of a detached, discrete arc in association with field line resonances, *J. Geophys. Res.*, *96*, 15683, 1991.

Schulz, M., and L. J. Lanzerotti, *Particle Diffusion in the Radiation Belts*, Springer-Verlag, New York, 1974.

Sergeev, V. A., and N. A. Tsyganenko, Energetic particle losses and trapping boundaries as deduced from calcuations with a realistic magnetic field model, *Plan. Space Sci.*, *30*, 999, 1982.

Sergeev, V. A., E. M. Sazhina, N. A. Tsyganenko, J. Å. Lundblad, and F. Søraas, Pitch-angle scattering of energetic protons in the magnetotail current sheet as the dominant

source of their isotropic precipitation into the nightside ionosphere, *Plan. Space Sci.*, *31*, 1147, 1983.

Skoug, R. M., The origin of narrow band cyclotron wave emission called chorus, Ph.D. thesis, University of Washington, 1995.

Smith, D. M., R. P. Lin, K. A. Anderson, K. Hurley, and C. M. Johns, High-resolution spectra of 20-300 keV hard X-rays from electron precipitation over Antarctica, *J. Geophys. Res.*, *100*, 19675, 1995.

Solomon, J., Drift of particles and wave-particle interactions, in *The Magnetospheres of the Earth and Jupiter*, edited by V. Formisano, p. 153, D. Reidel Publishing Company, Dordrecht, Holland, 1975.

Speiser, T., Particle trajectories in model current sheets, 1. Analytic solution, *J. Geophys. Res.*, *70*, 4219, 1965.

Stix, T. H., *Waves in Plasmas*, American Institute of Physics, New York, 1992.

Summers, D., R. M. Thorne, and F. Xiao, Relativistic theory of wave-particle resonant diffusion with application to electron acceleration in the magnetosphere, *J. Geophys. Res.*, *103*, 20487, 1998.

Swift, D. W., Mechanisms for auroral precipitation: A review, *Rev. Geophys. Space Phys.*, *19*, 185, 1981.

Thorne, R. M., A possible cause of dayside relativistic electron precipitation events, *J. Atmos. Terr. Phys.*, *36*, 635, 1974.

Thorne, R. M., and L. J. Andreoli, Mechanisms for intense relativistic electron precipitation, in *Exploration of the Polar Upper Atmosphere*, edited by C. Deehr, and J. A. Holtet, p. 381, D. Reidel Publishing Company, Dordrecht, Holland, 1980.

Thorne, R. M., and C. F. Kennel, Relativistic electron precipitation during magnetic storm main phase, *J. Geophys. Res.*, *76*, 4446, 1971.

Thorne, R. M., and T. R. Larsen, An investigation of relativistic electron precipitation events and their association with magnetospheric substorm activity, *J. Geophys. Res.*, *81*, 5501, 1976.

Torr, M. R., et al., A far ultraviolet imager for the international solar-terrestrial physics mission, *Space Sci. Rev.*, *71*, 329, 1995.

Treilhou, J. P., K. Lorentzen, M. McCarthy, G. K. Parks, J. Foat, B. Lin, and C. Jacquey, Hard X-rays and electric field in the subauroral afternoon sector, *32nd COSPAR Scientific Assembly*, pp. PSB1–0019, 1998.

Tsyganenko, N. A., A magnetospheric magnetic field model with a warped tail current sheet, *Plan. Space Sci.*, *37*, 5, 1989.

Tsyganenko, N. A., and A. V. Usmanov, Determination of the magnetospheric current system parameters and development of experimental geomagnetic field models based on data from IMP and HEOS satellites, *Plan. Space Sci.*, *30*, 985, 1982.

Walker, A. D. M., *Plasma Waves in the Magnetosphere*, Springer-Verlag, New York, 1993.

Werden, S., Energetic electron precipitation in the aurora as determined by X-ray imaging, Ph.D. thesis, University of Washington, 1988.

West, R. H., and G. K. Parks, ELF emissions and relativistic electron precipitation, *J. Geophys. Res.*, *89*, 159, 1984.

Xu, B. L., J. C. Samson, W. W. Liu, F. Creutzberg, and T. J. Hughes, Observations of optical aurora modulated by resonant Alfvén waves, *J. Geophys. Res.*, *98*, 11531, 1993.

Young, D. T., H. Balsiger, and J. Geiss, Correlations of magnetospheric ion composition with geomagnetic and solar activity, *J. Geophys. Res.*, *87*, 9077, 1982.

VITA

Kirsten Ruth Lorentzen was born on Sept. 18, 1969, in Mountain View, California to Grace and Einar Lorentzen. She graduated from Adrian Wilcox High School in Santa Clara, California in 1987, and received an A. B. in physics from Dartmouth College in 1991. After college, she joined the U. S. Peace Corps, and served for two years in Belize, Central America as a high school physics teacher at Toledo Community College. From 1993 to 1999 she was a graduate student in the Geophysics Program at the University of Washington.